Spin dependent transport of hot electrons through ultrathin epitaxial metallic films

by

Emanuel Heindl

(2010)

Thesis submitted in partial fulfillment
of the requirements for the degree of
Doctor of Natural Sciences (Dr. rer. nat.)
in the department of Physics
of the university of Regensburg

To my son
Sascha Heindl

Promotionsgesuch eingereicht am 23.06.2010
Die Arbeit wurde angeleitet von Prof. Dr. Christian H. Back

Prüfungsausschuss:	Vorsitzender:	Prof. Dr. John Schliemann
	1. Gutachter:	Prof. Dr. Christian H. Back
	2. Gutachter:	Prof. Dr. Jascha Repp
	weiterer Prüfer:	Prof. Dr. Dieter Weiss

Contents

List of Figures

1 Introduction

When a material is exposed to an incident beam of particles, the particles may interact with the material in such a way that the particle characteristics measured thereafter reflect some material properties. A thorough interpretation of the acquired results demands the determination of the states of the initially incident and outgoing particles. Many experiments in natural sciences and even everyday occurrences are based on this principle. By way of example, we determine the color of a leaf by illuminating it and identifying the frequencies of the reflected light by means of our eyes. However, the leaf appears green when white light is utilized and black when monochromatic red light shines on it as a consequence of absorption. In some situations interaction is weak and some of the particles do not feel the presence of the material at all. These become transmitted through the material in a ballistic manner. However, information about the material can still be gained, yet in a complementary way to the method above. For instance, in a Lambert-Beer absorption experiment we record the initial incident radiation intensity accompanied by the attenuated transmitted intensity and deduce the thickness of a thin material.

In general all such experiments use an amount of probing particles interacting with the material for a finite time. Thus, steady-state properties are probed when the material itself is negligibly changed during the time of interaction. Otherwise, the material is driven out of equilibrium into excited states, which may then be probed solely or simultaneously with the equilibrium ones. Scientists are fitted therefore with the possibility to investigate nonequilibrium states and processes being the basis for all dynamic and relaxation phenomena.

Considerable attention turned to the case when electrons of a ferromagnetic metal become excited. A ferromagnet looses a part of its magnetization on a very fast (less than 1 ps) timescale upon incidence of an ultrashort laser pulse [1]. The underlying processes randomizing the spin order are yet not completely understood, though appear to be crucial for developing applications based on fast magnetization switching [2]. On the other hand, transport of excited electrons through a ferromagnetic metal can be employed as a spin polarized current source. Based on spin dependent mean free paths this mechanism may be utilized for spin injection into semiconductors, a nontrivial challenge in spin-electronics [3]. Hence, spin dependent relaxation and transport of

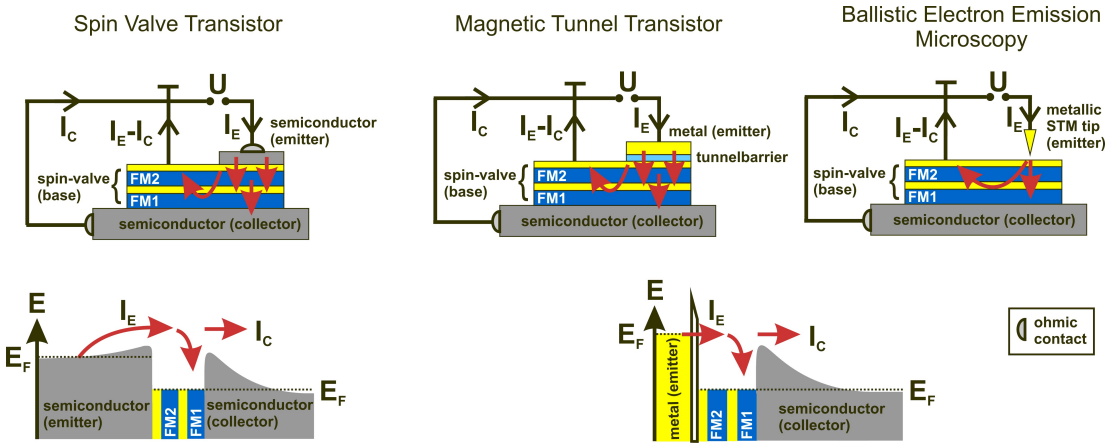

Figure 1.1: Experimental setups of a Spin Valve Transistor, Magnetic Tunnel Transistor and Ballistic Electron Emission Microscopy combined with their spatial conduction band evolutions.

excited (hot) electrons is of fundamental importance to the research of magnetism and spin electronics and has already stimulated research for several years clearing up many questions but also leaving some unacknowledged. To name only a few of the employed techniques, we cite time resolved experiments [1, 2, 4], planar devices [3, 5–10], electron spectroscopy [11–14] and theoretical approaches [15–21].

In the mid of the 1990's two new species of hot electron transistors (HET's), namely the Spin Valve Transistor (SVT) and the Magnetic Tunnel Transistor (MTT) [5, 7], were introduced to investigate spin dependent transport of low energy electrons in the ballistic (collisionless) regime. They resemble the three terminal design of metal base HET's in a common base circuit previously proposed in the 1960's to speed up conventional transistors[1] [5, 24], see Fig.1.1. A related experimental technique is Ballistic Electron Emission Microscopy (BEEM), which uses the tip of a scanning tunneling microscope (STM) as an energetically tunable hot electron emitter into a metal(base)/n-type semiconductor(collector) structure, see also Fig.1.1. The advantages are nanometer resolution and its ideal vacuum tunneling barrier preventing leakage currents and consequently allowing room temperature experiments. In consideration of these three setups, one may doubtlessly remember of Giant Magnetic Resistance (GMR) experiments due to the similar layer stack structure. They have certainly some aspects in common but major distinctions exist due to electron relaxation and excitation processes in HET's.

Ballistic electron transport is investigated by injecting hot electrons into the base layers, while excitation processes are studied by ejecting hot electrons from the base into

[1]The reader is also referred to similar all semiconductor designs of HET's like tunneling hot electron emission amplifiers (THETA) proposed in 1981 [22, 23].

the STM-tip by reversing the tunneling voltage. The latter approach is referred to as reverse or scattering ballistic electron emission microscopy (RBEEM or SBEEM) since hot electrons are not created by tunneling but by collision processes of hot holes with cold (thermalized) electrons. Furthermore, by replacing the n-type with a p-type semiconductor collector ballistic transport of excited holes across the base layers in the conduction bands below E_F can be studied, which is referred to as ballistic hole emission microscopy (BHEM) [25]. To complete the nomenclature, BEEM is also referred to as ballistic electron magnetic microscopy (BEMM) when spin dependent properties are studied, which is the approach this thesis is concerned with.

Let us now focus on the base layers, where the case arises that spin degenerate hot electrons of energy E and momentum $\mathbf{k}$ enter a thin ferromagnetic metal film. When we measure their energy and momentum distributions after some time delay within the ferromagnetic material, we will find one spin component left at energies around E and momentum $\mathbf{k}$, while the other spin component becomes more relaxed in energy and momentum space as a result of spin dependent relaxation. By placing a conduction band step at the edge of the thin film, thermalized and more relaxed electrons are prevented from overcoming the barrier, while electrons with energies larger than the barrier step are able to pass building up the collector current I_C, see again Fig.1.1. Due to the distinct momentum and energy distributions of both spin species, a spin filter effect is created. One spin component is more hindered to cross the band step than the other. In BEEM experiments the band step is mostly provided by a metal/n-type semiconductor contact giving rise to a Schottky barrier. Note that this barrier acts not only as an energy but also as a momentum (angular) filter for hot electrons. Since hot electrons loose a majority of their energy and momentum during transport over distances of some electron mean free paths, the overall base thickness should not exceed this value by far, which leads to an inherently ballistic rather than a diffusive transport experiment.

The introduction of a spin valve stack, i.e. a trilayer consisting of two ferromagnetic layers separated by a nonmagnetic layer, gives rise to a collector current being dependent on the magnetization configuration of the spin valve, such that hot electron transport through the metallic base can be studied spin dependently. The resulting spin contrast is commonly expressed in terms of a magnetocurrent (MC) rather than a magnetoresistance as the ohmic law is not well defined in the ballistic regime. Conductivity is not governed by the scattering time τ only, but also by density of states effects. According to the spin valve technique the quantity magnetocurrent is defined as

$$\mathrm{MC} \quad = \quad (I_C^P - I_C^{AP})/I_C^{AP} \tag{1.1}$$

with $I_C^{P(AP)}$ denoting the collector current in parallel(antiparallel) magnetization configuration. Magnetocurrents as large as 3400 % at 77 K using a MTT-design [26] and 600 % at room temperature using BEEM [27] have already been reported reflecting a

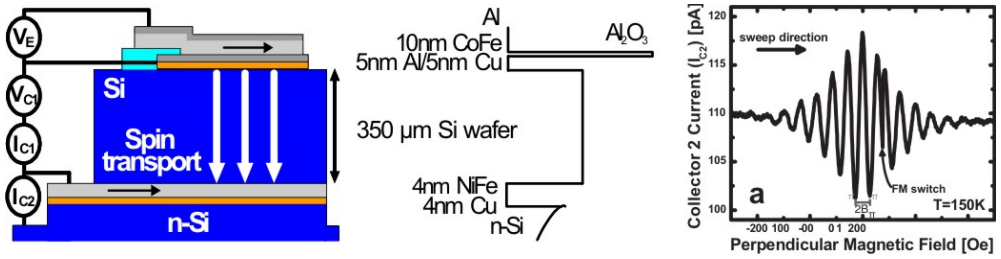

Figure 1.2: Schematic side view of a spin injection device (left panel) and associated conduction band diagram (middle panel). Spin polarized electrons are injected from the top of the device by tunneling and drift in an electric field to the bottom, where they are detected with a semiconductor/ferromagnetic metal/semiconductor structure employing spin dependent hot electron filtering. Spin precession experiments using the Hanle effect evidence the successful spin injection into the semiconductor (right panel). Images extracted from [10].

degree of spin polarization approaching 100 % according to Julliere's formula

$$\mathrm{MC} = \frac{2P_1P_2}{1-P_1P_2} \tag{1.2}$$

$$P_i = \frac{T_i^M - T_i^m}{T_i^M + T_i^m} \tag{1.3}$$

with T_i being the hot electron transmission of a ferromagnetic film i. The indices M and m represent majority and minority spins, respectively. Due to the large hot electron spin polarization P hot electron spin filtering is employed for spin detection and injection into semiconductors [3], as well. In another experiment, spin transport up to several hundred micrometers through semiconducting silicon has been obtained by utilizing the sensitive spin detection capability [10], compare Fig.1.2.

Optimizing spin injection and detection efficiency demands large magnetocurrents accompanied by preferably large collector currents. However, defects and a multitude of interfaces appearing as grain boundaries exist within the thin metallic base films, which may strongly suppress ballistic currents [16, 28] and may even affect the spin filter efficiency [16, 29–31].

The subject of this thesis is to investigate spin dependent hot electron transport through single crystalline spin valve stacks involving bcc Fe- and $Fe_{34}Co_{66}$-films deposited by Molecular Beam Epitaxy (MBE) onto conventional n-type semiconductor wafers. The well known magnetization behavior of these materials combined with their very distinct electronic properties eases the interpretation of the results in terms of hot electron transport. Due to the epitaxial structure the interaction of electrons with defects and interfaces is reduced to a minimum and an increase in the available spin polarization and hot electron transmission can be expected. Moreover band structure arguments can

be included into the analysis of the measured data granting new insights. The specific aims are to analyze in which way different relaxation processes enter electron transport by varying the electron energy, the temperature and the thickness of the base layers. All revealed results are crosschecked with related studies and compared to theoretical models. For the experimental transport measurements an already existing BEEM setup working at ambient conditions is at disposal, while for the temperature dependent studies a second Ultra High Vacuum (UHV) BEEM setup has been constructed and built.

This thesis is structured as follows: The second chapter is concerned with the theoretical background of hot electron transport in BEEM. The creation of the hot electrons, the subsequent hot electron transport through the base towards the semiconductor and the influence of the collector band structure is discussed. Chapter three addresses the construction of the new BEEM-setup, the characterization of the setup itself and the preparation of the samples. All experimental results obtained during this thesis are shown and discussed in chapter four. In order to understand the underlying magnetization behavior and to extract magnetization configurations of the spin valve, the magnetic anisotropies are determined by Ferromagnetic Resonance (FMR). They serve as input for simulations of hysteresis loops, which are analyzed with respect to hysteresis loops obtained by BEEM and Magneto Optic Kerr effect (MOKE). By variation of the thickness of the layers involved in the base we determine the spin dependent attenuation lengths, which reflect hot electron transport along the vicinity of the [100]-axis of the bcc $Fe_{34}Co_{66}$ and of the fcc Au layer. To clarify the microscopic origin of the magnetocurrent, we replace one of the bcc $Fe_{34}Co_{66}$ layers by an approximately equally thick bcc Fe layer and investigate these samples at different temperatures. These results are discussed with respect to transport models taking electronic band structure effects into consideration, evaluating the spin contrast. At the very end a compact overview of the most relevant results of this work is given.

We conclude this introduction with the same words as we have used at the beginning. We investigate excited states and processes within ferromagnetic materials by exposing them to an incident beam of low energy electrons. These interact with the ferromagnetic metal by relaxing elastically, inelastically and even spin dependently, though these are not the electrons to be detected. Quite the contrary, the characteristics of the remaining, mostly unscattered and through the ferromagnetic film ballistically transmitted electrons are recorded to reveal transport properties of the thin film.

2 Theory of Hot Electron Transport

This chapter is concerned with a systematic discussion of hot electron transport in BEEM. We start by discussing the creation of the hot charge carriers and highlight their subsequent relaxation and propagation within the metallic base. We proceed by investigating the energy and momentum filter properties of the semiconducting collector and end up by explaining the measured characteristics.

2.1 The emitter - creation of hot electrons

A metallic tip of a scanning tunneling microscope operated in constant current mode provides the electron source in BEEM experiments, see Fig.2.1. A feedback circuit adjusts the tunneling (emitter-base) gap keeping the tunneling current I_T constant. In doing so, the emitter becomes a constant current source of hot electrons, which is quite favorable for the investigation of the subsequent hot electron transport. On the contrary, STM operation in constant height mode (i.e. feedback off) enforces the tunneling (emitter) current I_T to vary upon changes of the tunneling voltage U. This situation is given in device based experiments, for instance in MTT's, where a constant tunneling gap is provided by the thickness of an insulating layer. Since the collector current is provided by a small fraction of electrons originating from I_T, the I_TU-characteristic superimposes the I_CU-characteristic complicating the interpretation of hot electron transport. Both approaches reveal different kinds of I_CU-characteristics so that the transfer ratio is introduced in order to get a comparable physical quantity. T is defined as

$$T = I_C/I_T. \tag{2.1}$$

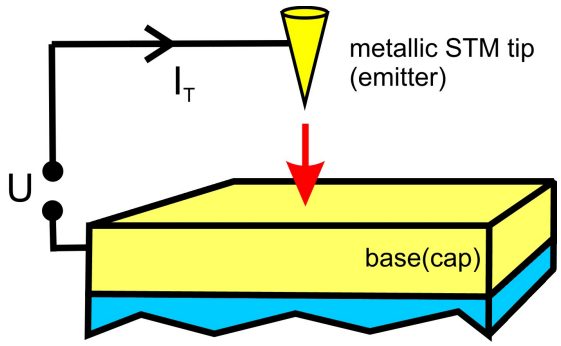

Figure 2.1: By applying a tunneling voltage an electron flow off the STM-tip into the metallic base is created. Within the base electrode the tunnel injected electrons are in a state of nonequilibrium and referred to as hot electrons.

Experiments, like MTT's or BEEM, are common base transistor approaches and T equals the dc current gain α being limited to values below 1. The major advantage of device based experiments is the feasibility to create large tunneling currents of the order of mA and consequently large collector currents of the order of µA, see for instance [32]. In STM/BEEM experiments I_T is limited to much lower values of the order of nA-µA. Accordingly, the collector current in BEEM experiments is commonly found in the low pA-regime at best and recording of $I_C U$-characteristics requires a well tuned setup.

The emitter creates a bunch of hot electron paths in the base manifested by hot electron distributions in momentum and energy space. Since the Schottky barrier at the base/collector interface will finally select some of these paths to build up I_C, we first should have a more precise insight into the tunneling process appearing in this work. It comprises a metallic (gold) STM-tip in tunneling distance to the uppermost metallic (gold) cap layer of the base electrode. We describe this system by two gold electrodes with free electron like properties separated by a vacuum gap d in a planar geometry. Tunneling is treated to be instantaneous and non perpendicular tunneling is neglected. The net flow of tunneling electrons N between two biased electrodes can then be approximated by a model proposed by Simmons [33] according to

$$\begin{aligned} N &= \frac{J_T}{e} \\ &= \frac{4\pi m}{h^3} \int_0^{E_m} dE_\perp \int_0^{\infty} dE_{||}\, D(E_\perp)\,(f(E) - f(E+eU)) \end{aligned} \tag{2.2}$$

with E_m being the energy of the barrier maximum, h Planck's constant, $f(E)$ the Fermi function and m the electron mass, respectively. The electron energy E consists of components $E_\perp$ and $E_{||}$ for transport perpendicular and parallel to the surface, respectively. $D(E_\perp)$ denotes the tunneling probability, which will be substituted by the one dimensional Wentzel-Kramers-Brillouin (WKB) tunneling term [33] assuming that the electron wavelength is small compared to the tunneling distance. One arrives therefore at

$$\begin{aligned} D(E_\perp) &= D(E_x) \\ &= \exp\left\{-\frac{4\pi}{h}\int_{s_1}^{s_2} \left[2m\,(V(x) - E_x)\right]^{1/2}\, dx\right\}, \end{aligned} \tag{2.3}$$

which represents the probability for one electron to tunnel along the direction $\hat{\mathbf{x}}$ through the potential barrier $V(x)$ with its spatial boundaries s_1 and s_2. Note that the zero level of the energy scale is set to the lowest conduction band edge of the emitter in the following. By assuming the barrier to be of rectangular shape the effect of an applied bias voltage is reflected in an average barrier height of $\overline{\Phi} = \Phi_{Au} + E_F - \frac{1}{2}eU$, see Fig.2.2(a). The integral of formula 2.3 can then be solved to [33]

$$D(E_x) \cong \exp\left(-\frac{4\pi d\sqrt{2m}}{h}\sqrt{\Phi_{Au} + E_F - \frac{1}{2}eU - E_x}\right) \tag{2.4}$$

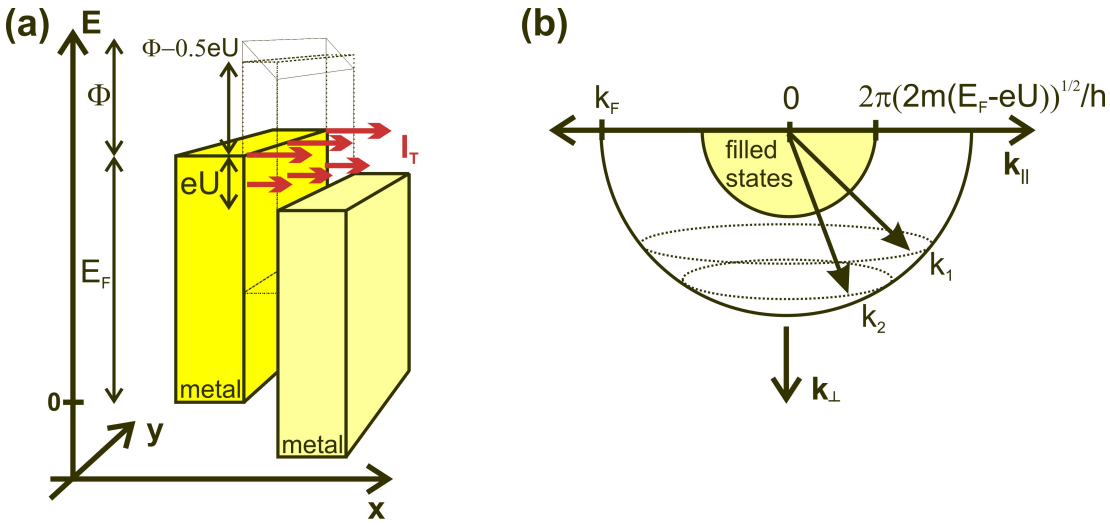

Figure 2.2: Electron tunneling visualized in energy (a) and momentum space (b).

with $d = s_2 - s_1$ denoting the tunneling distance, Φ_{Au} the gold work function (assumed to be 4.7 eV) and E_F the Fermi-energy of gold (assumed to be 9.4 eV as extracted from [34]). After substitution of equation 2.4 in equation 2.2 the integral becomes

$$N = \frac{4\pi m}{h^3}\int_0^{E_m} dE_\perp \int_0^{\infty} dE_{||}\, \exp\left(-\frac{4\pi d\sqrt{2m}}{h}\sqrt{\Phi_{Au}+E_F-\frac{1}{2}eU-E_\perp}\right) \times\left(\frac{1}{e^{\beta(E-E_F)}+1}-\frac{1}{e^{\beta(E+eU-E_F)}+1}\right) \tag{2.5}$$

with $\beta = k_B T$ and k_B the Boltzmann constant. We neglect here the fact that the STM feedback circuit dynamically adjusts the tunneling distance d keeping up a constant tunneling current I_T. Valuable information, however, can still be gained from this model by assuming a constant d with typical values of STM operation.

The evaluation of the integral in equation 2.5 can be visualized in energy or momentum space, see Fig.2.2. The largest contribution to the tunneling current originates from the energy interval between E_F and $E_F - eU$, where a majority of occupied emitter states is able to tunnel into a majority of unoccupied base states. The description in **k**-space is similar. One considers two semi Fermi spheres accounting for electrons incident on the metal vacuum interface in both gold electrodes [15]. The outer radius equals k_F and the inner radius is $\sqrt{2m\,(E_F - eU)}/\hbar$. In **k**-space the largest contribution to I_T is given by the half shell, which is created by subtracting the two Fermi semi-spheres of the electrodes.

2.1.1 Hot electron momentum distribution

For sketching the tunneling process in **k**-space we consider the two Fermi spheres shown in Fig.2.2(b). One sphere accounts for emitter electrons incident on the metal vacuum interface, while the other one reflects free final states in the base electrode. Electrons propagating along different directions exhibit a different rate or flux for the impact onto the metal vacuum interface per time and contribute therefore unequally to I_T. At a constant electron energy a measure for the flux is given by the surface of the corresponding emitter energy semi-sphere. Let us additionally consider a finite and constant energy component $E_{||} = E - E_{\perp}$. A measure for the flux is then the corresponding circumference of the energy sphere, as sketched by the dashed tracks spanned by the vectors $\mathbf{k_1}$ and $\mathbf{k_2}$ in Fig.2.2. The electron flux is therefore enhanced at larger energy components $E_{||}$ but at the cost of a reduced energy component $E_{\perp}$ determining the tunneling probability $D(E_{\perp})$. To highlight these two competing effects and their result on the momentum (angular) distribution of the tunnel injected electrons, we substitute $E_{\perp} = E\cos^2\Theta$ and $E_{||} = E\sin^2\Theta$ in equation 2.5 as a consequence of decomposing the free electron wave-vector **k** into its components $k_{\perp} = k\cos\Theta$ and $k_{||} = k\sin\Theta$. Θ denotes the angle between the electron wave-vector **k** and the perpendicular axis of the interface, see Fig.2.3. In doing so, formula 2.5 can be rewritten and becomes

$$N = \frac{4\pi m}{h^3}\int_0^{\pi/2} d\Theta \int_0^{E_m/\cos^2\Theta} dE\, E\sin(2\Theta) \times D(E,\Theta)\left(f(E) - f(E+eU)\right). \quad (2.6)$$

To depict the hot electron momentum distribution, we numerically execute the second integral using a Monte Carlo method implemented in a Fortran code. The result is plotted in Fig.2.4 for $d = 0.5\,\text{nm}$ and $d = 1\,\text{nm}$. Most of the electrons are injected at an angle $\Theta_{\max}$ of $8° - 9°$ for d=1 nm and $12° - 13°$ for d=0.5 nm for bias voltages U ranging from 0.7 to 3 V. The width of the momentum distribution is defined as the angle Θ', where the peak value decays by a factor of e^{-1}. We find $\Theta' = 18° - 19°(\Theta' = 2°)$ for d=1 nm and $\Theta' = 28°$ ($\Theta' = 3°$) for d=0.5 nm for angles larger (smaller) than $\Theta_{\max}$. The dip towards $\Theta = 0$ reflects the reduced number of electrons impinging onto the interface per time for $k_{||} \to 0$ [15]. Hence, significant contributions to I_T originate from

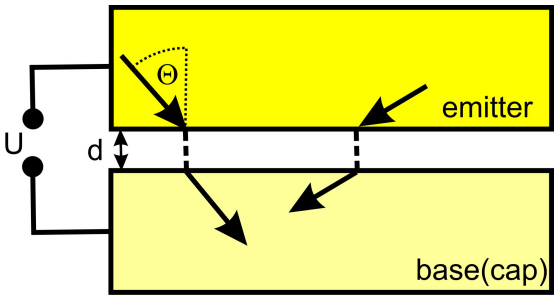

Figure 2.3: The tunneling current I_T is naturally built up by electrons impinging onto the tunneling interface at different angles Θ.

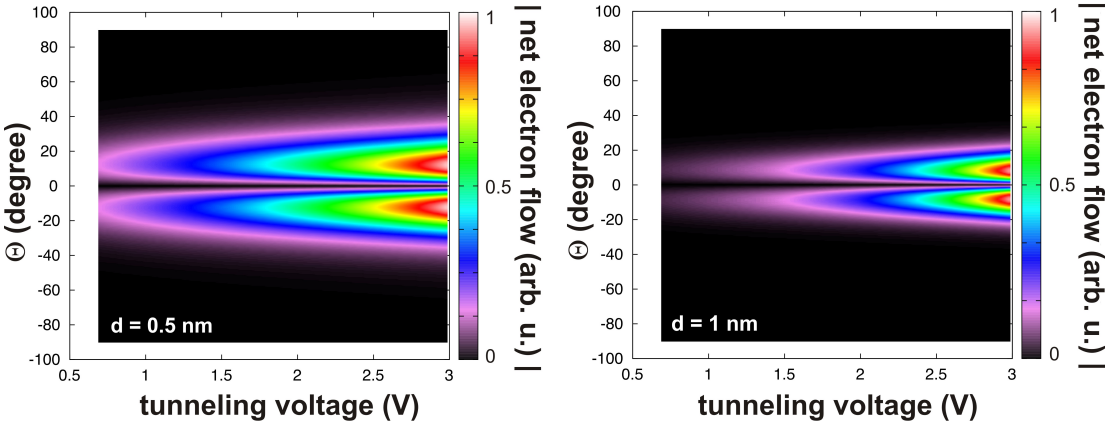

Figure 2.4: Hot electron momentum distribution of tunnel injected electrons across a tunneling gap of 0.5 and 1 nm between two gold electrodes.

electrons having a small momentum component parallel to the interface, giving rise to a forward focused tunneling emission cone with a dip around $\Theta = 0$.

2.1.2 Hot electron energy distribution

To reveal the energy distribution, we have to sum up the angular distribution of the hot electrons at constant electron energies. This requirement is met by executing the first integral of equation 2.6, which we carry out analytically. The result is plotted in Fig.2.5. The maximum of the energy distribution is found slightly below the Fermi energy of the emitter. This feature stems from the product of the Fermi function $f(E)$ for $T > 0$ and the exponential tunneling probability $D(E_\perp)$ of the integrand [23]. The maximum of $N(E)$ shifts from 40 to 70 meV (50 to 90 meV) below E_F of the emitter with increasing U for $d = 1$ nm (d=0.5 nm). The calculation demonstrates furthermore that the tunneling current I_T is provided by electrons of an energy interval at least several hundred meV broad at full width of half maximum particularly for larger tunneling voltages, see also [23, 35]. The equivalence of tunneling voltage and hot electron injection energy becomes therefore obscured for $|U| > 100$ mV[1].

In conclusion, we have simulated the tunneling conditions appearing in this thesis within a free electron model. Tunneling between emitter and base stems mostly from electrons of energies slightly below the emitter Fermi energy and the relevant electron energy interval spreads over some hundred meV for typical tunneling voltages employed in BEEM. The injected hot electrons enter the base electrode within a forward focused

[1] To create quasi-monoenergetic hot electrons for a wider range of tunneling voltages, a degenerate semiconductor can be used as STM-tip. In this case the energy distribution is limited to a small range between the conduction band edge of the tip and the Fermi level [35].

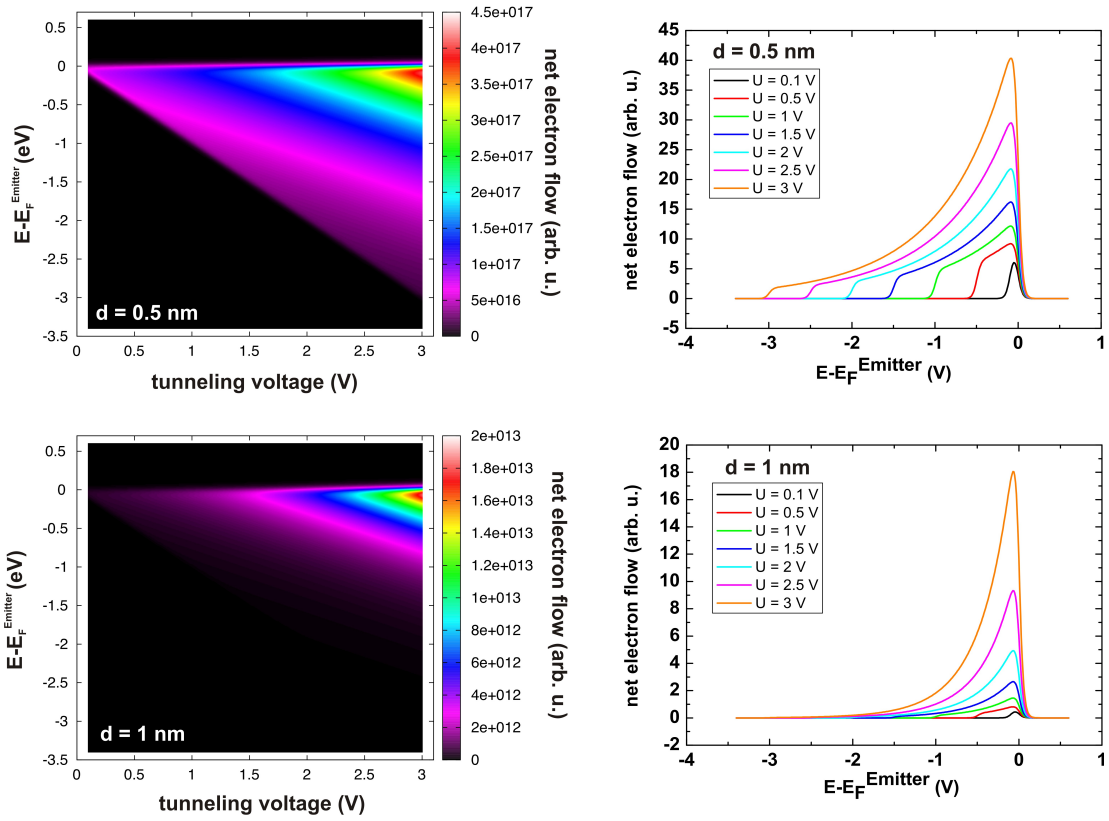

Figure 2.5: Hot electron energy distribution provided by tunneling across a gap of $d =$ 0.5 and 1 nm using two gold electrodes.

cone, though with a reduced probability for $\mathbf{k}_{||} \to 0$.

So far, we have disregarded the real electronic bandstructure of the electrodes, which is shown in Fig.2.6 for the fcc gold cap layer. In addition, the crystallinity of the STM-tip remains unknown. By including Fig.2.6 into our discussion we have to focus on states located in the vicinity of the [100]-axis (Γ-X direction) or on states around $\overline{\Gamma}$, which is the perpendicular direction with respect to the base surface. For growing electron energies exceeding 1.1 eV a band gap around $k_{||} = 0$ opens up and electrons are injected with an increasing nonzero momentum component $k_{||}$. Furthermore, electrons may be partly injected into a surface band, which is degenerated with bulk states and exists around $\overline{\Gamma}$ as calculated for the perfect clean (100)-surface[1], see Fig.2.6(c).

[1] Any modification of the perfect surface may further sensitively vary the dynamics of excited electrons in the surface area.

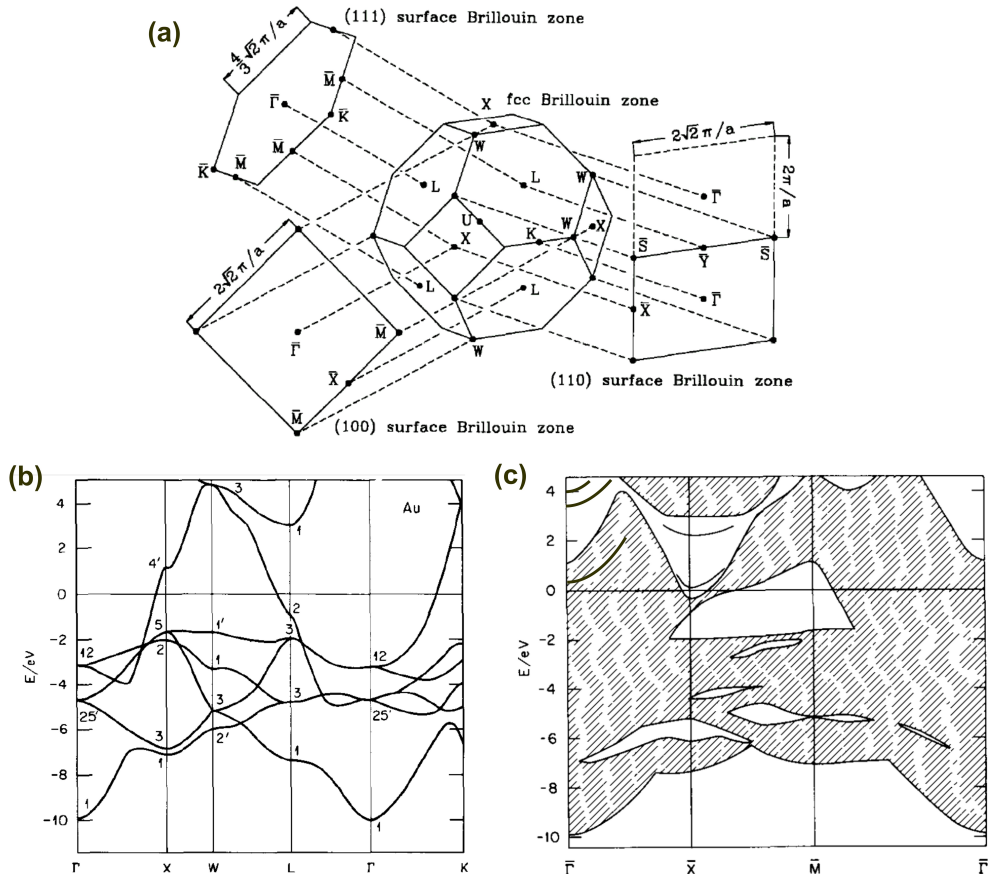

Figure 2.6: Bulk and surface Brillouin zones of a fcc-crystal (a). Electronic band structure of fcc Au and of the corresponding (100)-oriented surface (b and c). Surface states around $\overline{\mathrm{X}}$ and $\overline{\Gamma}$ are shown as solid lines. Graphs are extracted from [36] and [37]. Surface bands around $\overline{\Gamma}$ are extracted from [20] and added to (c).

2.2 The base - hot electron propagation and relaxation

Tunnel-emission provides a nonzero population of excited electronic states in the base of energies and wave-vectors beyond E_F and k_F, respectively. Elastic and inelastic scattering processes within the thin base reduce this degree of nonequilibrium giving rise to electron relaxation towards the equilibrium Fermi surface. Simultaneously, the injected electrons are also transported towards the base/collector interface as a consequence of the forward focused emission. We can use Matthiesen's approximation to gain the overall hot electron relaxation Γ from all microscopic relaxation channels Γ_i [20]

$$\begin{aligned} \Gamma &= \hbar/\tau \\ &= \Gamma_{\mathrm{e-e}} + \Gamma_{\mathrm{e-ph}} + \Gamma_{\mathrm{e-m}} + \Gamma_{\mathrm{e-plasm}} + \Gamma_{\mathrm{el}}. \end{aligned} \tag{2.7}$$

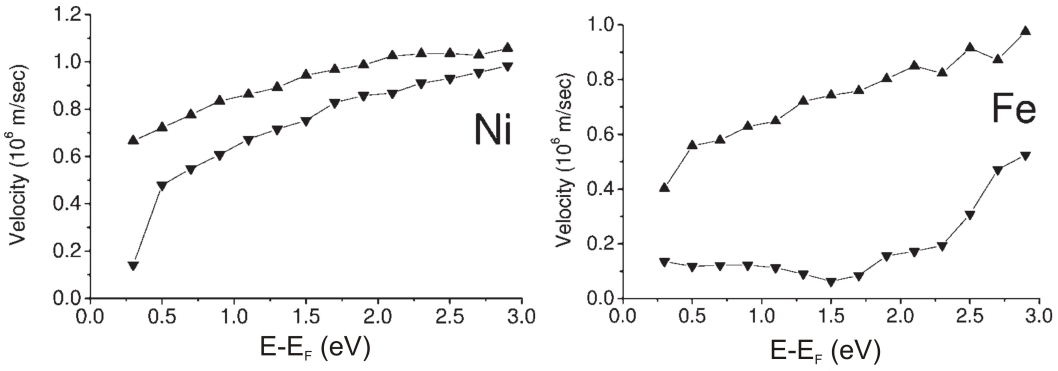

Figure 2.7: Calculated momentum averaged, spin resolved electron velocities in Ni and Fe. Up (down) triangles denote majority (minority) spin hot electrons. Figures extracted from [21].

Γ features the dimension of an energy and can be measured as the linewidth broadening in spectroscopy experiments. Using Heisenberg's uncertainty principle $\Delta E \Delta t = \hbar$, we can correlate Γ with the electron lifetime τ being the time passing during electron transport across a distance of one mean free path Λ. For an electronic state $(\mathbf{k}, n, \sigma)$ with n being the band index and σ the electronic spin it holds

$$\Lambda(\mathbf{k}, n, \sigma) = v(\mathbf{k}, n, \sigma)\tau(\mathbf{k}, n, \sigma) \tag{2.8}$$

while v denotes the electronic group velocity. The latter is given by the first derivative $\partial E/\partial k$ of the dispersion relation and is therefore spin dependent for a ferromagnet, compare Fig.2.7 [21]. Furthermore, it is meaningful to differentiate τ and Λ by inelastic and elastic contributions according to

$$\frac{1}{\Lambda} = \frac{1}{\Lambda^{\text{inel}}} + \frac{1}{\Lambda^{\text{el}}} \tag{2.9}$$

$$\frac{1}{\tau} = \frac{1}{\tau^{\text{inel}}} + \frac{1}{\tau^{\text{el}}} \tag{2.10}$$

in order to match the availability of experimental data. Photoelectron Spectroscopy revealed an interesting feature [38]:

The inelastic mean free path Λ^{inel} of low energy electrons for transition metals with unoccupied d-like states is measured to be shorter compared to noble metals with completely occupied d-like states .

The so-called universal curve of metals, i.e. the dependence of the inelastic mean free path as function of electron energy, becomes material dependent at low electron energies and the universality is canceled. This behavior can be understood with Fermis

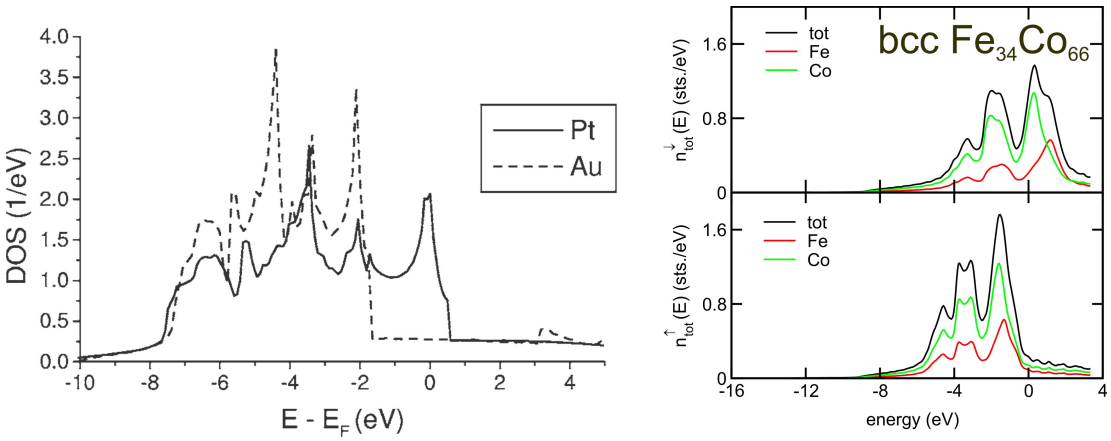

material	λ [nm] (U=1 V)	Ref.	technique
Pt	4	[16]	BEEM
Au	13	[40]	BEEM
$Fe_{16}Co_{84}$	5.7 (majority spin)	[39]	MTT
	0.8 (minority spin)		

Figure 2.8: Spin resolved density of states and scattering lengths for hot electrons in Pt, Au and bcc $Fe_{34}Co_{66}$. When a majority of unoccupied states is available for hot electron decay, λ is reduced. Graphs extracted from [21, 41].

golden rule determining the transition probability W between electronic states i and f in first-order perturbation theory according to

$$W = \frac{2\pi}{\hbar} \sum_j |< f_j|H'|i >|^2 \rho_j \tag{2.11}$$

with H' and ρ_j being the perturbation Hamiltonian and the density of final states per unit of energy, respectively. The sum is carried out in energy space and respects final states being accessible at different energy levels. Incoming hot electrons scatter therefore more likely, if there are more final hole states (i.e. unoccupied states) hot electrons can decay into. In the case of ferromagnetic metals almost completely and only partially occupied d-like states exist simultaneously in one material but for each kind of spin, a situation which is given, for instance, in Co rich FeCo alloys. The determination of the corresponding scattering length λ for excited electrons shows accordingly a large spin asymmetry $\lambda_M/\lambda_m > 5$ [39]. When one compares the unoccupied part of the density of states with experimentally determined scattering lengths for a variety of materials, the correspondence is even more evident, see Fig.2.8.

Within the framework of the golden rule approach we also understand the energy dependence of the inelastic lifetime τ^{inel}, which is experimentally accessible by 2Photon-

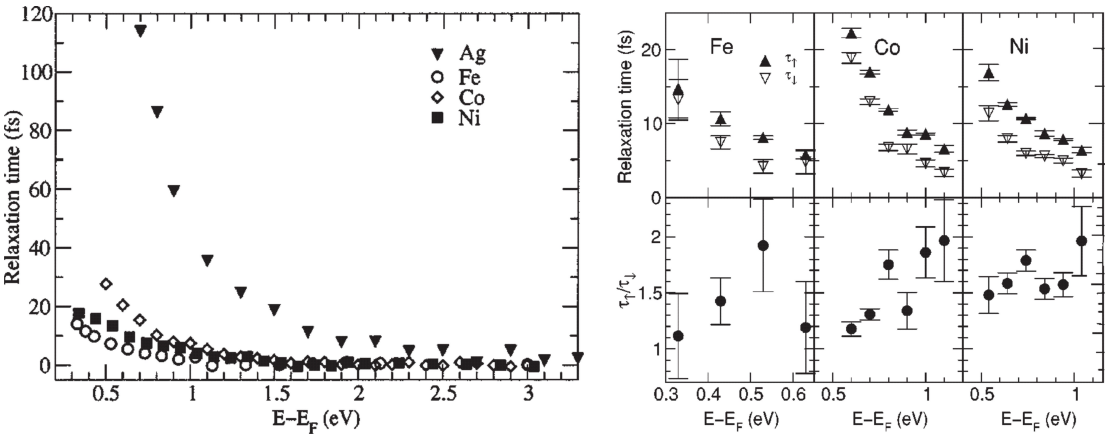

Figure 2.9: Spin averaged (left) and spin resolved (right) inelastic lifetimes for Ag and the three transition metals Fe, Co and Ni. Figures extracted from [42].

Photoemission or by STM [21, 42, 43], see Fig.2.9. The experimental values for τ^{inel} are of the order of fs and monotonically reduced with increasing electron energy since a larger amount of final states becomes accessible at elevated electron energies. On the contrary, elastic contributions to τ and Λ are not as directly accessible in experiments. These depict scattering at impurities, grain boundaries and interfaces. τ^{el} and Γ^{el} become therefore a function of the crystalline quality and may differ when results of different sample series are compared to each other.

Apart from the spin asymmetry of the group velocity we should also highlight the scattering mechanisms ruling the spin asymmetry of the lifetime in order to understand spin contrast in hot electron transport. For this task it is meaningful to calculate the hot electron transfer time through the metallic base and to compare it to the lifetimes τ_i of different scattering mechanisms i. Assuming a base thickness of 15 nm and typical values for the group velocity of $0.2 - 1.2 \times 10^6$ m/s yields base transfer time amounting to 12-75 fs, only.

2.2.1 Electron-electron scattering

Several experiments and calculations demonstrate that the most effective inelastic relaxation channel in the hot electron regime in metals is given by collisions with the bath of thermalized (cold) electrons [20, 42, 43]. Electrons experience each other via their own Coulomb potential. This is screened to some extent by other conduction electrons in the surroundings reducing the scattering cross section and limiting the interaction range. During collision a part of the initial hot electron energy and momentum is transferred to the thermalized electrons. These become on their part excited and leave hot holes in the conduction bands below E_F. In other words, secondary electron-hole pairs

are created during relaxation of primary hot electrons, compare Fig.2.10. A strict condition underlying this kind of scattering is given by Pauli's exclusion principle demanding that hot electrons of energy E only interact with conduction electrons of energies larger than $2E_F - E$ (T=0 K). A scattering event emerges only when primary hot electron and secondary electron are transmitted into previously unoccupied electronic states.

In a BEEM experiment secondary electrons may on their part contribute to I_C provided they gain sufficient energy and adequate momentum to be transmitted into the semiconductor. The significance of this non ballistic process in HET's is verified by excitation spectroscopy experiments (SBEEM and SBHEM) [8, 44–47] revealing a small but growing influence on I_C with increasing tunneling voltage. In non-magnetic materials no spin order of secondary electrons is provided[1]. On the contrary, ferromagnetic materials exhibit an intrinsic spin polarization in the energy intervals $[E_F, 2E_F - E]$ and $[E_F, E]$, which are relevant for the excitation of secondary electrons[2]. As far as secondaries contribute to I_C their spin polarization also enters the total hot electron spin polarization P, which is reflected in the magnetocurrent value. But the intrinsic spin polarization in the relevant energy intervals for secondary electrons does not correspond to the large values of P extracted from magnetocurrent values of several hundred percent. The contribution of the secondary electron spin polarization to the magnetocurrent is therefore generally less than that of the primary hot electrons in BEEM experiments.

Within a golden rule approach the rate of electron-electron relaxation is given by the sum of all final state energies E' and $\epsilon + E - E'$ of the primary and secondary electrons, respectively. The latter sum has to be further weighted with the number of all initial secondary states of energy ϵ as

$$\begin{aligned}\tau^{-1}_{\mathrm{e-e,M(m)}} &= \frac{2\pi}{\hbar}\int_{E_F}^{E} dE'\,(1-f(E'))\,\rho_{M(m)}(E') \\ &\quad\times\int_0^{E_F} d\epsilon\,\Big[f(\epsilon)\rho_{M(m)}(\epsilon)\,(1-f(\epsilon+E-E'))\,\rho_{M(m)}(\epsilon+E-E') \\ &\quad+ f(\epsilon)\rho_{m(M)}(\epsilon)\,(1-f(\epsilon+E-E'))\,\rho_{m(M)}(\epsilon+E-E')\Big] \\ &\quad\times\left|\alpha(E-E')\right|^2, \end{aligned} \tag{2.12}$$

while E reflects the energy of the incoming primary electrons. The energy transfer in a single event equals therefore $E - E'$. ρ reflects the density of states and $\alpha(E - E')$ the matrix element connecting initial and final states by the screened Coulomb interaction.

[1] This situation is particularly interesting within the spacer layer of a spin valve, where an incident spin polarized hot electron beam may loose a part of its spin order due to excitation of secondary electrons of opposite spin.

[2] If the relaxed primary electron is of opposite spin orientation than the secondary electron, one may treat the secondary hole below E_F combined with the primary relaxed electron as a Stoner pair.

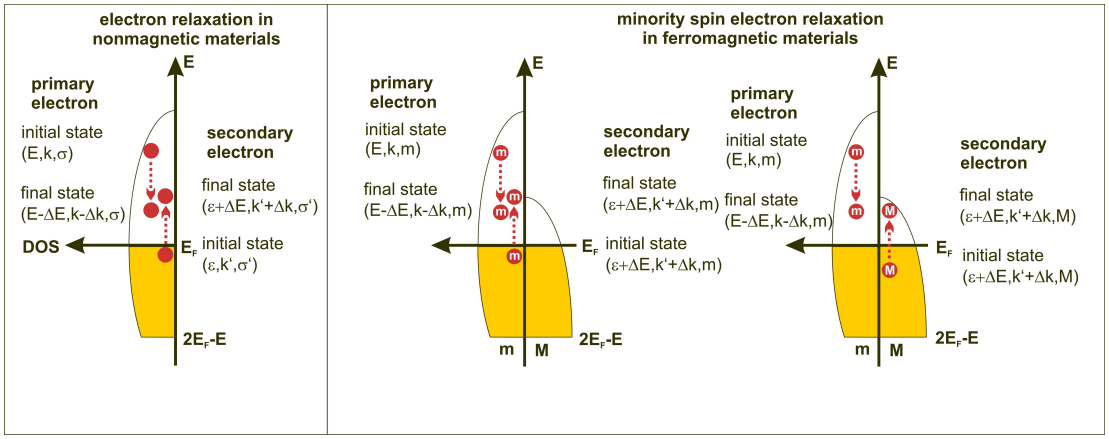

Figure 2.10: Sketch of hot electron collisions with thermalized electrons in non-magnetic (left) and ferromagnetic materials for the case of minority spin scattering (right). Energy and momentum of incoming (primary) hot electrons are partly transferred to thermal electrons exciting a secondary electron-hole pair. The energy interval for secondary electron excitation is shown in yellow.

Assuming spin degeneracy and α and ρ to be energy independent, formula 2.12 collapses to the well known equation [48]

$$\tau_{\mathrm{e-e}}^{-1} = \frac{\pi}{\hbar}\rho^3 \left|\alpha\right|^2 (E - E_F)^2 . \tag{2.13}$$

In experiments with excited electrons in the noble metals Cu and Ag this behavior is evident in the total inelastic part of the electron lifetime τ^{inel} [1, 43] and, furthermore, reveals that electron-electron relaxation rules the total lifetime τ^{inel}, see Fig.2.9. Though applicable to some simple metals the approximation of constant density of states breaks down for hot electron decay in transition metals [48, 49]. Unoccupied d-like states above E_F and even occupied states below E_F influence considerably the energy dependence of $\tau_{\mathrm{e-e}}$ [49–52].

Typical values of $\tau_{\mathrm{e-e}}^{\mathrm{inel}}$ from Fig.2.9 are of the order of $1 - 10\,\mathrm{fs}$ for electron energies above 1 eV [1, 20, 42, 43]. Taking into account the typical base transfer time in BEEM (12-75 fs) and an average energy loss of about 2/3 of the initial electron energy, as predicted by self energy approaches [17], the efficiency of electron-electron relaxation in hot electron experiments becomes evident. Although we expect a more complex energy dependence of $\tau_{\mathrm{e-e}}$ for transition metals, we can still presume an almost monotonic decay with increasing electron energy due to monotonic growing of the final phase space [1, 42, 43].

2.2.2 Electron-phonon scattering

Electrons couple to phonons as well since they experience the ion Coulomb potential of each atom. Hot electrons thermalize therefore by absorbing and emitting phonons opening up a channel to transfer energy and momentum to the lattice. Phonons are either thermally generated or they are spontaneously emitted by excited electrons. The latter process exists even at $T = 0\,\mathrm{K}$ [53] and may create phonons up to the maximum phonon energy $\hbar\omega_{\max}$. While the corresponding electron energy relaxation can be referred to as quasi-elastic due to a maximum energy transfer $\hbar\omega_{\max}$ of the order of $\Delta E \approx 10\,\mathrm{meV}$ per scattering event, the impact on momentum relaxation is larger. Even electron backscattering is facilitated. Since this relaxation channel is weakly inelastic, just a fraction of the spin dependent free phase space in ferromagnetic materials is sampled when compared to electron-electron scattering.

Hot electron lifetimes $\tau_{\mathrm{e-ph}}$ due to phonon interaction can be determined by angle resolved photoemission spectroscopy (ARPES), time resolved Kerr experiments and by theoretical approaches [1, 49, 54–56]. These are found to be of the order of 10 fs at room temperature and larger at lower temperatures. For this work we assess $\tau_{\mathrm{e-ph}}$ to be less than $10^2\,\mathrm{fs}$, which is larger than $\tau_{\mathrm{e-e}}$ but still comparable to the base transfer time. Hence, electron-phonon scattering is generally significant in BEEM transport experiments. Note that $\tau_{\mathrm{e-ph}}$ is also $\mathbf{k}$-dependent and may gain/loose strength in some points of $\mathbf{k}$-space [20]. The assessment of $\tau_{\mathrm{e-e}} < \tau_{\mathrm{e-ph}}$ and the fact that electron-electron scattering samples a much larger phase space strongly suggests that phonon scattering processes contribute only little to the magnetocurrent with respect to electron-electron scattering. A direct fingerprint of a strong influence of phonons to the spin dependence of hot electron transport is a magnetocurrent, which is reduced at lower temperatures.

We analyze now the manifestation of electron-phonon relaxation in HET experiments, i.e. its energy and temperature dependence. We consider the Eliashberg spectral function $\alpha(\omega)^2F(\omega,\mathbf{k})$ denoting the strength of electron-phonon coupling multiplied by the phonon density of states. With respect to hot electron relaxation it follows [20, 57–59].

$$\begin{aligned}\Gamma_{\mathrm{e-ph}}(\omega) &= \frac{\hbar}{\tau_{\mathrm{phonon}}} \\ &= 2\pi\hbar\int_0^{\omega_{\max}} d\omega'\,\alpha(\omega')^2F(\omega')\left\{1 - f(\omega-\omega') + 2n(\omega') + f(\omega+\omega')\right\}\end{aligned} \tag{2.14}$$

with $n(\omega')$ and $\omega_{\max}$ being the Bose-Einstein distribution and the maximum phonon frequency, respectively. Equation 2.14 represents the possibility to fill an electronic hole state with an initial electron of energy $E = \hbar\omega$ via a phonon of frequency ω' to provide energy and momentum. By simulating the phonon system via a three dimensional Debye model one gets for $\omega_{\max}$

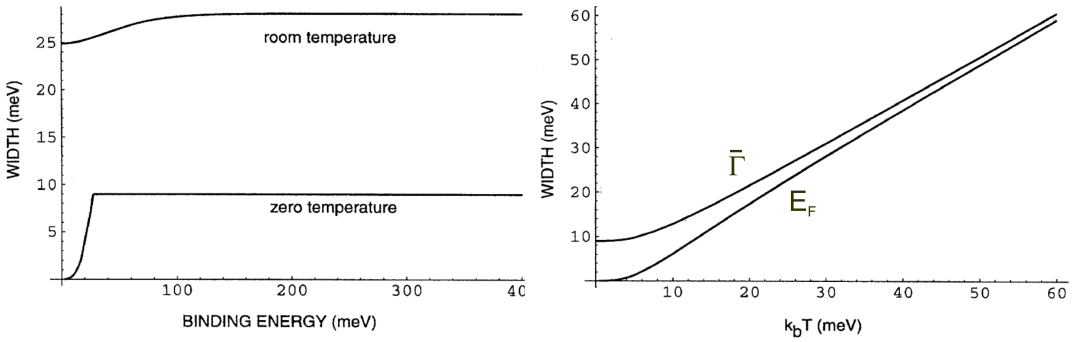

Figure 2.11: Phonon contributions to the peak linewidth in angle resolved photon emission spectroscopy (ARPES) of the Cu(111) surface state at ($\overline{\Gamma}$) as a function of binding(hole) energy (left) and as a function of temperature for the two binding energies $E = E_F$ and $E = E(\overline{\Gamma})$ (right). Graphs extracted from [54].

$$\omega_{\max} = \begin{cases} E/\hbar & \text{for} \quad E < \hbar\omega_D \\ \omega_D & \text{for} \quad E \geq \hbar\omega_D \end{cases} \tag{2.15}$$

with ω_D being the Debye frequency. Using a constant electron-phonon coupling strength α the low temperature limit($T = 0\,\mathrm{K}$) can be expressed to [20]

$$\alpha^2 F(\omega) = \begin{cases} \lambda_p \left(\frac{\omega}{\omega_D}\right)^2 & \text{for} \quad E < \hbar\omega_D \\ 0 & \text{for} \quad E \geq \hbar\omega_D \end{cases} \tag{2.16}$$

$$\Gamma_{\mathrm{e-ph}}(\omega) = 2\pi\hbar \int_0^{\omega_{\max}} d\omega'\, \alpha^2 F(\omega') \tag{2.17}$$

$$= \begin{cases} \frac{2}{3}\pi\hbar\lambda_p\omega_D \left(\frac{\omega}{\omega_D}\right)^3 & \text{for} \quad E = \hbar\omega < \hbar\omega_D \\ \frac{2}{3}\pi\hbar\lambda_p\omega_D & \text{for} \quad E = \hbar\omega \geq \hbar\omega_D \end{cases} \tag{2.18}$$

with λ_p being the electron-phonon mass enhancement parameter, a quantity which reflects the electron-phonon coupling strength. The last equation demonstrates a nonzero electron relaxation rate at $T = 0\,\mathrm{K}$, which is exclusively mediated by phonon emission [57]. Furthermore, $\Gamma_{\mathrm{e-ph}}$ becomes constant for electron energies exceeding the maximum phonon energy $E > \hbar\omega_D$. This behavior is evident in the very related surface state studies using ARPES, compare Fig.2.11.

Since we have highlighted the energy dependence of electron-phonon scattering, we proceed to focus on the temperature dependence of $\Gamma_{\mathrm{e-ph}}$. In the high temperature limit ($T >> \hbar\omega_{\max}/k_B$) $\Gamma_{\mathrm{e-ph}}$ scales linearly with T according to

$$\Gamma_{\mathrm{e-ph}} = 2\pi\lambda_p k_B T \tag{2.19}$$

This behavior changes slightly at lower temperatures, see Fig.2.11.

2.2.3 Electron-magnon scattering

Magnons are quantized collective excitations (spin waves) in ferromagnets decreasing the global magnetic moment by two Bohr magnetons μ_B per magnon. Carrying a spin of 1 oriented antiparallel with respect to the spins of the host ferromagnetic lattice, magnons can be emitted by minority spin and absorbed by majority spin electrons, only. Magnon mediated electron relaxation reverses therefore the electronic spin. Phonon-magnon interaction accounts for thermally excited magnons, which fits experimentalists with a control to vary the magnon population by temperature. Like for electron-phonon scattering the spontaneous emission of magnons is possible even at T=0 K [18]. Since emission is prohibited for majority spin electrons, a source of spin asymmetry in hot electron relaxation is given by this process. Note that no phase space arguments have been included yet. Other relaxation mechanisms, like electron-electron scattering whose Coulomb interaction is naturally spin independent, account for a spin asymmetry by sampling a spin dependent phase space.

With regard to the magnon dispersion relation we expect that a scattering event may reduce the hot electron energy up to the maximum magnon energy $\hbar\omega_{\max}$. This attains values of several hundred meV for magnon wave-vectors at the Brillouin zone boundary, see Fig.2.12 [60–62]. Hence, magnon contributions are certainly significant when electron energies smaller than $\Phi_{SB} + \hbar\omega_{\max}$ are used in BEEM-experiments. But there is also a strong impact on momentum relaxation, which is as strong as in the case of phonon scattering. Hot electrons may be transferred to undetectable states due to the large momentum exchange provided by the emission of large **k**-vector magnons. Spontaneous magnon emission is therefore believed to contribute significantly to minority spin electron relaxation and therefore to the magnetocurrent, as well. Spontaneously emitted magnons are also in a state of nonequilibrium and therefore referred to as hot magnons. They thermalize on their part via phonons and electron-hole pairs of opposite spin orientation (Stoner excitations). Note that secondary electrons created by the latter process cannot influence BEEM-experiments, since Φ_{SB} generally exceeds the largest magnon energy $\hbar\omega_{\max}$.

Let us now focus on the fraction of thermally excited spin waves. They may act in a twofold manner. Magnons having an almost vanishing wave-vector parallel to the interfaces ($k_{||} \approx 0$) reverse the electron spin, but carry and transfer only low energy and low momentum. Hence, hot electrons scattered by this mechanism will still be detectable in BEEM as a quasi-ballistic contribution. Any spin contrast is then reduced due to the spin mixing contribution of magnons. On the other hand, magnons with a larger wave-vector $k_{||}$ act like phonons as out-scatterers, i.e. they remove hot electrons from the acceptance cone of the collector. Taking into account available final electronic states in the relevant energy interval $[E, E \pm k_B T]$ absorption of thermally excited

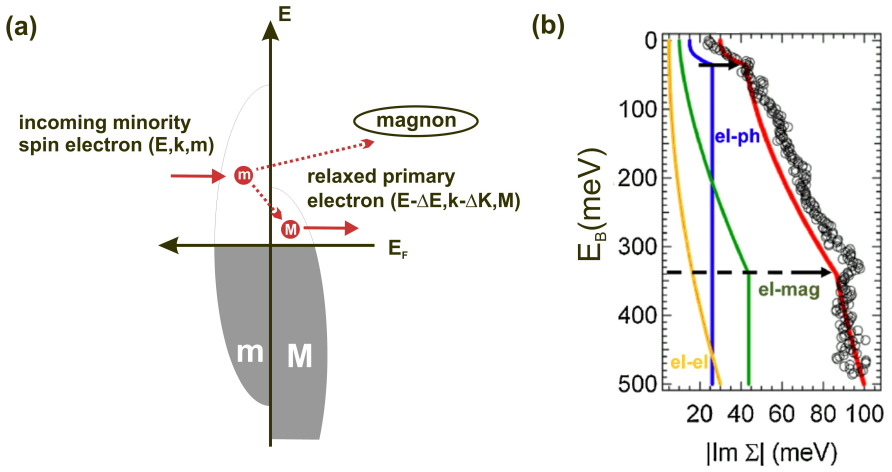

Figure 2.12: Sketch of spontaneous magnon emission: Aside from energy and momentum, also angular momentum is transferred from the electronic system to the magnonic system, which induces spin flip processes (a). ARPES study on Ni(110) (b) revealing the significance of spontaneous magnon emission. The abbreviations el-el, el-ph and el-mag reflect electron-, phonon- and magnon-mediated electron relaxation. Graphs extracted from [63].

magnons is favored compared to emission, since we can assume that more unoccupied minority spin states are present than majority spin states. Such a behavior strengthens relaxation of incoming majority spin electrons. Hence, at lower temperature we can expect an increase in spin contrast since out-scattering and spin-mixing processes freeze out.

We can understand the energy dependence of electron-magnon relaxation within the same formalism as already used for electron-phonon relaxation. $\Gamma_{\mathrm{e-m}}$ can be modeled with the Eliashberg function by substituting the corresponding magnon parameters [64]. At $T = 0\,\mathrm{K}$ we can therefore write

$$\Gamma_{\mathrm{e-m}} \sim \int_0^{\omega_{\max}} d\omega' \alpha_m^2 F(\omega') \tag{2.20}$$

$$\omega_{\max} = \begin{cases} E/\hbar & \text{for} \quad E < \hbar\omega_0 \\ \omega_0 & \text{for} \quad E \geq \hbar\omega_0 \end{cases} \tag{2.21}$$

with ω_0 and $F(\omega)$ being the maximum magnon energy and magnon density of states, respectively. If we simulate the magnon system via Bloch's 3/2 power law reflecting a parabolic dispersion relation $E(q) = Dq^2$, while D is the spin wave stiffness, we get

$$\alpha_m^2 F(\omega) = \lambda_m \frac{1}{4\pi^2} D^{-3/2} \sqrt{\omega} \tag{2.22}$$

$$\Gamma_{\mathrm{e-m}} = \begin{cases} \frac{\lambda_m}{6\pi^2} D^{-3/2} \omega^{3/2} & \text{for} \quad E = \hbar\omega < \hbar\omega_0 \\ \frac{\lambda_m}{6\pi^2} D^{-3/2} \omega_0^{3/2} & \text{for} \quad E = \hbar\omega \geq \hbar\omega_0 \end{cases} . \tag{2.23}$$

λ_m is the electron-magnon mass enhancement parameter, which is reported to be comparable in magnitude to λ_p [63, 64].

Experimental information about this relaxation channel can be extracted from spin polarized electron energy loss spectroscopy (SPEELS), ARPES and temperature dependent transport studies using ferromagnetic HET-devices. SPEELS directly evidences the significance of spontaneous magnon emission and ARPES confirms the energy dependence of the scattering rate, see Fig.2.12 again [60, 61, 65]. On the other hand, device based experiments reveal that spin mixing due to thermally excited magnons is mostly active within the bulk of ferromagnetic layers rather than at the interfaces [20, 54, 66, 67]. Furthermore, these results demonstrate a temperature scaling in agreement with Bloch's 3/2 power law. The electronic lifetime $\tau_{\mathrm{e-m}}$ associated with this kind of scattering can be extracted from SPEELS and time resolved Kerr effect (TR-MOKE) experiments revealing $\tau_{\mathrm{e-m}}$ is typically of the order of 10 fs [1, 61]. Comparing this value to the time of flight of hot electrons through the base we perceive the significant impact of magnons for the hot electron decay.

Although electron-magnon scattering is not as inelastic as electron-electron scattering, a large energy and momentum transfer may occur within a single scattering event due to the spontaneous emission of magnons. The latter removes mostly minority spin hot electrons from the acceptance cone of the semiconductor. Thus, this kind of relaxation is discussed to be one of the sources of spin contrast in hot electron transport [61, 68].

2.2.4 Electron-defect scattering

Another crucial aspect for this transport experiment is given by hot electron relaxation at lattice defects. These may act as elastic scatterers randomizing any electron directionality and favoring an isotropic electron distribution. The non-ideal match of the lattice constants of the epitaxially grown base layers leads to a finite defect density, which is, a priori, not negligible. The mismatch equals approximately 1-2 % at each interface (relevant lattice constants: $a_{\mathrm{Au}} = 0.41/\sqrt{2}$ nm, a_{FeCo}=0.284 nm, a_{GaAsP}=0.562 nm, a_{Fe}=0.287 nm) so that stacking faults and vacancies are regularly built into the epitaxial lattice at the interfaces. However, lattice strain relaxes within the bulk of the layers so that defect scattering matters mostly on lateral and less on perpendicular scales for ultrathin films. The spatial defect distribution will contribute to the standard deviation of electron attenuation by averaging characteristics obtained on different probing locations on the sample. Though completely single crystalline layer stacks, which accompany no grain boundaries, are employed, the impact of defects on hot electron attenuation cannot be completely excluded at this point.

2.2.5 Electron-plasmon scattering

Bulk plasmons require an energy of several eV to be excited due to an offset in the plasmon dispersion relation at $\mathbf{k} = 0$. However, plasmon excitation is favored at metallic surfaces as reflected in a dispersion relation scaling via $\omega \sim \sqrt{k_{||}}$ [20, 49]. The latter case holds only, when a metallic band gap accompanied by surface states confines electrons at the surface, so that a two dimensional electron gas is created [20]. Evidence for such excitations is given, for instance, by inelastic tunneling spectroscopy [69–72].

For this work we omit this kind of relaxation since bcc Fe(100) and $Fe_{34}Co_{66}(100)$ provide no energy gap at $\overline{\Gamma}$ within the relevant energy interval. The condition above is, furthermore, not fulfilled for fcc Au(100), where one surface band being degenerated with bulk states exists, see again Fig.2.6.

2.2.6 Electron relaxation at the surface

Due to the existence of the surface resonance band on the fcc Au(100)-surface we have to consider that electrons can also be injected into these states rather than directly into bulk states, compare Fig.2.6. Surface states exhibit a distinct electronic dispersion relation depending on $\mathbf{k}_{||}$, while $\mathbf{k}_{\perp}$ equals zero. Hot electrons in this surface band suffer the same relaxation mechanisms as mentioned above and are transferred either into intraband states or into the continuum of bulk states as interband processes. Both processes provide a finite value for Γ_{e-surf} [73–76]. Since in this thesis the continuum of bulk states provides a much larger phase space for tunnel injection, we do not expect any significant influences of this surface band.

2.2.7 Electron relaxation and optical excitations

Electrons may relax, furthermore, by emitting photons via inter- and intraband processes [77]. However, this kind of scattering is reported to be negligible for metallic films with respect to the relaxation channels mentioned above, see [69].

2.2.8 Spin-orbit interaction

As the electron passes through the lattice of positively charged atom cores, its spin experiences a magnetic field in its coordinate frame, which we know as spin-orbit coupling. As a consequence, the pure spin character of electronic bands is lost and replaced by a weighted degeneration of majority or minority spins. This behavior is particularly visible at spin hybridization points (spin hot spots), where scattering events of electrons accompany a significant chance of spin flips giving rise to a reduction of spin order (spin relaxation).

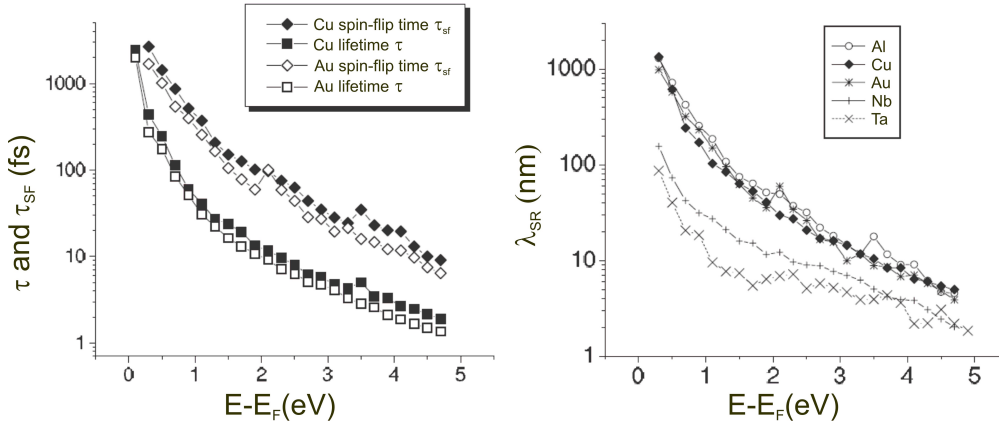

Figure 2.13: Calculated momentum averaged inelastic lifetime τ, spin-flip time τ_{SF} (left) and corresponding spin relaxation lengths (right). Graphs extracted from [78].

In metals spin-orbit coupling is commonly treated within the Elliott-Yafet mechanism, which is the most important mechanism among other spin orbit type effects [78–80]. Valid close to electronic equilibrium this theory associates electron relaxation triggered by phonon- and impurity scattering to spin relaxation [78]. By raising the electron energy into the hot electron regime, however, the most effective relaxation channel is given by electron-electron interaction. This altered situation is modeled by the authors of [78]. They claim that inelastic relaxation of excited electrons is essentially faster than relaxation in spin space, so that hot electrons maintain their spin order after inelastic relaxation down to E_F, as shown by the spin flip times τ_{SF} and electronic lifetimes τ of Fig.2.13.

These results are supported by a HET study [81]. The authors investigate the hot electron analogon to the anisotropic magnetoresistance (AMR), i.e. the anisotropic magnetocurrent. The spin-orbit induced attenuation of the collector current for NiFe and Co is about 1 % only in agreement with long spin relaxation times of the order of $10^2 - 10^3$ fs.

Both experiments strongly indicate that spin-orbit induced effects have only a minor influence on hot electron transport in BEEM.

2.3 The collector - hot electron filtering

Electrons, which have passed the base layers, impinge onto the base/collector interface, where they experience the Schottky barrier as an energy and momentum filter. Electrons with sufficient energy may be transmitted into the semiconductor, while relaxed electrons do not overcome the Schottky barrier and are prevented from entering. This

behavior results in $I_C U$-characteristics showing an onset of I_C for tunneling voltages equivalent to Φ_{SB}.

2.3.1 Electron reflection and refraction

The Schottky barrier is a potential step and, within a free electron model, it separates materials of different effective electron masses. One of the consequences is that electrons crossing the interface are subject to refraction effects, see Fig.2.14. $k_{||}$ is conserved for electron motion parallel to ideal flat interfaces, while the opposite holds for $k_{\perp}$. With regard to the effective electron mass we use for the metallic base the free electron mass m and for the semiconductor a different value m^*. The apex point of the presumed parabolic dispersion relation in the metallic base is set as the energy zero level in the following. In doing so, electron motion parallel to the interfaces in the metal as well as in the semiconductor can be expressed by [82]

$$E_{||}^{\text{metal}} = \frac{\hbar^2}{2m} k_{||}^2 \tag{2.24}$$

$$E_{||}^{\text{sc}} = \frac{\hbar^2}{2m^*} k_{||}^2. \tag{2.25}$$

By combining the last two equation one arrives at

$$E_{||}^{\text{sc}} = \frac{m}{m^*} E_{||}^{\text{metal}}. \tag{2.26}$$

Conservation of the overall electron energy claims further

$$E = E_{\perp}^{\text{metal}} + E_{||}^{\text{metal}} \tag{2.27}$$

$$= E_{\perp}^{\text{sc}} + E_{||}^{\text{sc}} + E_{SB} \tag{2.28}$$

with $E_{SB} = E_F^{\text{metal}} + \Phi_{SB}$. By combining equations 2.26 and 2.28 we get for hot electron motion perpendicular to the interface

$$E_{\perp}^{\text{sc}} = E - E_{||}^{\text{sc}} - E_{SB} \tag{2.29}$$

$$= E_{\perp}^{\text{metal}} - E_{||}^{\text{metal}} \left(\frac{m}{m^*} - 1 \right) - E_{SB} \tag{2.30}$$

demonstrating that $E_{\perp}^{\text{sc}} < E_{\perp}^{\text{metal}}$. Thus, electrons slow down their perpendicular motion by crossing the metal/semiconductor interface for $m^* < m$ and $E_{SB} \neq 0$. On the other hand, motion parallel to the interface gains energy when $m^* < m$, see equation 2.26. Hot electrons crossing the interface are therefore refracted away from the perpendicular axis for $\Theta \neq 0$ [82], see Fig.2.14. By increasing the angle of electron incidence to a value Θ_c, electron refraction turns to total reflection. Electrons able to cross the interface account for

$$k_{\perp}^{\text{sc}} \geq 0. \tag{2.31}$$

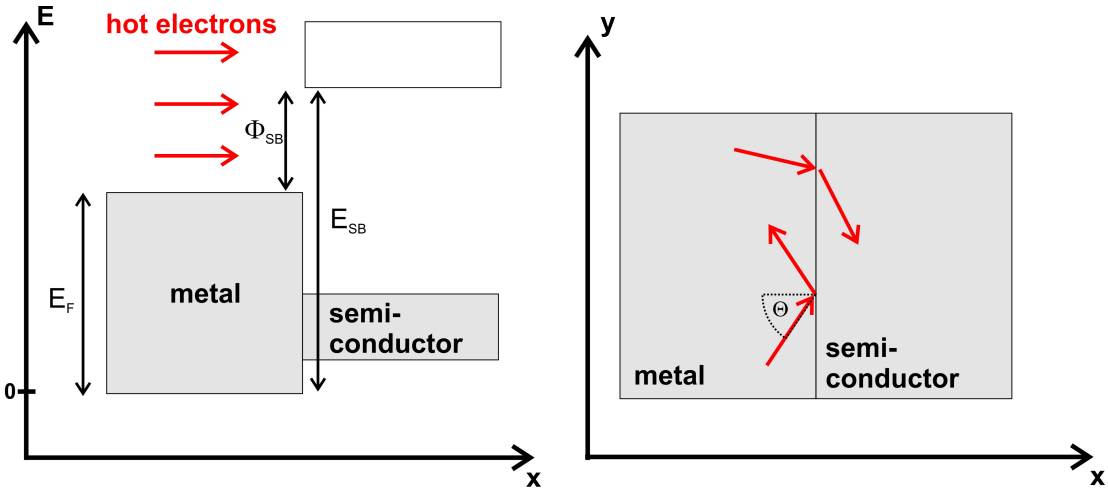

Figure 2.14: The band structure used for deriving the critical angle of acceptance at the metal/semiconductor interface (left). Electrons incident non perpendicularly on the interface are subject to refraction and total reflection effects.

We rewrite this condition using equation 2.29 to

$$k_{||}^{\mathrm{sc}} \leq \sqrt{\frac{2m^*}{\hbar^2}\,(E - E_{SB})}. \tag{2.32}$$

The angle Θ of electron incidence is correlated to the electron wave-vector $\mathbf{k}$ as

$$\sin\Theta = \frac{k_{||}}{k} \tag{2.33}$$

$$= \frac{k_{||}}{\sqrt{2mE/\hbar^2}}. \tag{2.34}$$

By combining equation 2.32 and 2.33 we find for the critical angle Θ_c

$$\sin\left(\Theta\right)^2 = \frac{k_{||}^2}{2mE/\hbar^2} \tag{2.35}$$

$$\Theta_c = \arcsin\sqrt{\frac{m^*}{m}\frac{E - E_{SB}}{E}} \tag{2.36}$$

Like the electron tunneling cone, the last equation defines an acceptance cone for the semiconductor. Note that this argument holds for electron transmission across any energy barrier. Electrons with $\Theta < \Theta_c$ are transmitted into the semiconductor otherwise they are reflected back into the base layers. In order to estimate the magnitude of Θ_c, let us consider the case of gold grown onto GaAs(100). For $\Phi_{SB} = 0.8\,\mathrm{eV}$, $E_F = 9.4\,\mathrm{eV}$, $m^*/m = 0.069$ and $E = E_F + \Phi_{SB} + 0.1\,\mathrm{eV}$ one gets $\Theta_c \approx 1.5°$ from formula 2.36. Thus, only electrons with an almost normal incidence may enter the semiconductor collector. This very narrow acceptance cone overlapping with the similarly narrow tunneling

emission cone facilitates microscopy in the ballistic regime, since almost any hot electron scattering event in the base transfers hot electrons to undetectable states outside the acceptance cone so that these electrons are lost for the collector current. The lateral resolution Δx in BEEM is then determined by

$$\Delta x \quad = \quad 2d \tan \Theta_c(E, m^*) \tag{2.37}$$

with d being the overall base thickness. For instance, $\Theta_c = 1.5°$ yields $\Delta x = 1\,\mathrm{nm}$ in the case of $d = 20\,\mathrm{nm}$. The critical acceptance angle $\Theta_c(E, m^*)$ increases with electron energy as a result of the parabolic shape of presumed free electron like bands. In the same manner the lateral resolution decreases with increasing tunneling voltage.

When the electron energy is raised further, conduction band valleys at different **k**-points of the Brillouin zone are accessible for hot electron transmission, which degrades the lateral resolution aside from formula 2.37. The Schottky barrier depends on the electronic wave-vector **k**, because the barrier height is given by the difference between the Fermi level[1] and the **k**-dependent conduction band edge of the semiconductor. Note that in other experiments the Schottky barrier height Φ_{SB} commonly refers to the special case of the lowest potential step height, only.

In the following we approximate the conduction band characteristic of $GaAs_{67}P_{33}$ within a free electron approach by using various **k**-dependent Schottky barrier heights $\Phi_{SB,i}$ for each conduction band valley located at different points i within the Brillouin zone. Each valley comprises its own effective electron mass m_i^* and its own critical angle of acceptance $\Theta_{c,i}$, so that electrons incident on the interface experience a bunch of acceptance cones. For $\Theta_{c,i}$, we have to respect the location of the band valley apex with regard to the surface Brillouin zone center $\overline{\Gamma}$. If their projection do not overlap (off-axis states), electron transmission into the minimum of the corresponding parabolic bands requires a nonzero $k_{||,i}$-component or a nonzero angle of incidence Θ_i. This requirement is not given for on-axis states, whose parabolic apex point projects onto $\overline{\Gamma}$, see Fig.2.15.

For $GaAs_{67}P_{33}$ we have to consider $i \in \{\Gamma_{1c}, X_{1c}, X_{3c}, L_{1c}\}$. Satellite valleys at the L_{1c} and X_{1c} points are available at an injection energy of $0.16\,\mathrm{eV}+\Phi_{SB,\Gamma}$ and, additionally, at X_{3c} at an injection energy of $0.41\,\mathrm{eV}+\Phi_{SB,\Gamma}$ [86]. Ballistic transport into the apex of the L-valleys requires an electron transport at a minimum angle of incidence of $\Theta_L = 36°(42°)$ with respect to the perpendicular [100]-axis of the bcc $Fe_{34}Co_{66}$(Fe)-layers according to

$$\sin(\Theta_i) \quad = \quad \frac{k_{||,i}}{k_{\max}}. \tag{2.38}$$

L-valleys account for $k_{||,L} = 7.9\,\mathrm{nm}^{-1}$ according to a lattice constant of $a = 0.562\,\mathrm{nm}$ for $GaAs_{67}P_{33}$. Performing the same calculation again, transport into X-valleys requires

[1] In the case of III-V semiconductors the Fermi-level is pinned at the metal/semiconductor interface within the semiconductor gap [83–85].

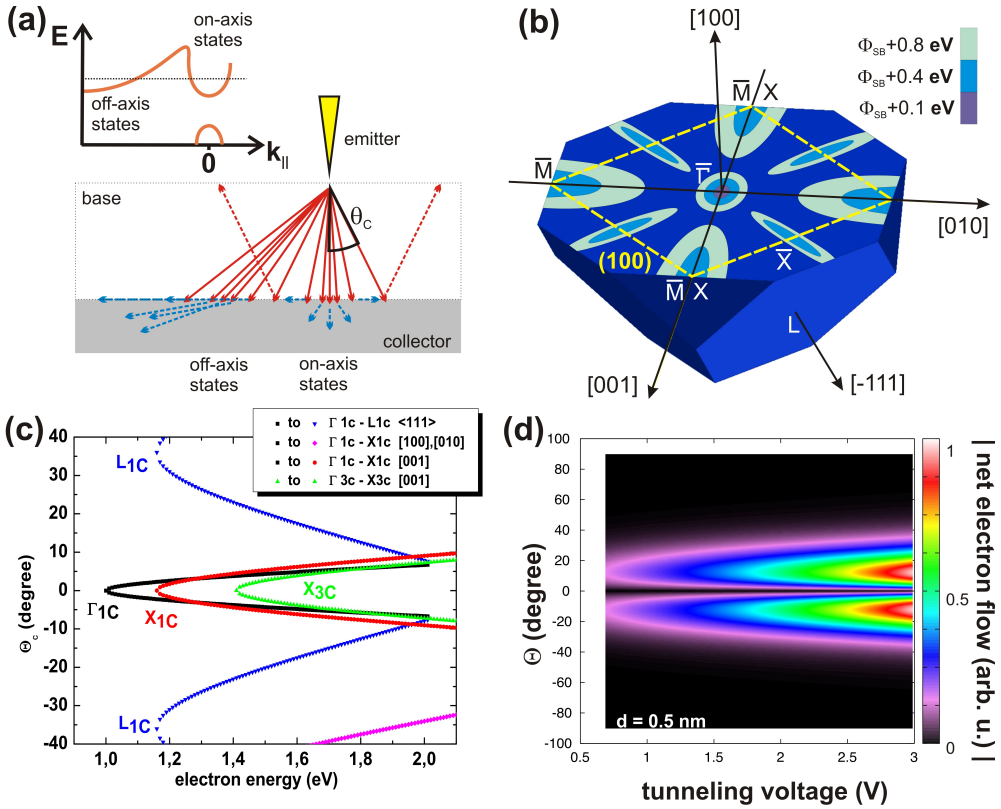

Figure 2.15: Sketch of the angular dependence of electron transmission into $GaAs_{67}P_{33}$ (a). Unoccupied conduction band states of $GaAs_{67}P_{33}$ as a function of $k_{||}$ for three electron energies (b). The critical angle of hot electron transport for the $Fe_{34}Co_{66}/GaAs_{67}P_{33}$-interface calculated with formula 2.40 (c) and the tunneling emission cone of the emitter for a tunneling gap of 0.5 nm (d). Both permit ballistic electron transport only at small angles Θ, i.e. normal to the film plane.

an angle of $\Theta_X = 56°(69°)$ and 0° according to $k_{||,X} = 11.1$ and $0\,\mathrm{nm}^{-1}$. $k_{\max}$ is extracted from the bandstructures of bcc $Fe_{34}Co_{66}$ and bcc Fe and assumed to have an average value of $0.61 \times 2\pi/b$ and $0.54 \times 2\pi/c$, respectively, in the energy range of 1.3 up to 2.5 eV above the Fermi level [41]. b and c are the corresponding lattice constants and assumed to be 0.2835 nm and 0.2858 nm, respectively [87]. To reveal the critical angle of the relevant off-axis acceptance cones we use formula 2.36 and, for the sake of simplicity, we shift the corresponding acceptance cones by the offset determined by $k_{||,i}$. In order to cover more features of the real band structure, longitudinal and transversal effective masses $m^*_{l(t)}$ are introduced with their nonparabolicity parameters α. We extract m^*_Γ of $GaAs_{67}P_{33}$ and Φ_{SB} from [44], the Fermi-energy from [88] and utilize for the remaining variables the values of GaAs approximately, which we extract from [89] ($\Phi_{SB}(Fe_{34}Co_{66}/GaAs_{67}P_{33})$=$\Phi_{SB}(Fe/GaAs_{67}P_{33})$=1 eV, $m^*_\Gamma = 0.089m$, $m^*_{L,l} = 1.9m$,

$m^*_{X,l} = 1.3m$, $m^*_{X,t} = 0.23m$, $\alpha_\Gamma = 0.69\,\mathrm{eV}^{-1}$, $\alpha_L = 0.65\,\mathrm{eV}^{-1}$, $\alpha_X = 0.5\,\mathrm{eV}^{-1}$). We arrive therefore at

$$\Theta_{c,i} = \arcsin\sqrt{\frac{m^*_{l(t),i}(1+\alpha_i(E-\Phi_{SB,i}-E_F))}{m}\frac{E-E_{SB,i}}{E}} \tag{2.39}$$

which becomes

$$\Theta_{c,i} = \arcsin\sqrt{\frac{m^*_{l(t),i}(1+\alpha_i(E-\Phi_{SB,i}))}{m}\frac{E-\Phi_{SB,i}}{E+E_F}} \tag{2.40}$$

by referring all electron energies to E_F (assumed to be 9.1 eV for $Fe_{34}Co_{66}$ and 8.8 eV for Fe [88]) rather than to the lowest conduction band point of the base. With $\Theta_{c,i}$ and the offset of the conduction band valleys we can depict the electronic bandstructure of the semiconductor $GaAs_{67}P_{33}$ as a function of Θ rather than the wave-vector, see Fig.2.15 for the case of $Fe_{34}Co_{66}/GaAs_{67}P_{33}$. The situation for $Fe/GaAs_{67}P_{33}$ (not shown) is very similar except that electron refraction is reduced and off-axis valleys appear consequently at larger angles of incidence.

Due to the narrow tunneling distribution of Fig.2.15(d) peaking at small angles Θ combined with the narrow acceptance cones of the semiconductor of Fig.2.15(c) electrons are preferentially transmitted into on-axis ($k_{||} \approx 0$) semiconductor valleys near $\overline{\Gamma}$. However, a growing but still relatively small overlap via off-axis L-valley states is visible for larger tunneling voltages until Γ- and L-valleys merge.

Furthermore, electrons cover a longer distance through the base and are more attenuated when they are transported non-perpendicularly. To estimate the magnitude of this effect let us consider ballistic electron transport towards the L-point for $Fe_{34}Co_{66}/GaAs_{67}P_{33}$. The corresponding fraction of the collector current, which we name $I_C^{\overline{X}}$ (L projects onto $\overline{X}$ of the (100)-surface Brillouin zone), suffers therefore more attenuation compared to $I_C^{\overline{\Gamma}}$, according to

$$\frac{I_C^{\overline{X}}}{I_C^{\overline{\Gamma}}} \sim \frac{\exp\left(-\frac{d/\cos(\Theta_L)}{\lambda}\right)}{\exp\left(-\frac{d}{\lambda}\right)}. \tag{2.41}$$

For an overall base thickness of d =20 nm combined with an average attenuation length of λ =6 nm $I_C^{\overline{X}}$ is suppressed to about 50 % of $I_C^{\overline{\Gamma}}$.

Though additional conduction band valleys contribute for larger voltages U and the directionality of electron selection at the metal/semiconductor interface is reduced, I_C is still built up of hot electrons transported almost perpendicularly in the vicinity of the [100]-axis of the bcc $Fe_{34}Co_{66}$ and bcc Fe lattice. With regard to Fig.2.15(c) and formula 2.37 we assess, in this way, a lateral resolution of approximatively 10 nm for BEEM with tunneling voltages less than -3 V. These statements hold only provided the transport through the base layers involves weak scattering and is dominantly of

ballistic origin. Only with the existence of strong scatterers in combination with a non-conservation of $k_{||}$ at the base layer interfaces a large contribution of non-perpendicular electron paths to the collector current seems to be likely, compare [89].

2.3.2 The shape of the Schottky barrier

2.3.2.1 The depletion zone

In the last paragraph we have addressed electron reflection and refraction at a **k**-dependent step-like barrier within a free electron approach. The Schottky barrier, however, is of a more complex shape. Next to the interface the electron density of the semiconductor becomes depleted within a zone of width W given by

$$W = \sqrt{\frac{2\epsilon\epsilon_0 \left(U_{bi} - U_{BC}\right)}{eN_d}} \tag{2.42}$$

with U_{bi} being the built-in potential, U_{BC} an external voltage applied between base and collector, $\epsilon(\epsilon_0)$ the dielectricity constant of the semiconductor(vacuum) and N_D the dopant density. This effect arises from an electron redistribution from the semiconductor towards the metal and towards interface states [83]. The resulting electric built-in field E_{bi} bends the electronic bands. A high dopant density reduces the depletion zone width and electron tunneling through the Schottky barrier may be facilitated. Hot electron filtering at the Schottky barrier sensitively deteriorates then and partly or completely thermalized electrons (leakage currents) contribute to the low ballistic currents to be measured. For n-doped $GaAs_{67}P_{33}$ with $N_d = 5 \cdot 10^{16}$ cm^{-3} we calculate a depletion zone width of $W = 160\,\text{nm}$ assuming $\epsilon = 12.2$ and $U_{bi} = 1\,\text{V}$. Tunneling is therefore relevant only at the very top of the Schottky barrier, where the zone width becomes quadratically small. A low doping level enhances the depletion zone and reduces the electric built-in field[1]. The latter affects hot electrons within the depletion zone by accelerating them towards the semiconductor bulk, where they finally thermalize before flowing into a current detector. Moreover, a nonzero E_{bi} prevents thermalized electrons within the semiconductor from flowing back into the base so that they are forced into the detector [27]. This current detector should be connected to the semiconductor by a low resistance demanding an ohmic back contact.

In conclusion, the doping density N_D of the semiconducting collector has to be chosen properly in HET-experiments to suppress the influence of leakage currents and to enable the electrons to flow into the current detection system.

[1]Note that the intrinsic charge carrier density of GaAs and Si is about $2 \cdot 10^6\,\text{cm}^{-3}$ and $2 \cdot 10^{10}\,\text{cm}^{-3}$ at room temperature.

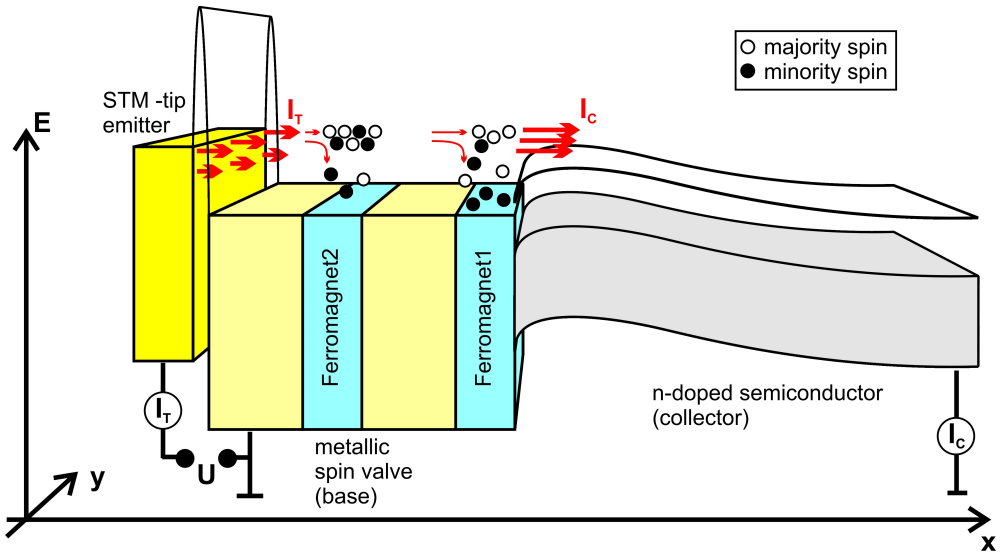

Figure 2.16: Sketch of the spatial electronic bandstructure in BEEM (top panel). The tunneling and Schottky barrier are smoothed due to image potential effects, while the spin valve base impresses spin contrast on I_C.

2.3.2.2 Image potential effect and quantum-mechanical reflection

Electrons incident on a barrier are also subject to an image potential effect, which leads to an attractive Coulomb like potential at the interface. In this way, electrons incident on the metal/semiconductor interface experience a Schottky barrier, whose maximum is lowered by a value $\Delta\Phi$ and shifted by a distance Δx towards the semiconductor bulk. Moreover, the barrier shape becomes smoothed rather than being an abrupt one. For BEEM-experiments the tunneling and the Schottky barrier are modified due to this effect but the impact on the latter one is much more crucial, see Fig.2.16. We can calculate the resulting $\Delta\Phi$ and Δx from [90]

$$\Delta\Phi_{SB} = \sqrt[4]{\frac{e^6 N_D \left(eU_{bi} - k_B T\right)}{8\pi^2 \epsilon^3 \epsilon_0^3}} \tag{2.43}$$

$$\Delta x = \frac{1}{4}\sqrt[4]{\frac{e^2}{2\pi^2 \epsilon\epsilon_0 N_D \left(eU_{bi} - k_B T\right)}} \tag{2.44}$$

$$eU_{bi} = \Phi_{SB} - eU_{BC} - \zeta, \tag{2.45}$$

where ζ is the difference between the semiconductor work function and the electron affinity. $\Delta\Phi_{SB}$ can be estimated to be 40 meV for $GaAs_{67}P_{33}$, which is small with respect to $\Phi_{SB} \cong 1\,\text{eV}$ [44]. On the other hand, Δx equals 1.6 nm, which is not any more negligible. The probability of electron backscattering into the base is increased, in particular, for tunneling voltages only slightly larger than Φ_{SB}. This effect is mostly me-

diated by semiconductor phonons [91] and enhanced in the region between the metallic interface and the barrier maximum [6].

Another backscattering effect at the metal/semiconductor interface arises due to the quantum-mechanical nature of the incoming electrons demanding the conservation of the amplitude and gradient of the wave-function. Even for electron energies larger than the step height and matching conducting states the transmission probability is smaller than one and the incident electron wave may be reflected back. With increasing electron energy reflection decreases scaling with a square-root behavior [91].

These two effects combined with the large phase space mismatch at the metal/semiconductor interface suppresses hot electron transmission across the Schottky barrier to an extent of a few percent, only [91]. Hence, this interface is the bottleneck for ballistic currents in BEEM. This statement is in agreement with $I_C U$-characteristics reflecting the semiconductor bandstructure [92]. Relaxation and transport effects of the base layers are generally not so obvious and more hidden in the $I_C U$-characteristics.

2.3.3 Spectroscopy and microscopy

2.3.3.1 Spectroscopy

Hot electron relaxation in the base and electron transmission across the metal/semiconductor interface are encoded in the $I_C U$-characteristics. The first model to interpret these spectra was given by Bell and Kaiser in 1988 [92]. It is based on a planar tunneling formalism incorporating a free electron like transmission across the base/collector interface, see Fig.2.17(a). The latter condition accounts for the following two requirements

$$\begin{aligned} E_{||} &\leq E_{||,\max} \\ &= \frac{m^*}{m-m^*}\left(E_\perp - E_F + eU - \Phi_{SB}\right) \qquad (2.46) \\ E_\perp &\geq E_{\perp,\min} \\ &= E_F - eU + \Phi_{SB}. \qquad (2.47) \end{aligned}$$

The electronic bandstructure of the semiconductor is approximated by parabolic conduction bands with effective masses m^* and the zero energy level is set at the conduction band minimum of the emitter. Thus, we can express the $I_C U$-characteristic like the $I_T U$-characteristic, yet, with integration boundaries reflecting the restrictions mentioned above

$$I_C(U) = \frac{4A\pi me}{h^3} R \int_{E_{\perp,\min}}^{E_m} dE_\perp \int_0^{E_{||,\max}} dE_{||}\, D(E_\perp)\left(f(E) - f(E+eU)\right). \qquad (2.48)$$

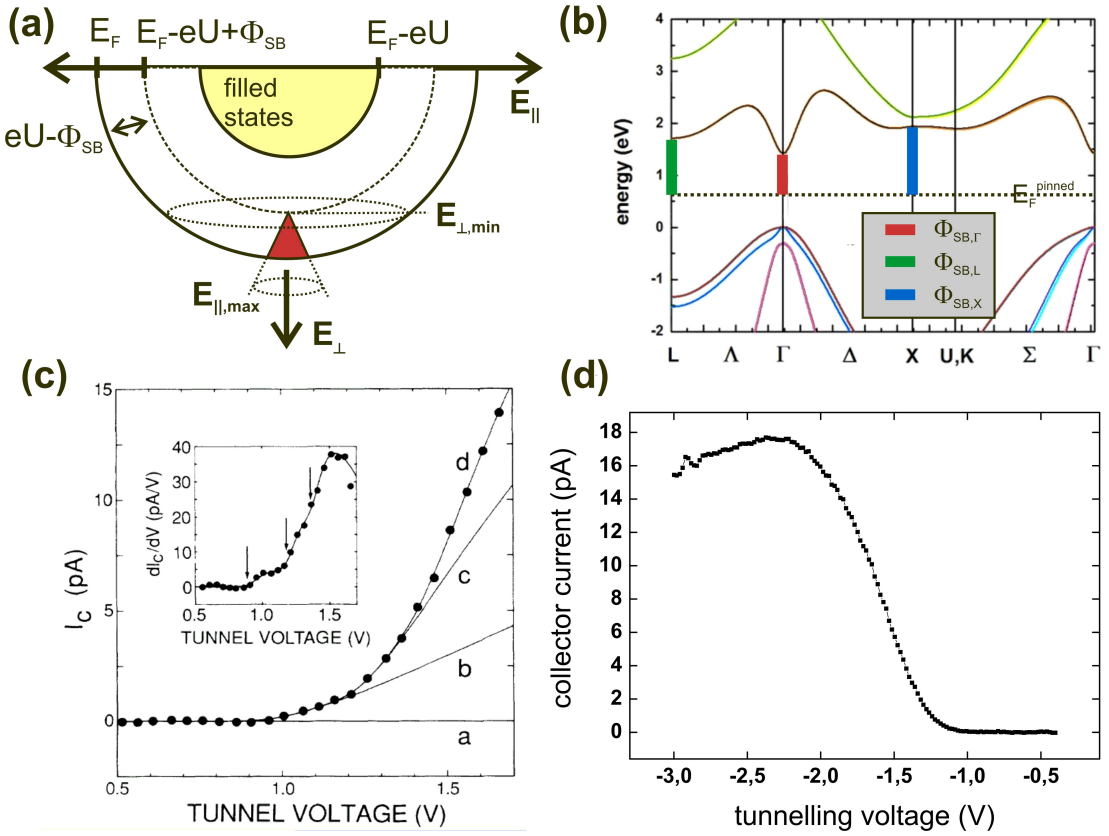

Figure 2.17: Only a small fraction (red) of the original tunneling phase space is available for ballistic hot electron transmission into the semiconductor as described by the Bell/Kaiser model [92] (a). Tight binding bandstructure calculation of GaAs (b) and $I_C U$-characteristic of Au/GaAs showing three independent I_C-contributions matching the energy of the Γ_{1c}, L_{1c} and X_{1c} conduction band valley of GaAs. Typical $I_C U$-spectrum recorded on $Fe_{34}Co_{66}$/Au/$Fe_{34}Co_{66}$ spin valves. (b) and (c) extracted from [93] and [92].

The normalization of this formula to I_T leads to the so-called Bell-Kaiser formula

$$\frac{I_C(U)}{I_T} = R\frac{\int_{E_{\perp,\min}}^{E_m} dE_\perp \int_0^{E_{||,\max}} dE_{||}\, D(E_\perp)\,(f(E)-f(E+eU))}{\int_0^{E_m} dE_\perp \int_0^{\infty} dE_{||}\, D(E_\perp)\,(f(E)-f(E+eU))} \tag{2.49}$$

with A being the emitter area. R is a constant including all scattering events in the base. Formula 2.49 can be simplified for the onset region ($eU \gtrsim \Phi_{SB}$) predicting a quadratic behavior $I_C \sim (eU-\Phi_{SB})^2$.

However, experimentally determined characteristics enforced an extension of this model, see Fig.2.17(b) and (c), and the incorporation of other conduction band minima with onsets at $E_F + \Phi_{SB,i}$. The simplest extension is to consider the total current as a sum

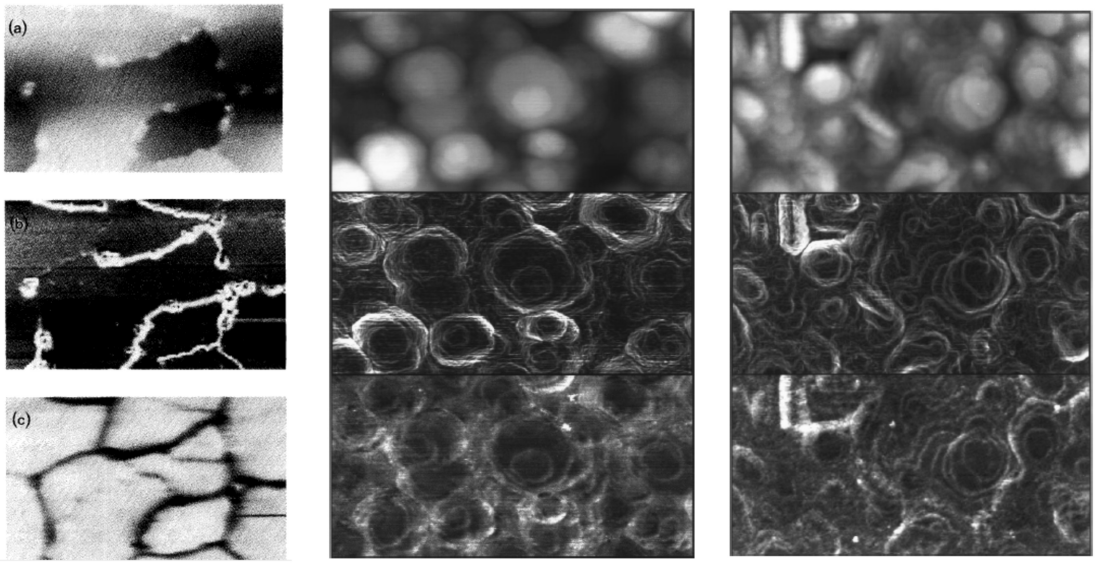

Figure 2.18: Topography, topography gradient and I_C as a function of tip position for Mg/GaP(110) (left), Au(111)/Si(100) (middle) and Au(111)/Si(111)(right). I_C is attenuated at atomic steps for Mg on GaP(110), while the opposite holds for Au(111)/Si(100) and Au(111)/Si(111). Graphs extracted from [96] and [45].

of the involved conduction band minima via

$$I_C \quad = \quad R \sum_i I_{C,i}(E_F + \Phi_{SB,i}). \tag{2.50}$$

Note that formula 2.49 takes only on-axis conduction band valleys into account and is limited due to its free electron character. The practical experience, however, shows that this formula fits the experimental spectra well in a quite large energy interval.

The authors of [94] complemented the approach used by Bell and Kaiser with quantum-mechanical transmission effects at the Schottky barrier. In addition they introduced integrand terms reflecting non perpendicular incidence on the interface and a simple energy dependent hot electron attenuation in the base [94, 95]. For the onset region of the I_CU-characteristic they found a $I_C \sim (eU - \Phi_{SB})^{5/2}$ behavior in contrast to the quadratic onset predicted by the Bell-Kaiser approach. Maxima in the I_CU-characteristic at larger tunneling voltages, see for instance Fig.2.17(d), are interpreted as a result of the enhanced scattering phase space. Spatial inhomogeneities of the I_CU-spectra are attributed to be a consequence of local surface gradients [95].

2.3.3.2 Microscopy

The high degree of ballistic transport in BEEM experiments can be nicely visualized by mapping I_C as function of tip position simultaneously with the topography. In the

last paragraphs we have addressed a forward focused electron momentum distribution combined with available on-axis states in the semiconductor. In this case, I_C is large on atomic terraces and attenuated at atomic steps or grain boundaries. The latter break the symmetry parallel to the interfaces and act therefore beyond the planar tunneling theory as a source of finite $k_{||}$ during tunneling facilitating non-perpendicular electron transport paths through the base, compare Fig.2.18. The situation for maps of I_C changes significantly when there are either gap areas in the base around $\overline{\Gamma}$ shielding on-axis states of the semiconductor, like for Au(111), or when there are no on-axis states available in the semiconducting collector, like for Si(111). These situations dictate that ballistic electrons have to travel away from the film normal [45] and that they are transmitted into the semiconducting collector via off-axis states only, which may require an additional source of $k_{||}$ in the base. Contrast in I_C-images is then reversed and I_C is large on atomic steps or grain boundaries as evidenced for Au(111)/Si(100) and Au(111)/Si(111), compare Fig.2.18.

2.3.3.3 Investigating spin dependent properties with BEEM

A standard exponential attenuation law of I_C is obtained with increasing base layer thickness d [39, 98, 99]. Scattering processes can therefore be studied by the variation of the thickness of layers involved in the base. The resulting scattering or attenuation length λ represents the thickness of the considered material to reduce I_C by a factor of e^{-1}. Strictly adhering to this definition the obtained attenuation length is greater or equal the mean free path Λ, because scattering does not automatically transfer hot electrons to undetectable states and contributions of secondary electrons cannot be ruled out.

The introduction of a spin valve into the base leads to a dependence of $I_C U$-characteristics on the magnetic configuration of the spin valve. In antiparallel magnetization configuration a majority spin electron in the first ferromagnetic layer is of minority spin character in the second layer and vice versa, while for parallel aligned magnetic moments the spin character remains conserved. Since minority spin hot electrons are generally more suppressed in transport than their counterpart, I_C is reduced in antiparallel magnetization configuration. The combination of the statements above yields for parallel (P) and antiparallel magnetization configuration (AP)

$$I_C^P/I_T \sim \exp\left(-\frac{d^{\mathrm{FM1}}}{\lambda_M^{\mathrm{FM1}}}\right)\exp\left(-\frac{d^{\mathrm{FM2}}}{\lambda_M^{\mathrm{FM2}}}\right)+\exp\left(-\frac{d^{\mathrm{FM1}}}{\lambda_m^{\mathrm{FM1}}}\right)\exp\left(-\frac{d^{\mathrm{FM2}}}{\lambda_m^{\mathrm{FM2}}}\right) \quad (2.51)$$

$$I_C^{AP}/I_T \sim \exp\left(-\frac{d^{\mathrm{FM1}}}{\lambda_M^{\mathrm{FM1}}}\right)\exp\left(-\frac{d^{\mathrm{FM2}}}{\lambda_m^{\mathrm{FM2}}}\right)+\exp\left(-\frac{d^{\mathrm{FM1}}}{\lambda_m^{\mathrm{FM1}}}\right)\exp\left(-\frac{d^{\mathrm{FM2}}}{\lambda_M^{\mathrm{FM2}}}\right) \quad (2.52)$$

with d and $\lambda_{M(m)}$ being the ferromagnetic layer thickness and the majority(minority)

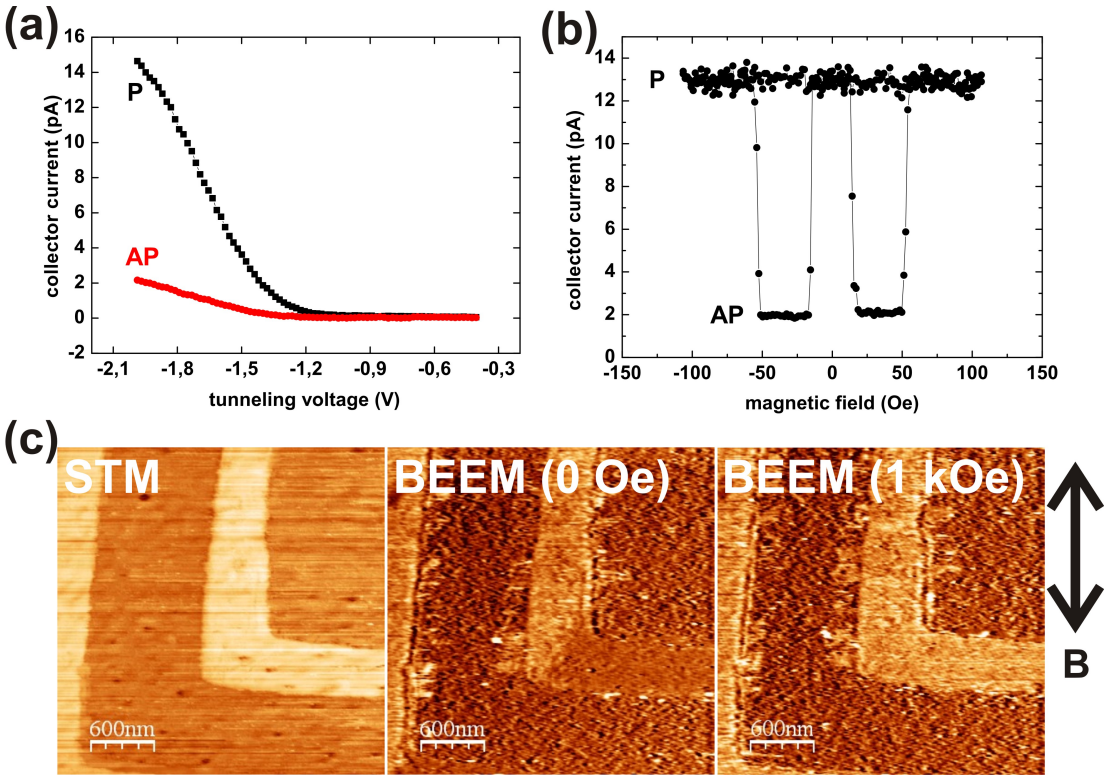

Figure 2.19: $I_C U$-characteristic measured at external fields of H=105 and 49 Oe in agreement with parallel and antiparallel magnetization alignment of a $Fe_{34}Co_{66}/Au/Fe_{34}Co_{66}$ spin valve (a) and corresponding hysteresis loop obtained with $U = -2\,V$ (b). Topography and I_C-images on zickzack patterned poly-crystalline $Au/Ni_{80}Fe_{20}$ films grown onto extended fcc Au/bcc $Fe_{34}Co_{66}$-layers on n-$GaAs_{67}P_{33}$. BEEM reveals the nucleation of an 90° domain wall in the $Ni_{80}Fe_{20}$-film [97].

spin scattering length, respectively. Apart from spectroscopy experiments the available spin contrast can be also employed to map magnetic domains in one of the ferromagnetic layers of the spin valve, see Fig.2.19.

2.4 Summary

In conclusion, a source of spin asymmetry in hot electron transport through ferromagnetic layers is provided by spin dependent group velocities and relaxation rates. The latter effect is supposed to stem from the spin dependent phase space for hot electron decay, which is sampled more or less effectively by electron-electron, electron-phonon and electron-magnon scattering. The utilization of a spin valve technique produces spin contrast manifested in collector currents depending on the magnetization configuration of the spin valve. The metal/semiconductor interface acts as an energy and momentum

filter separating almost ballistically transported hot electrons from those which are more thermalized. The combination of the spin valve technique with a metal/semiconductor contact allows therefore studying spin dependent hot electron transport.

3 Instrumentation and sample fabrication

The design of a Ballistic Electron Emission Microscope for investigating spin signals requires some careful specifications. Construction and implementation has to address a stable STM-operation with tunneling currents up to 100 nA in an external magnetic field. Additionally, a second terminal is needed for the detection of the small ballistic currents. The temperature of the sample holder has to be varied with a flow cryostat and, thus, the core of the instrumentation should be positioned within a UHV vacuum chamber. At the beginning of this chapter we discuss the electrical requirements for the detection of the collector and tunneling current. Thereafter, we address the mechanical setup and end by describing the sample preparation procedure.

3.1 Electrical Instrumentation

3.1.1 Detection of the collector current

Detecting low currents of the order of fA becomes essential when several metals with thicknesses comparable to their hot electron scattering length λ are introduced into the base as a consequence of the exponential thickness scaling of hot electron attenuation. On the other hand, we would also like to investigate thinner and hence more transmissive samples showing collector currents of the order of pA. A third condition addresses the measurement of I_C as function of tip position. Typically 256×256 data points per image have to be recorded in a reasonable time setting a lower limit for the amplifiers bandwidth. To accommodate these three requirements a current detector able to resolve currents between 0.1 pA up to 30 pA accompanied by an instrumentation bandwidth of the order of at least 10 Hz is needed. Such low current signals require the detector to be placed in the vicinity of the sample in order to avoid noise from other sources coupling into the electronic circuit.

The most powerful low current detector is a transimpedance amplifier (current to voltage converter) due to its low input resistance approaching zero and reflecting therefore a perfect current sink, see Fig.3.1(a) and [100]. During operation the input current becomes converted to an output voltage U_o depending on the feedback resistance R of the

amplifier via

$$U_o = I_C R. \tag{3.1}$$

These type of amplifiers are usually employed in STM for recording the tunneling current with resistors R being commonly larger than 100 MΩ. For BEEM we have to incorporate a second circuit for detecting I_C at an independent terminal. However for large feedback resistors R one has to respect the inherent resistor (Johnson) noise. It leads to an effective voltage noise $u_{R,\text{eff}}$ being proportional to the square root of R. In a current sensing experiment $u_{R,\text{eff}}$ shows up as a current noise $i_{R,\text{eff}}$ according to

$$\begin{aligned} u_{R,\text{eff}} &= \sqrt{4k_B T R \Delta\nu_C} \\ i_{R,\text{eff}} &= \sqrt{\frac{4k_B T \Delta\nu_C}{R}} \end{aligned} \tag{3.2}$$

with $\Delta\nu_C$ denoting the bandwidth of the measurement instrument. Current detection is therefore facilitated when large feedback resistors R are introduced. For instance, the thermal amplifier noise $i_{R,\text{eff}}$ at room temperature conditions equals 13, 4 and 1 fA/$\sqrt{\text{Hz}}$ for R=0.1, 1 and 10 GΩ, respectively. Let us express this result in terms of a signal to noise ratio (SNR), defined as

$$\text{SNR} = \frac{I_C}{i_{R,\text{eff}}}. \tag{3.3}$$

The detection of currents as low as 100 fA accompanied by an instrumentation bandwidth of $\Delta\nu_C$=100 Hz produces signal to noise ratios of 0.8, 2.5 and 10 for R=0.1, 1 and 10 GΩ, respectively, see also Fig.3.1(b). Hence, a feedback resistor of R=0.1 GΩ is not sufficient to dominate its own resistor noise in the output signal U_o for the desired setup. Another problem is that high gain transimpedance amplifiers tend to unstable operation conditions. In order to avoid such gain peaking effects, a small capacitor is commonly connected in parallel to the feedback resistor R [101]. With no capacitor connected the capacitance C is governed by stray capacitances, which are of order some pF and present in all circuits. However, a nonzero C and R limits the amplifiers bandwidth $\Delta\nu_C$ according to the low pass formula

$$\Delta\nu_C = \frac{1}{2\pi RC}. \tag{3.4}$$

To assure electrically stable operating conditions, we choose for the capacitor C a value well above any stray capacitances of $C = 10$ pF. In order to keep the RC-product and thus the time constant as low as possible, a resistor with R=1 GΩ is employed in the feedback circuit. However, the determination of the corresponding transfer function[1] yields an instrumentation bandwidth being already too low and less than 10 Hz, only.

[1]The frequency dependence of the Output/Input=$U_o/I_C R$ ratio

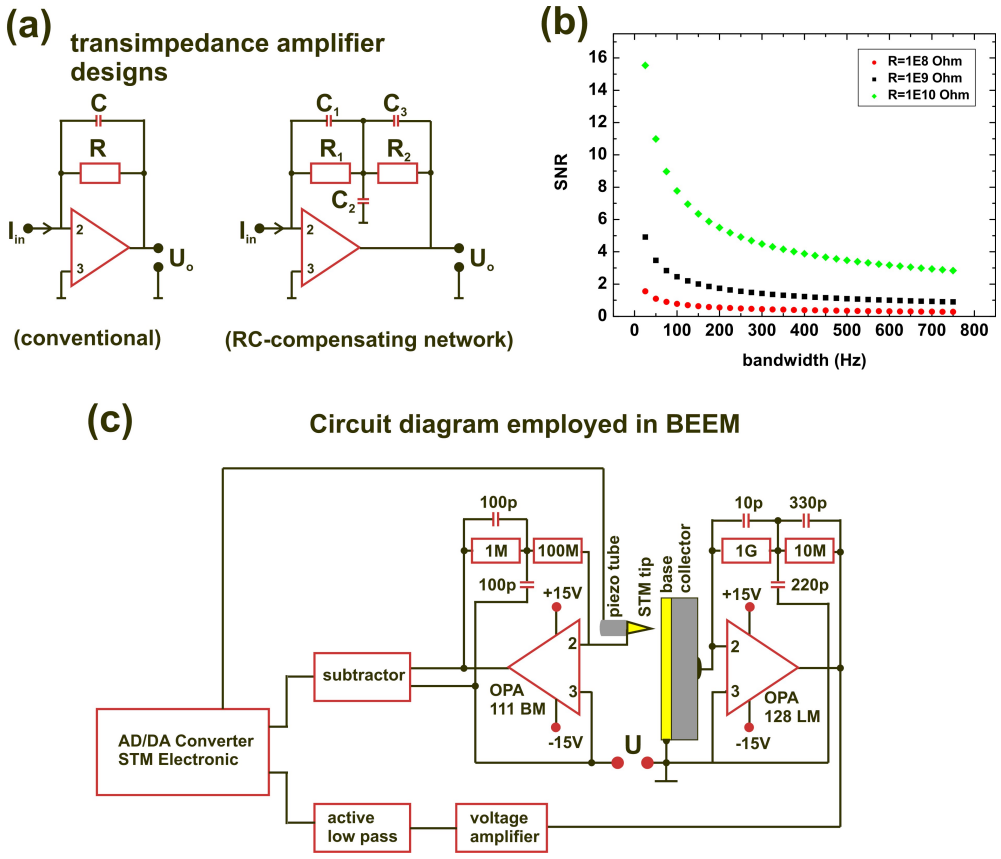

Figure 3.1: Transimpedance amplifier: conventional and RC-compensating network design (a). Calculated signal to noise ratio using formula 3.3 with I_C=100 fA (b). Electrical instrumentation employed in this work (c). The sample is sandwiched between two transimpedance amplifiers detecting I_T and I_C.

With an alternate design of a transimpedance amplifier circuit, see Fig.3.1(a) we increase the bandwidth beyond the limitations of the time constant RC at the cost of signal to noise ratio. The introduction of a high pass R_2C_2 into the feedback of the operational amplifier is used to compensate the low pass effect of R_1C_1, while the second low pass provided by R_2C_3 sets the overall bandwidth of the current to voltage converter [102, 103]. We determine the optimum values of C_2, C_3 and R_2 by varying them carefully in order to linearize the transfer function up to larger frequencies and to avoid overshoot effects, see Fig.3.2. In a second step the output voltage U_o becomes amplified by a factor of 100 and roughly corrected for any electrical offset by a difference amplifier. Shiftable notch filters for 100 and 50 Hz line noise are additionally incorporated but mostly switched off during the measurement. Before feeding the I_C signal into an analog-digital(AD) converter the remaining high frequency noise is cut off by a third order active low pass (Butterworth circuit) with variable threshold frequencies of f_g=5,

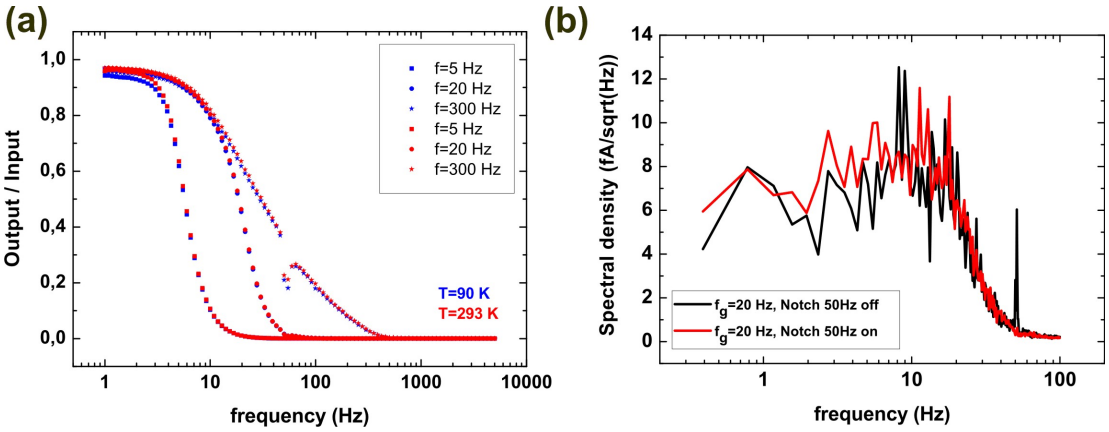

Figure 3.2: Transfer function of the circuit processing I_C with the sample holder at temperatures of 300 and 90 K, respectively (a). Spectral density of the circuit processing the collector current signal (b) with and without 50 Hz notch filter activation. The active low pass is set to a threshold frequency of 20 Hz.

20 and 300 Hz. The lower cut-off frequencies are designated for I_CU-spectroscopy, which requires very low noise levels, while the cut-off frequency of 300 Hz can be employed in BEEM-imaging, where a lot of data points have to be measured within a reasonable time. Fig.3.2(a) shows the resulting transfer function of the complete circuit processing I_C. The steep decay of the Output/Input ratio with increasing frequency is governed by the cutoff of the butterworth filter and the dip at $f = 50$ Hz is due to an active notch filter. The graph for f_g=300 Hz exhibits a -3 dB-bandwidth of about 17 Hz accompanied by a smoother decay with frequency, which stems from the low pass effect of the transimpedance amplifier. It turned out that this is the best compromise between SNR and instrumentation bandwidth.

Furthermore, the spectral density of Fig.3.2(b) demonstrates a low white noise level superimposed to a frequency dependent behavior above 20 Hz, which is just impressed by the active low pass set to this cut-off frequency.

Another crucial aspect of the circuit is that the electrical load, which separates the inverting input of the collector current transimpedance amplifier from ground, is given by the resistance R_s of the Schottky diode, see Fig.3.1(c). R_s can be experimentally extracted from the first derivative of the Schottky diode IU-characteristic at vanishing base/collector bias voltage $U_{BC} = 0$. We can also estimate this value with the thermionic theory model of Schottky diodes according to

$$R_s = \frac{h^3}{4\pi m^* e^2 k_B T A} \exp\left(\frac{\Phi_{SB}}{k_B T}\right) \tag{3.5}$$

with A being the diode area [36]. R_s can be calculated to 4.9 MΩ (642 MΩ) for Fe/GaAs (Fe/$GaAs_{67}P_{33}$) by assuming $A = 1\,\mathrm{mm}^2$, $m^* = 0.069m(0.089m)$, $\Phi_{SB} = 0.7(1)$ eV and

$T = 300\,\mathrm{K}$. It turned out that the offset of the transimpedance amplifier is critically sensitive to external sources of voltage noise when R_s is small (not well above $1\,\mathrm{M\Omega}$ [36]). The offset even responds to motion of personal in the laboratory, which strongly impedes the performance of thorough measurements. The same effect occurs when the sample is replaced by a one meter long unshielded floating cable, which acts as an antenna for electrical field changes. Such transimpedance amplifiers with a relative low electrical load between the current source and the inverting input are elsewhere applied as all-electrical motion detectors [104]. Since the sample resistance in BEEM should not fall below this threshold value for thorough operation conditions, please note that R_s can be increased by using smaller diode areas A, larger Schottky barriers Φ_{SB} or by reducing the temperature as visible in equation 3.5.

Finally, we have to take care of any temperature dependence of the electrical detection system upon cooling the sample holder, since the applied high ohmic feedback resistors are ELTEC Model thin film semiconductor resistors. They are known to multiply its own resistance when being cooled to liquid nitrogen temperature. We address this question by measuring the transfer function with the sample holder cooled to 90 K. No significant changes compared to room temperature operation is observed, see Fig.3.2(a).

Note that the sample structure as a Schottky diode creates photocurrents in the µA-range when being exposed to sources of light, which drives the output voltage of the transimpedance amplifier to saturation. The detection of the much lower collector currents requires this STM-like experiment to be performed in darkness with blacked out window flanges and with hot cathode pressure gauges switched off.

3.1.2 Detection of the tunneling current

Demands on the STM-amplifier feedback resistance are governed by the current range (up to 100 nA) and bandwidth considerations rather than by noise requirements. The instrumentation bandwidth $\Delta\nu_T$ should be of order of $10^2..10^3\,\mathrm{Hz}$ to assure a sufficiently fast response of the feedback circuit during scanning in constant current mode. We utilize $R = 100\,\mathrm{M\Omega}$ with no additional capacitance C connected in parallel to R. The transfer function is once more optimized by the variation of C_2, C_3 and R_2. The final circuit exhibits a -3 dB bandwidth at 1.5 kHz, see Fig.3.3(a) and is placed in situ, as well. The noninverting input is connected to the tunneling voltage for biasing the STM-tip, i.e. I_T is measured with respect to U rather than to ground. In order to accommodate the requirements of the STM feedback electronic an additional analog subtractor is introduced to subtract U from the output voltage.

For tunneling currents in the nA-regime current noise appearing in I_T is governed by flicker noise rather than by shot or resistor noise. Flicker noise $i_{f,\mathrm{eff}}$ can be phenomeno-

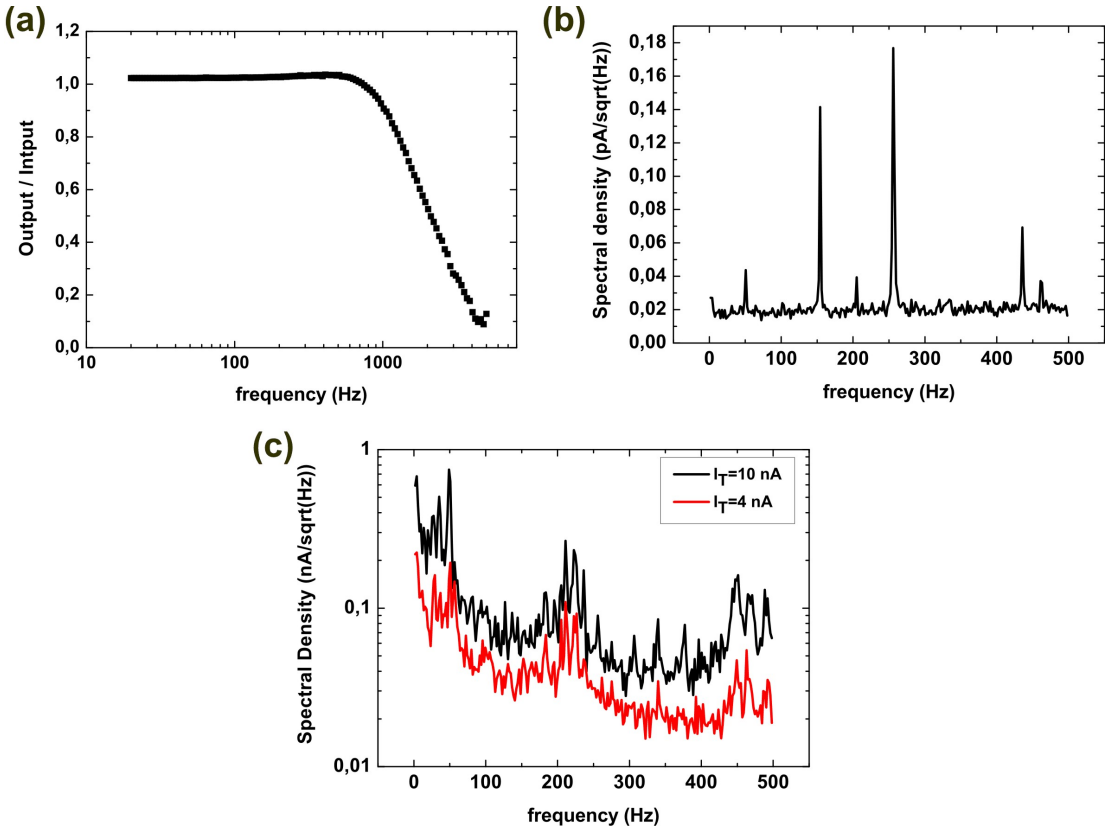

Figure 3.3: Characterization of the electronic circuit processing I_T: Transfer function showing a -3 dB bandwidth at a frequency of 1.5 kHz (a). Tunneling current spectral density without (b) and with tunneling contact (c). The latter one is recorded in constant height mode at an average tunneling current of $I_T = 4\,\mathrm{nA}$ and 10 nA using a $Au/Fe_{34}Co_{66}/GaAs_{67}P_{33}$-sample.

logically treated by [105]

$$i_{f,\mathrm{eff}} = \sqrt{\frac{\alpha I_T^2}{\nu}\Delta\nu_T} \tag{3.6}$$

with $\Delta\nu_T$ being the instrumentation bandwidth and α a constant of order of $10^{-3}-10^{-6}$ for STM operation [105]. We can visualize the tunneling current noise by obtaining the spectral density in constant height mode, where obscuring artefacts of the STM feedback are avoided, see Fig.3.3(b) and (c). The current noise amplitude of I_T is, like the hot electrons, attenuated within and transmitted through the base layers and finally mapped onto I_C.

3.1.3 Other parameters of the setup

Within this work the STM-feedback controlling the tunneling distance acts on absolute deviations from the setpoint of I_T rather than on the logarithm of it as commonly employed in STM-experiments. It turned out that a constant current source is more likely obeyed in this way.

Attempts to establish a low frequency lock-in instrumentation with a modulated bias voltage and a demodulated collector current signal were not successful. This approach was mostly hampered by the strong capacitive pickup in the I_C-circuit, compare also [36].

3.2 Mechanical Instrumentation

Technical demands concerning the mechanical setup are mostly governed by a stable STM operation. Any instability of the tunneling gap may create additional noise or overshoot effects in I_T, which also deteriorate the measurement conditions for I_C. To meet this requirement, we apply a two stage mechanical damping system combined with a stiff STM-head design. The UHV-chamber rests on a pneumatically controlled oil suspension system, while the STM-head itself is decoupled by an in-situ vibrational isolation stage, whose special design can be regarded as a miniaturized version of the damping system used in [106].

The magnetic field environment enforces the utilization of materials with low intrinsic magnetic moments for the sample holder. Due to the intended temperature dependent studies, we further benefit from materials with low temperature expansion coefficients. Against the background of mechanical processibility the last two conditions are best met by Titanium, which we use for building the STM-head, see Fig.3.4. This exhibits the shape of a cuboid and contains a 3D sawtooth piezo-actuator for rough positioning of the sample and a four quadrant piezo tube scanner for STM-operation. The holder of the STM-tip is directly glued onto the piezo tube. The vicinity between the large voltages applied to the piezo tube and the current sensing capability of the STM-circuit facilitates cross talk effects, which we suppress by shielding the piezo tube with an aluminum based housing.

The sample holder is made up of OFHC-copper[1], which is known to have one of the best thermal conductivities at all. It rests on 4 glass pearls and is exclusively screwed to a ceramic disc mounted on top of the sawtooth piezo-actuator to assure an effective thermal and electrical isolation combined with good mechanical stability. To avoid additional mechanical vibrations the flow cryostat is connected to the sample holder with

[1] OFHC: oxygen-free high thermal conductivity, a copper purity grade insuring a copper content of at least 99.95 %.

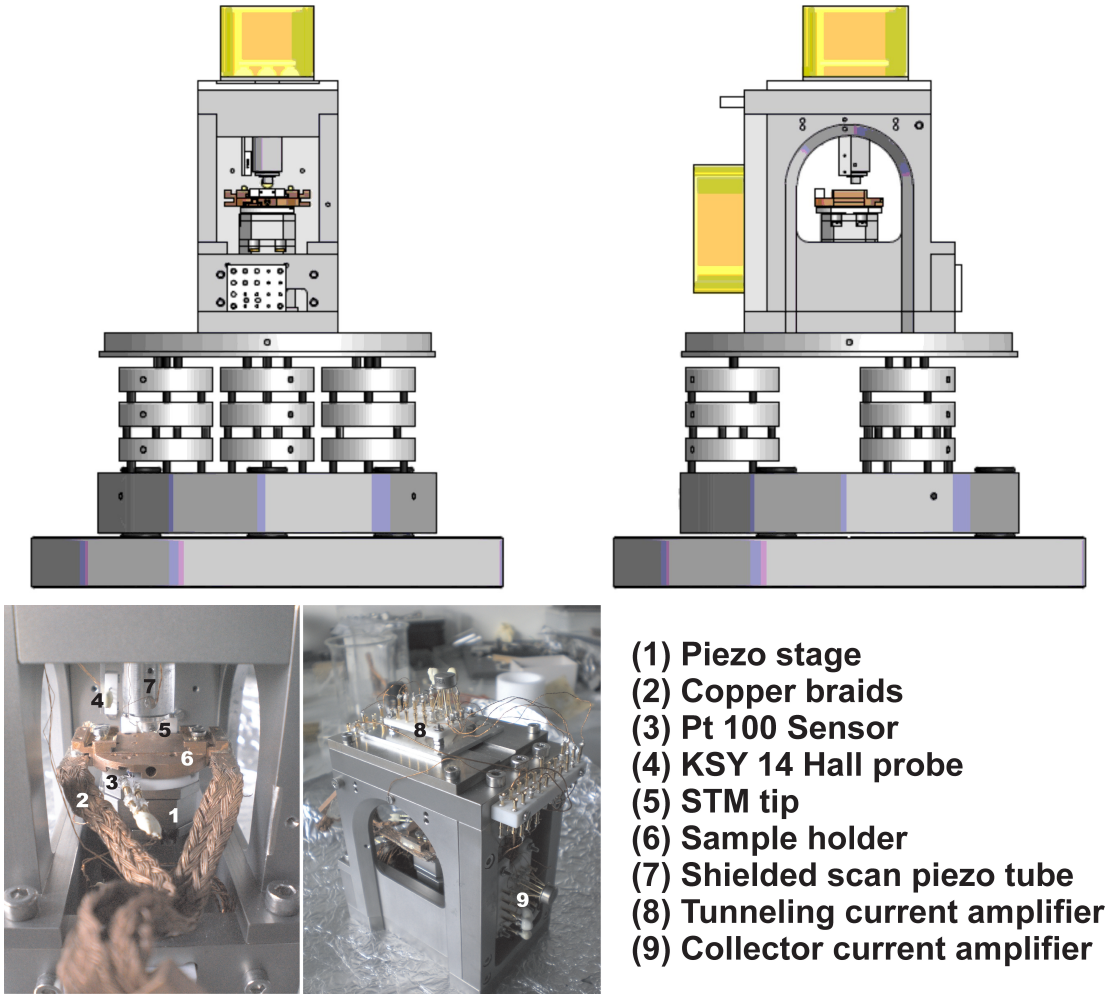

Figure 3.4: Construction plan of the STM/BEEM head (top) and its implementation with the main sensors and actuators (bottom).

OFHC-copper braids and air-cooled iron core coils are used instead of water cooled ones. Magnetic fields up to 1.5 kOe can be generated so far, as measured by an implemented in-situ Hall probe near the sample position. The temperature of the sample holder and the cryostat is recorded within a four-point geometry using a Pt100 resistor and a 29 Ω FeRh-resistor, respectively.

During the assembly of the setup it turned out that the electrical connection of the flow cryostat to the sample holder induces non tolerable electrical noise in the transimpedance amplifier circuit processing the low ballistic currents. Despite lots of efforts were made to eliminate this problem, acceptable working conditions were restored only by electrically isolating the cooling stage with sapphire plates. This, however, strongly increases the thermal resistivity between the sample holder and the cryostat

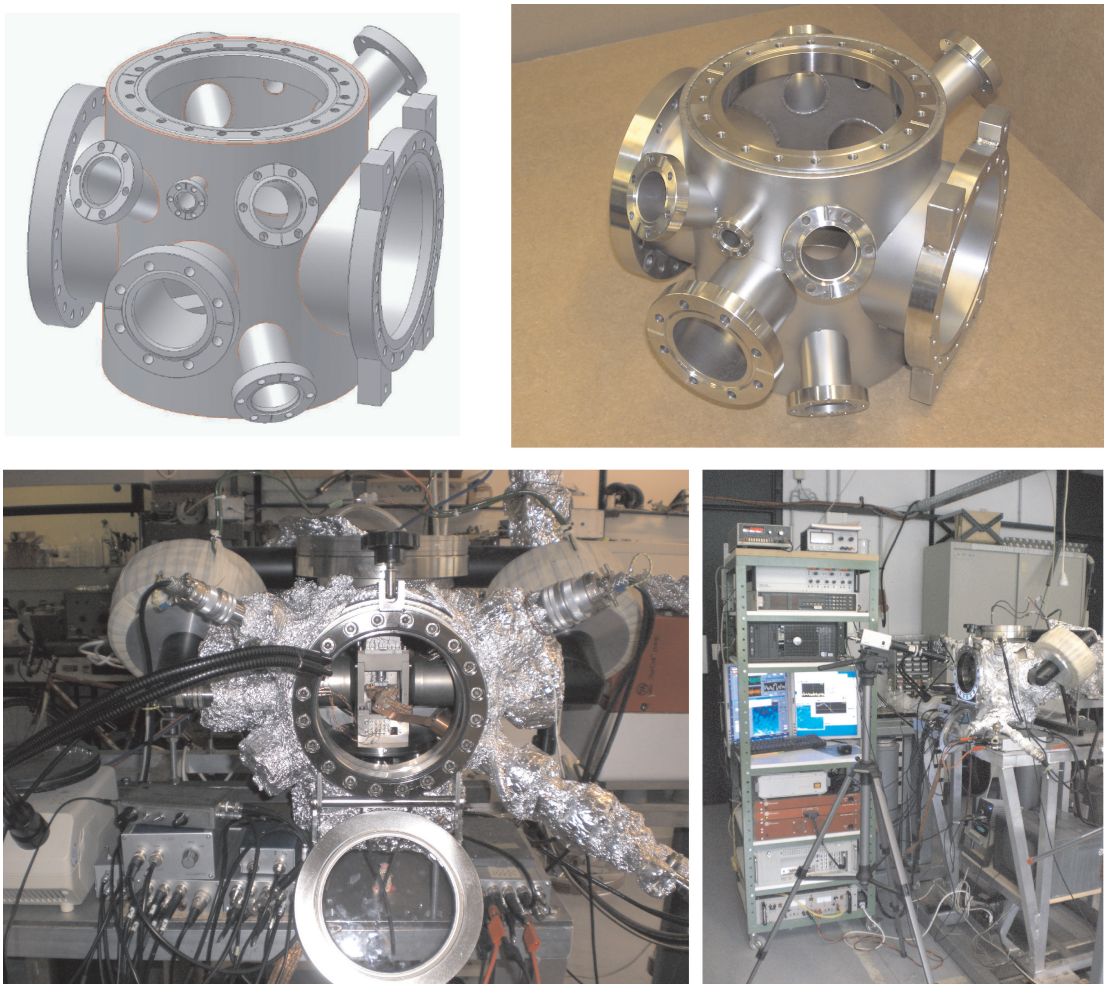

Figure 3.5: Construction and implementation of the vacuum chamber designated to include the BEEM setup (top) and an overview of the complete assembled setup (bottom).

and, as a consequence, reduces the available temperature range. The lowest temperatures achieved on the sample holder so far are therefore 85 K using LHe and 130 K using LN_2, while the cryostat itself is cooled down to 7 K and 69 K, respectively.

The CAD-construction of the vacuum chamber and its production by the local mechanical workshop are shown in Fig.3.5. The chamber has been leak tested using Helium and found to be tight within the sensitivity of the employed leak tester. The overall setup is intended to operate without any loadlock and is vented for sample exchange. Apart from one Viton sealed flange designated for a fast access to the chamber copper gaskets are used solely. The chamber is pumped by an ion-getter, Titan sublimation and a turbo pump backed by a two stage roughing pump (membrane and turbo-drag pump). During BEEM and STM operation all mechanically working pumps are switched off and a pressure in the range of $5 \cdot 10^{-10} - 2 \cdot 10^{-9}$ mbar is maintained by the ion-getter and sublimation pump. An image of the complete setup can be seen in Fig.3.5.

3.3 Sample preparation

As substrate material the Tellurium doped ternary semiconductor $GaAs_{67}P_{33}$ is employed in this work. The wafers are heteroepitaxial bilayer stacks consisting of a 7 µm thick n-$GaAs_{67}P_{33}$(100) layer with a dopant concentration of $N_d = 5 \cdot 10^{16}$ cm^{-3} grown onto a n-GaAs(100) wafer with $N_d = 10^{18}$cm^{-3}. With reference to the Mott density of GaAs, which equals $2.8 \cdot 10^{16}$ cm^{-3}, a doping density of $N_d = 5 \cdot 10^{16}$ cm^{-3} in $GaAs_{67}P_{33}$ can be interpreted as a slightly degenerate doping level forcing E_F above the conduction band edge in the bulk material. An investigation of the surface morphology of this wafer highlights a cross-hatch pattern, which arises from strain induced misfit dislocations [107–109], see Fig.3.6(a,b). Surface characterization using atomic force microscopy on the unprepared semiconductor surface reveals a striped profile with peak to peak corrugations of 4 nm on lateral scales of hundreds of nanometers, compare Fig.3.6(c). Due to the utilization of $GaAs_{67}P_{33}$ instead of GaAs we benefit from the larger energy gap of $E_g = 1.81$ eV and, thus, from the larger Schottky barrier height Φ_{SB} and sample resistance, as well. Leakage currents across the metal/semiconductor interface are more effectively suppressed and room temperature experiments are facilitated thereby. The similarity of $GaAs_{67}P_{33}$ and GaAs is also reflected in very similar lattice constants of $a = 0.562$ nm [98] and $a = 0.565$ nm, respectively. This, in turn, provides similar growth conditions for overlayers. GaAs(100)-substrates are known to permit epitaxial growth of bcc Fe- and bcc Fe_xCo_{1-x}-films with $x > 0.2$ on top [110]. With regard to spin dependent ballistic hot electron transport studies these metals are particularly interesting due to their very dissimilar phase space for hot electron decay and due to their single crystalline structure, which minimizes ballistic current attenuation at grain boundaries. Furthermore, the evaporation process can be continued to build up completely epitaxial multilayer stacks, like spin valves. For this purpose, thin epitaxial films of gold or silver can be introduced as spacer layers between the bcc Fe or bcc $Fe_{34}Co_{66}$ films. By this means layer stacks with the configuration: GaAs(100)<010> || bcc Fe or $Fe_{34}Co_{66}$(100)<010> || fcc Au or Ag(100)<011> || bcc Fe or $Fe_{34}Co_{66}$(100)<010> can be achieved. The stoichiometry of $GaAs_{67}P_{33}$ manifests itself in low lying conduction band edges L_{1c}, X_{1c} and X_{3c}, see Fig.3.7. The former two are energetically located at $\Gamma_{1c} + 0.16$ eV, while the edge of X_{3c} is found at $\Gamma_{1c} + 0.41$ eV, respectively. Due to the (100)-surface orientation conduction band states around the X-point project onto $\overline{\Gamma}$ so that these are accessible for hot electrons as on-axis states with $k_{||} \approx 0$. Compared to GaAs(100)-substrates with energetically higher conduction band edges we expect an improved hot electron transmission across the metal/semiconductor interface with increasing electron energy [44].

As mentioned above, ballistic currents may be suppressed in the base at metal interfaces due to mismatched energy surfaces. It is therefore desirable to introduce as few

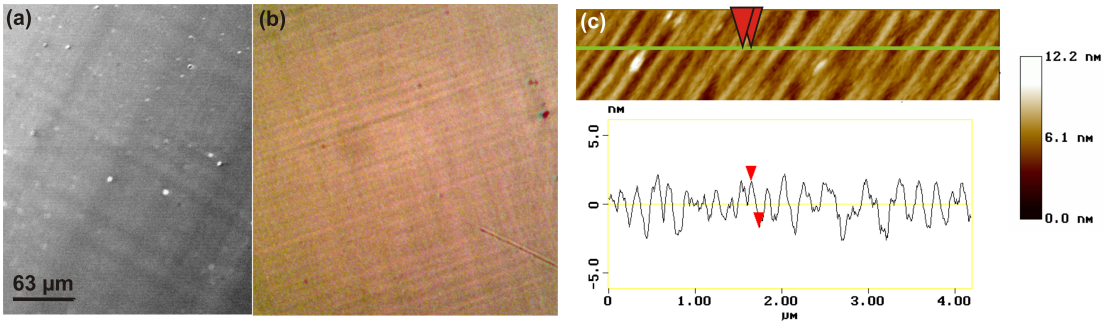

Figure 3.6: Surface morphology of $GaAs_{67}P_{33}(100)$: Scanning electron (a) and optical (b) microscopy reveals a cross hatch patterned surface. Atomic force microscopy reveals a striped corrugation on the nanoscale (c).

different materials as possible into the base, since the repeated occurrence of the same interface structure leads to no further attenuation of I_C in a pure ballistic transport process, compare [111]. From this point of view the most promising sample systems are $Au/Fe_{34}Co_{66}/Au/Fe_{34}Co_{66}$ and Au/Fe/Au/Fe-stacks. Note that the ex-situ sample transfer from the evaporation chamber to the BEEM-setup imposes the selection of Au rather than Ag as cap material due to its chemical passivity. The center of investigation of this thesis is mainly given by $Fe_{34}Co_{66}/Au/Fe_{34}Co_{66}$ spin valves, whose fabrication and crystallinity we highlight in the following.

Prior to the metal deposition the semiconductor surface is cleaned for about 90 minutes by sputtering with 1 keV Ar ions while simultaneously annealing at 840 K in UHV-conditions. This receipt is based on Auger-electron spectroscopy determining the O_2 and carbon contamination on the $GaAs_{67}P_{33}$-surface. It turned out, that oxides are significantly reduced when the substrate is annealed for 1/2 hour at temperatures of at least 820 K. On the contrary, no oxide reduction is observed for annealing at 770 K. In addition, sputtering for 45 min completely suppresses the carbon contamination on the surface. The remaining time is spent on scanning the sample with respect to the ion beam to assure a homogenous cleaning on areas of 1 cm^2. An ohmic back-contact to the semiconductor is created by means of InGa-eutectoid. A small droplet of this fluid metal is deposited onto the backside of the wafer and alloyed with it during the annealing procedure. The metallic spin valve stack is evaporated with growth rates of about one monolayer/minute at a pressure of $2 \cdot 10^{-10}$ mbar by molecular beam epitaxy (MBE) at room temperature and finally capped with a gold protection layer for chemical passivation. Evidence for the fully epitaxial growth of $Au/Fe_{34}Co_{66}/Au/Fe_{34}Co_{66}$ stacks is given by Reflection of High Energy Electron Diffraction (RHEED) during growth and by cross-sectional Transmission Electron Microscopy (TEM), see Fig.3.7.

Due to the single crystalline structure of the ferromagnetic films we also benefit from

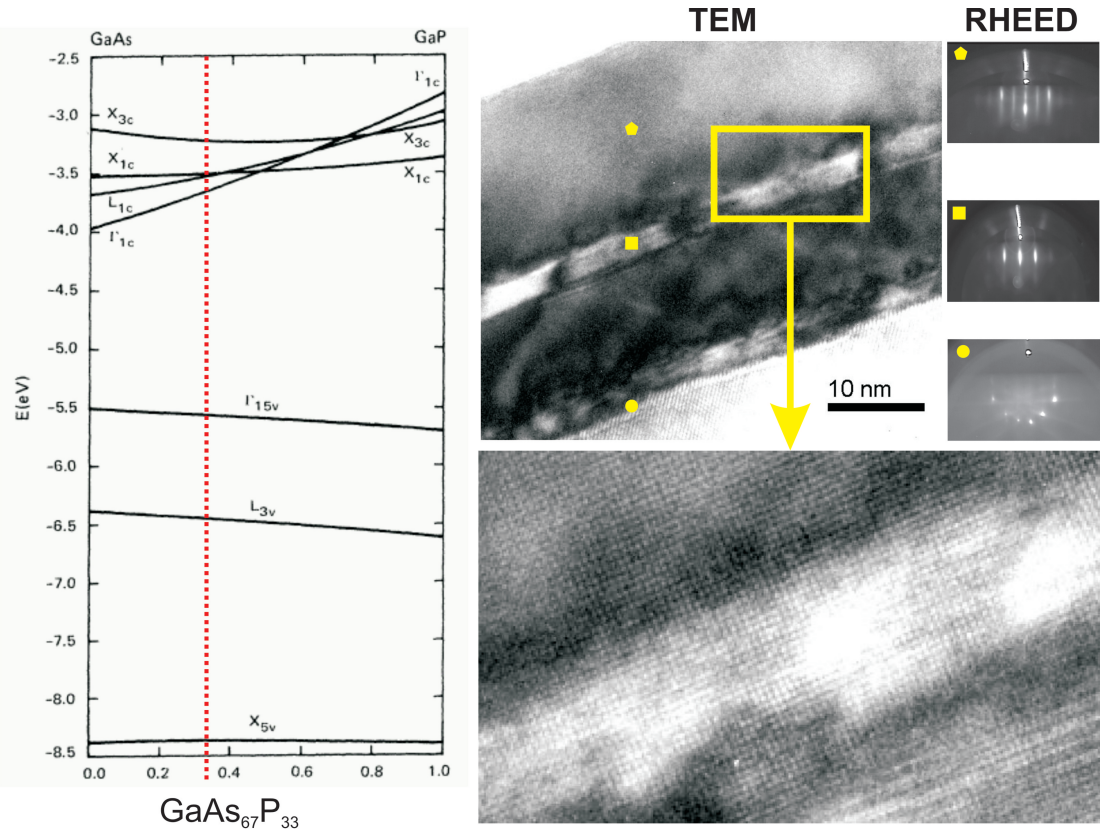

Figure 3.7: Conduction band profile of $GaAs_{67}P_{33}(100)$ (left) and crystallinity of $Fe_{34}Co_{66}/Au/Fe_{34}Co_{66}$ spin valves grown onto $GaAs_{67}P_{33}(100)$. TEM and RHEED during layer deposition clearly demonstrate the single crystalline growth (right). Graphs extracted from [86, 98].

magnetic crystalline anisotropies, which lead to parallel aligned magnetic easy axes of the two $Fe_{34}Co_{66}$-layers. In this way parallel and antiparallel magnetization configuration are exclusively accessible during the magnetization reversal yielding maximum spin contrast.

After the metallization process the sample is cut into pieces with diode areas of about 2x2 mm^2 and any hot electron transport experiments are carried out on the extended base layers. In the following, we label the $Fe_{34}Co_{66}$-layer deposited directly onto the semiconductor as FM1 and the second $Fe_{34}Co_{66}$-layer as FM2.

4 Results

In this chapter all experimental results are shown and discussed with regard to the electron transport and relaxation theory described in the last chapters. At the beginning the diode characteristics of the metallized semiconductor samples are highlighted accompanied by the determination of the sample resistance. We discuss then general features of the obtained hot electron characteristics and proceed to study the magnetic response of $Fe_{34}Co_{66}$/Au/$Fe_{34}Co_{66}$ spin valve samples. Thereafter, the center of our investigation is given by the hot electron attenuation lengths of bcc $Fe_{34}Co_{66}$ and fcc Au, which are are determined by a thickness dependent study. The question, whether spin asymmetry in hot electron transport is governed by interface or by bulk properties of the ferromagnetic layers, is cleared up and the importance of the crystalline structure combined with the influence of the substrate material is analyzed. A model based on ab-initio bandstructure calculations allows us to understand the energy characteristics and the spin dependence of the attenuation lengths. We conclude this chapter by investigating the temperature dependence in $Fe_{34}Co_{66}$/Au/$Fe_{34}Co_{66}$ and $Fe_{34}Co_{66}$/Au/Fe trilayers to check for differences of hot electron transport between bcc Fe and bcc $Fe_{34}Co_{66}$.

4.1 Characterization of the base/collector contact

Due to the instrumentation sensitivity on the sample resistance and on the ohmic back contact the metallized semiconductors are first tested for their Schottky diode characteristics. Many sample series contain defective samples with a reduced R_s as well as operating sample pieces. For the desired hot electron measurements the highly resistive samples need to be selected. Reasons for a degraded quality may be found in inter-diffusion processes of the metal atoms into the semiconductor, which lead to lowered and thinned Schottky barrier shapes strengthening the influence of leakage currents.

It turned out that a fast and reliable examination of R_s can be performed by measuring the resistance for forward and reverse biased diodes using a commercial Ohm-meter. This test even succeeds under illuminated conditions. Semiconductor dopant concentrations of order $N_D = 10^{16}\,\mathrm{cm}^{-3}$ combined with sufficiently large Schottky barrier heights

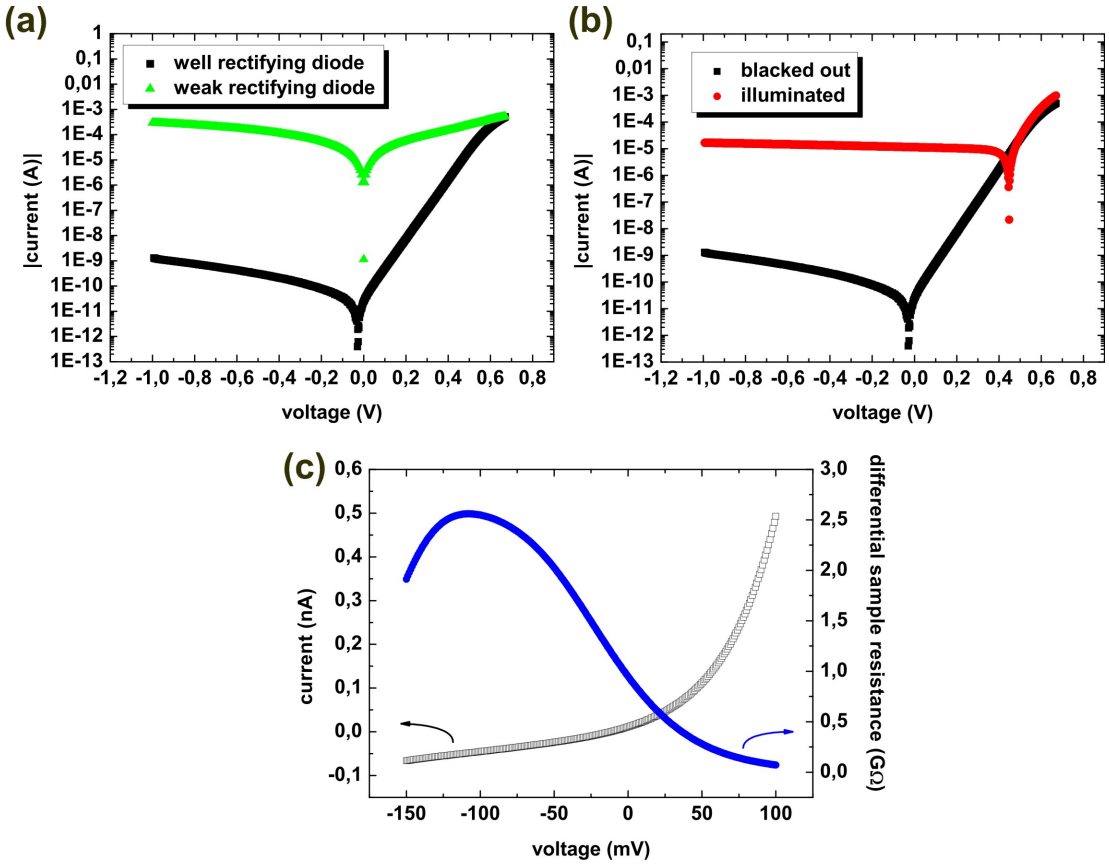

Figure 4.1: Current voltage characteristic of the base/collector contact of weak and well rectifying diodes in blacked out conditions (a). By illuminating the latter kind of Schottky diodes the impact of photocurrents is clearly visible (b), while in blacked out conditions these samples exhibit large resistances at $U_{BC} = 0$ (c). The graphs are recorded at room temperature using samples with an effective diode area of approximately $4\,\mathrm{mm}^2$.

give rise to effective rectifying properties and therefore to photocurrents as well. This diode behavior scales tightly with the quality of the metal/semiconductor interface and easily deteriorates when N_D is accidentally increased or the effective barrier height reduced. In doing so, broken diodes with a reduced R_s exhibit a more symmetric (more ohmic) current voltage characteristic than well rectifying diodes do, compare Fig.4.1(a). In the same manner, resistance readings of multimeters are more or less different when biasing the sample in forward and reverse geometry.

Beyond this fast test a more thorough characterization of the base/collector Schottky contact quality is the investigation of the current-voltage-characteristic, which we obtain by using a two point geometry, see Fig.4.1. Once defective samples are sorted out, we utilize the remaining operational ones to determine the impact of photocurrents and to

reveal the relevant sample resistance around $U_{BC} = 0$. When the Schottky diodes are illuminated using a commercial halogen light, photocurrents of order of µA are created demonstrating the need to perform BEEM in blacked out conditions, see Fig.4.1(b). The resulting sample resistance, as determined by the first derivative of the current-voltage-characteristic, exhibits values in the large M Ω- and low G Ω-regime and meets therefore the requirements of the instrumentation, see last chapter and Fig.4.1(c).

4.2 Features of hot electron characteristics

Once spin valve samples with well rectifying properties are identified, they are inserted into the BEEM-setup and approached towards the STM-tip until the desired setpoint of the tunneling current is reached. When we record the collector current at fixed I_T and sweep the tunneling voltage U, the resulting $I_C U$-spectrum demonstrates the typical onset of I_C at voltages equivalent to Φ_{SB}, see Fig.4.2(a). Toggling between parallel and antiparallel magnetization configuration of the spin valve via an external magnetic field B enforces I_C to interchange between large and low levels reflecting the spin dependence of hot electron transport[1].

By checking for the response of I_C upon variations of the tunneling current while keeping the tunneling voltage fixed, i.e. by reducing the tunneling distance, a linear rise of I_C is commonly obtained for emitter currents of $I_T < 30\,\text{nA}$, see Fig4.2(b). As in a conventional transistor design the linear $I_C I_T$-characteristic demonstrates that the collector current is a fraction of the emitter current. The linear behavior is observed for both magnetization configurations, however, with a distinct slope reflecting once more the spin dependence of hot electron transmission through the base. It turned out that for setpoints beyond 30 nA deviations from the linear dependence become likely leading to suppressed values of I_C. Moreover, $I_C I_T$-characteristics are rather irreproducible for all bias voltages when I_T exceeds 30 nA. Only rarely linear dependencies ranging up to $I_T = 100\,\text{nA}$ can be observed. We cannot find an unambiguous interpretation therefor yet. It may be caused by hot electron scattering with other injected hot or not completely relaxed electrons (space charging), since base transfer times are in the fs-regime but relaxation and transport of relaxed electrons lasts longer. Another reason may lie in the variation of the angular distribution of the injected hot electrons being more spread at smaller tunneling distances (i.e. at larger I_T), see Fig.2.4. But we can also not exclude instrumentation artefacts. In order to avoid drawbacks for the subsequent interpretation of the results, the majority of the following experiments is carried out with tunneling currents less then 30 nA.

[1] This behavior justifies the name Magnetic Tunnel Transistor, whose on- and off-state is controlled by the magnetization configuration of a spin valve.

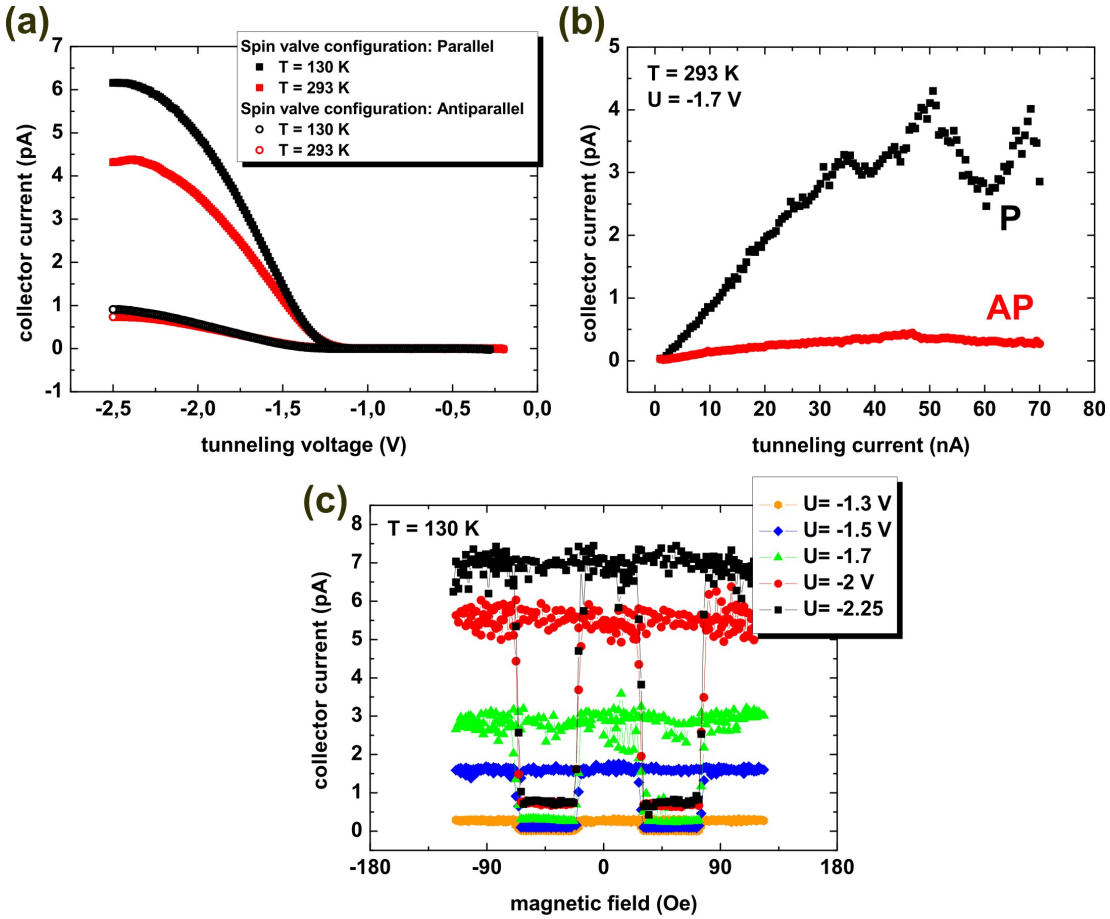

Figure 4.2: $I_C U$- (a), $I_C I_T$- (b) and $I_C B$-characteristic (c) of an 18.7 nm Au/ 2.9 nm $Fe_{34}Co_{66}$/ 10.8 nm Au/ 5 nm $Fe_{34}Co_{66}$ spin valve stack grown onto n-$GaAs_{67}P_{33}$. All three curves reflect the same spin contrast. Data of (a) and (c) is obtained with I_T = 20 nA.

Hysteresis loops ($I_C B$-characteristics) are obtained by recording I_C and by sweeping an external magnetic field B while keeping U and I_T constant. They depict the relative angle between the two magnetization vectors of the spin valve at each field value. The difference in I_C, which appears in $I_C U$-characteristic when toggling between the two collinear magnetization configurations, is also visible in the hysteresis loops, compare Fig.4.2(a) to (c).

Note that $I_C U$-characteristics, as shown in Fig.4.2(a), represent the average of several hundred up to some thousands single characteristics randomly obtained over the sample surface and that hysteresis loops, like in Fig.4.2(b), are recorded at one location showing the average of not more than twenty single loops. If we add errors bars to the $I_C U$-characteristics reflecting the standard deviation, we see a monotonic tendency of scattering of I_C-data with larger absolute collector currents, which is also seen in the

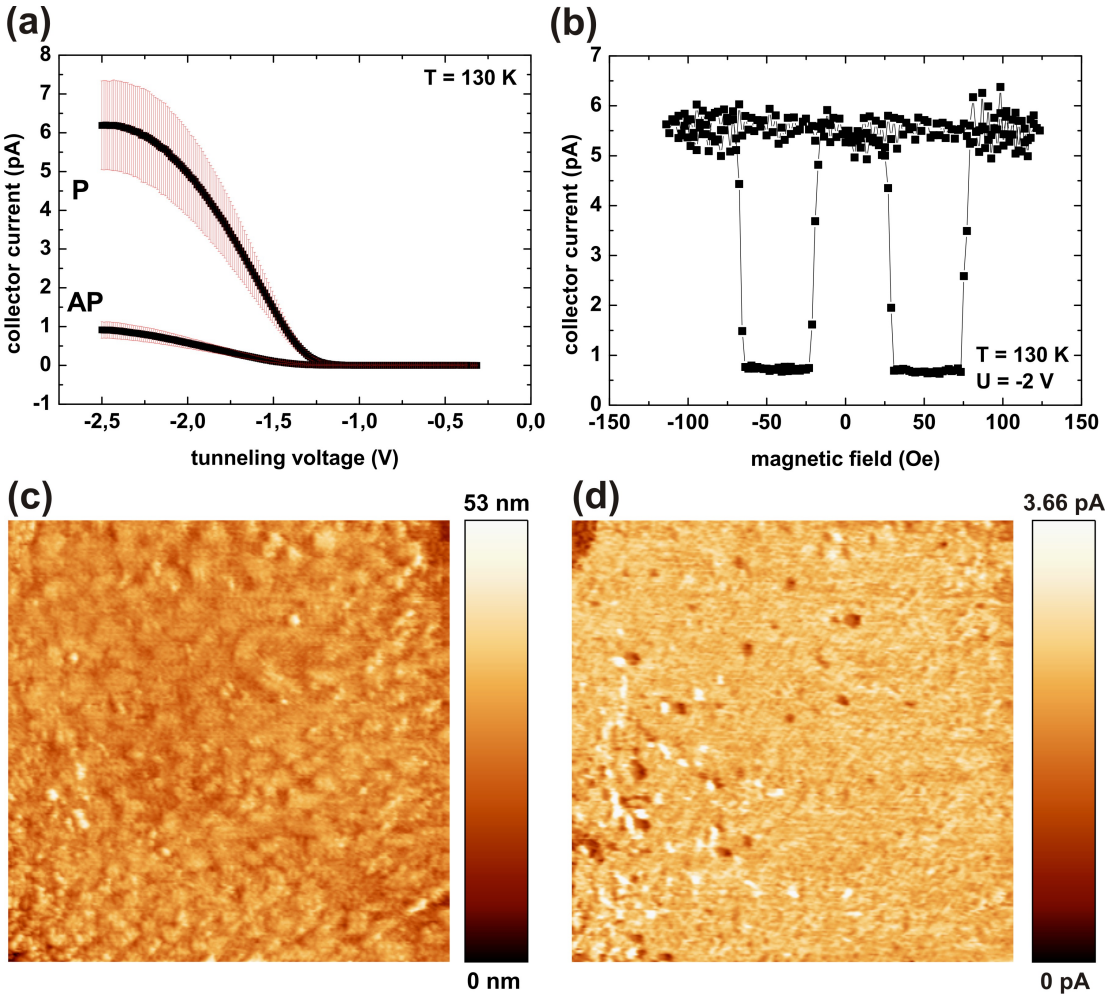

Figure 4.3: Statistic of $I_C U$-characteristics obtained at random STM-tip position on the sample surface showing the average value with their standard deviation (a) and a corresponding hysteresis loop obtained on one STM-tip position (b). By performing microscopy with STM (c) and BEEM (d) an inhomogeneous hot electron transmission is revealed. The edge length of the images equals 4 µm and the measurement parameters are T=250 K and U=-1.7 V. Data is obtained using a 18.7 nm Au/2.9 nm $Fe_{34}Co_{66}$/ 10.8 nm Au/5 nm $Fe_{34}Co_{66}$ spin valve stack with tunneling currents of I_T=20 nA.

hysteresis loops, see Fig.4.3. For this, we state a twofold origin.

The error bars stem not only from noise within the single characteristics, but also from scattering of the single curves itself as a consequence of spatially varying transport properties as visible by recording I_C as function of tip position, see Fig.4.3(c) and (d). These images demonstrate that the collector current is not homogenous across the sample surface and obviously reflects to some extent the topographic corrugation aside from electron transport properties. Variations of the thickness of the base layers lead

to an inverted contrast between the STM-images revealing the topography and BEEM-images revealing the hot electron transmissivity. Other reasons may be found in spatially varying surface gradients, impurities, lattice defects, adsorbates and in the height of the Schottky barrier. The latter is stochastically distributed over the interface area and we can readily assume variations of Φ_{SB} up to 100 meV [36, 82], which affect the entire $I_C U$-characteristic. Aside from inhomogeneous transport properties an intrinsic contribution to current noise appears even when a constant STM-tip position is maintained on the sample surface. This is particularly visible in hysteresis loops. It is known that electron transport over the Schottky barrier contributes a shot noise [6]. Yet, its low amplitude cannot account for the large I_C-variations. The scaling of the noise amplitude with I_C strongly suggests to be an attenuated replica of the current noise, which already adheres to I_T. Within the base layers ballistic currents originating from I_T are attenuated just as well as the noise amplitude of I_T.

The spin contrast visible in all graphs of Fig.4.2 gets trigonometrically reduced when magnetic misalignments, i.e. relative angles between the magnetization vectors apart from 0° and 180°, are accessible. By toggling between the two quantization axis of the ferromagnetic layers, the respective spin species do not any more ideally project onto each other and the identities $I_C^{\max} = I_C^P$ and $I_C^{\min} = I_C^{AP}$ loose their validity. By introducing angles α and β respecting the corresponding deviations from parallel and antiparallel magnetization configuration, we can write

$$I_C^{\max} = \left(I_C^P - I_C^{AP}\right) \cos^2 \frac{\alpha}{2} + I_C^{AP} \tag{4.1}$$

$$I_C^{\min} = \left(I_C^{AP} - I_C^P\right) \cos^2 \frac{\beta}{2} + I_C^P. \tag{4.2}$$

We express the spin contrast resulting from $I_C^{\max}$ and $I_C^{\min}$ in an effective magnetocurrent value MC* as

$$\begin{aligned} \mathrm{MC}^* &= \frac{I_C^{\max} - I_C^{\min}}{I_C^{\min}} \\ &= \frac{\mathrm{MC}\left(\cos^2 \frac{\alpha}{2} + \cos^2 \frac{\beta}{2} - 1\right)}{\mathrm{MC}\left(1 - \cos^2 \frac{\beta}{2}\right) + 1}. \end{aligned} \tag{4.3}$$

Note that MC* collapses to MC when $\alpha = \beta = 0$ and to $\mathrm{MC} \cos^2 \frac{\alpha}{2}$ for $\beta = 0$. Due to the denominator of the last formula depending on β rather than α MC^* is more sensitive on slight misalignments of antiparallel magnetization configuration than on deviations from parallelly aligned magnetic moments, see Fig.4.4. Any evaluation of majority and minority spin quantities demands the determination of I_C^P and I_C^{AP}. To extract these values from spin valve studies with misaligned magnetization vectors the determination of MC^*, α and β is needed for a thorough interpretation.

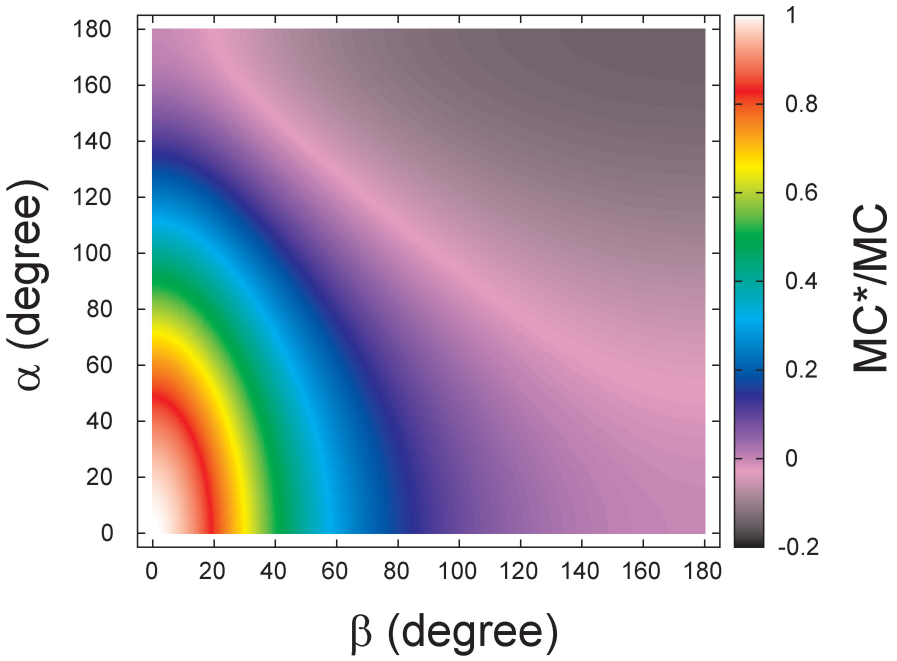

Figure 4.4: Effective magnetocurrent MC* as a function of angular deviation α and β from parallel and antiparallel magnetization configuration of the spin valve using formula 4.3 with MC = 6 = 600 %.

4.3 Hot electron transport and magnetic anisotropy of $Fe_{34}Co_{66}$/Au/$Fe_{34}Co_{66}$ spin valves

Yet, we lack the evidence that the two levels of I_C, i.e. the maximum and minimum detectable collector current, observable in the hysteresis loops of $Fe_{34}Co_{66}$/Au/$Fe_{34}Co_{66}$ spin valves, coincide with parallel and antiparallel magnetization configuration, respectively, see Fig.4.2(c). So far, we may only define an effective MC* rather than an absolute magnetocurrent, but we will show in the following that this coincidence is given when the external field is applied along the [110]-axis of the substrate. Quite the contrary, other field orientations prevent the achievement of an antiparallel magnetization configuration and very distinct magnetization reversals emerge.

Since only ultrathin magnetic films are involved, we can state that the magnetization vectors are always oriented within the film plane as energetically favored by the magnetic shape anisotropy [112]. Due to the single crystalline nature of the ferromagnetic layers additional magnetocrystalline anisotropies reflecting the lattice symmetry arise. It is reported that $Fe_{34}Co_{66}$ grows epitaxially onto GaAs(100)-substrates in the structure bcc $Fe_{34}Co_{66}$(100)<010> || GaAs(100)<010> [113]. This layer system shows a magnetic in-plane uniaxial anisotropy of pure interface origin with an easy axis along

the [110]-direction of the substrate lattice and with a strength determined by the constant $K_{u,||}^{\mathrm{eff}}$ [114]. Its microscopic origin is mostly ascribed to an anisotropic interface, which influences the magnetic response via spin-orbit interaction [115]. Furthermore, the tetragonal bcc lattice provides an in-plane fourfold magnetocrystalline anisotropy with two magnetic easy axes along [110] and [1-10] for film thicknesses larger than 7 monolayers. Note that the corresponding anisotropy constant $K_{1,||}^{\mathrm{eff}}$ shares bulk (index V) and surface/interface (index I) contributions due to the altered coordination of atoms at surfaces/interfaces [116]. We write therefore

$$K_{u,||}^{\mathrm{eff}} = \frac{1}{d} K_u^{\mathrm{S}} \tag{4.4}$$

$$K_{1,||}^{\mathrm{eff}} = K_1^{\mathrm{V}} + \frac{1}{d} K_1^{\mathrm{I1}} + \frac{1}{d} K_1^{\mathrm{I2}} \tag{4.5}$$

while d denotes the thickness of the considered ferromagnetic film and the indices I1 and I2 reflect the two interfaces of the thin film. The corresponding in-plane anisotropy energy $E_{||}$ per unit volume can be written as [112, 117]

$$E_{||} = -\frac{K_{1,||}^{\mathrm{eff}}}{2} \left(\alpha_x^4 + \alpha_y^4 \right) - K_{u,||}^{\mathrm{eff}} \cos^2 \phi \tag{4.6}$$

with α_x and α_y defined as [118]

$$\alpha_x = \cos \phi \tag{4.7}$$

$$\alpha_y = \sin \phi. \tag{4.8}$$

The angle ϕ reflects the deflection angle from the [110]-axis. Although we have to respect the case of $Fe_{34}Co_{66}$ grown onto $GaAs_{67}P_{33}(100)$ rather than GaAs(100), we do not expect very distinct magnetic anisotropies due to the additional phosphide compound, compare the discussion in [115]. Once the magnetic easy axis of the FM1-layer is found, we constitute it to be the [110]-axis of the substrate in the following without any further verification.

In order to determine the relevant magnetization configurations and to highlight the magnetization reversal processes, we determine the magnetic anisotropies by Ferromagnetic Resonance (FMR). In a second step these results will serve as input for simulations of hysteresis loops, which are obtained on microscopic scales with BEEM and, complementary, on macroscopic scales with magneto-optic Kerr (MOKE) effect measurements, as well. We perform this procedure exemplarily on one sample with the layer structure 5 nm Au/ 2.9 nm $Fe_{34}Co_{66}$/ 3.6 nm Au/2.9 nm $Fe_{34}Co_{66}$/n-$GaAs_{67}P_{33}(100)$ with all three experiments carried out at ambient conditions.

For the sample characterization with FMR a 22 GHz radiofrequency (rf) and a dc magnetic field are applied in the film plane perpendicularly oriented with respect to each other. The resulting resonance fields as well as the coercive fields are distinct

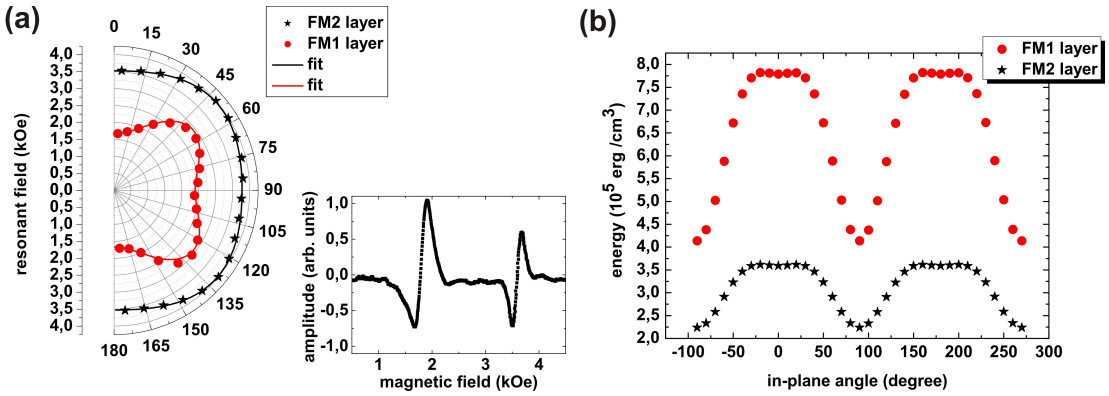

Figure 4.5: Ferromagnetic resonance fields of a layer stack of 5 nm Au/ 2.9 nm $Fe_{34}Co_{66}$/ 3.6 nm Au/2.9 nm $Fe_{34}Co_{66}$/n-$GaAs_{67}P_{33}$(100) and their corresponding in-plane angle dependence noted with respect to the [110]-axis of the $GaAs_{67}P_{33}$(100)-substrate (a). The solid lines are fits with the linearized Landau-Lifshitz equation of motion [118]. In-plane anisotropy energy per unit volume calculated with formula 4.6 shows the presence of an uniaxial and a fourfold magnetic anisotropy in the two $Fe_{34}Co_{66}$ layers (b).

for the two $Fe_{34}Co_{66}$-layers due to distinct magnetic anisotropies. Resonances show up as derivatives of Lorentzians due to the employed lock in-technique and are obtained as a function of the in-plane angle ϕ of the static magnetic field with respect to the [110]-axis, see Fig.4.5(a). The low field resonance corresponds to the layer with the larger magnetic anisotropy, i.e. the FM1-layer, and the high field resonance to the FM2-layer, respectively. This data is analyzed by using the linearized Landau Lifshitz equation of motion [112, 117] revealing the anisotropy constants $K^{\text{eff}}_{1,||}$ to be 4.4×10^5 and $1.8\times10^5\,\text{erg/cm}^{-3}$ and $K^{\text{eff}}_{u,||}$ to be 3.7×10^5 and $1.4\times10^5\,\text{erg/cm}^{-3}$ for the FM1 and FM2 layer, respectively. For this procedure a g-factor of 2.15 and a saturation magnetization of $4\pi M_S$ =24 kOe is used. Note that the data of the FM2-layer can be well fitted with an additional uniaxial term, only. It may be caused by several factors like lattice strain, inter-diffusion of the metallic layers, additional interface anisotropies or a significant coupling of the magnetic moments of the two ferromagnetic layers. We continue by calculating the anisotropy energy per unit volume using formula 4.6, where the overall magnetic easy axes appear as global minima. According to Fig.4.5(b) both ferromagnetic layers exhibit just one magnetic easy axis, which are aligned parallel with respect to each other along the [110]-axis of the substrate.

When the magnetic field is swept along this axis, hysteresis loops of a very rectangular shape are obtained revealing that domain wall motion dominates the magnetization reversal over spin rotation processes, see Fig.4.6(a) and (b). In order to achieve a quantitative statement about the magnetization alignment of the spin valve during the reversal, we simulate the hysteresis loops with the already determined magnetic anisotropies. In

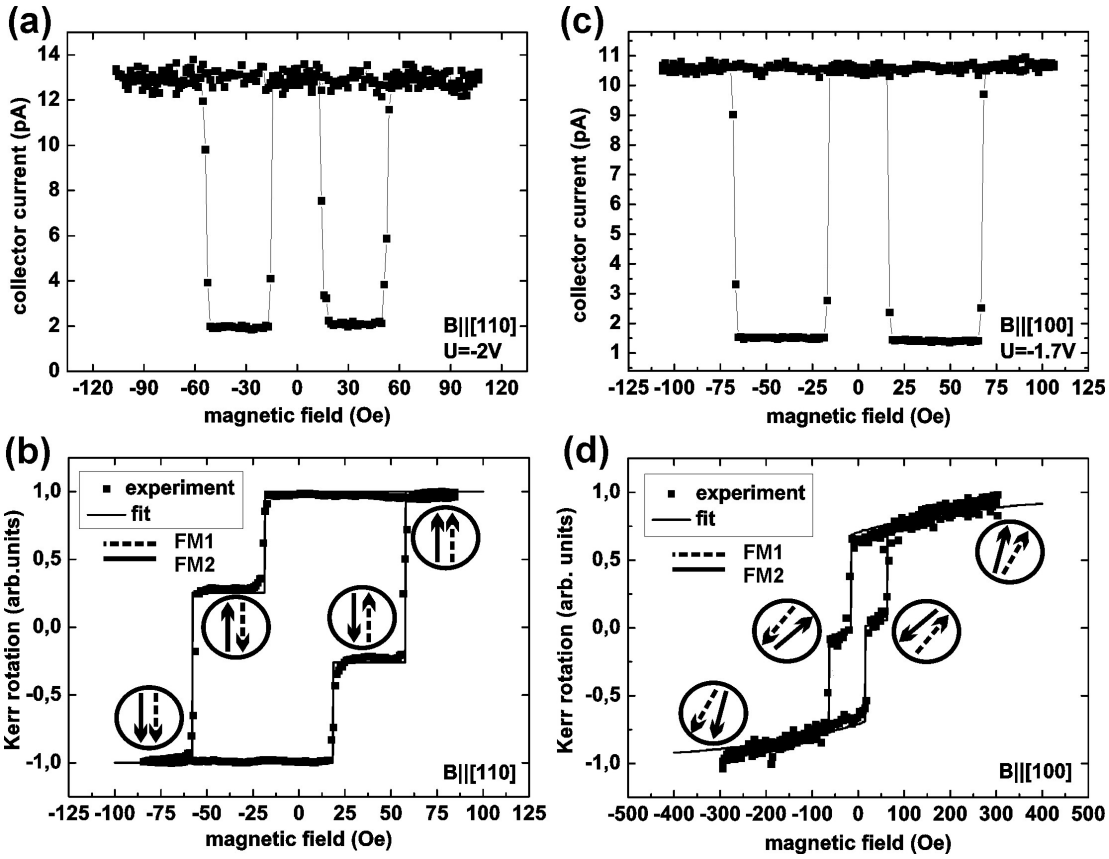

Figure 4.6: BEEM (a,c) and MOKE (b,d) hysteresis loops obtained with an external magnetic field applied along the magnetic easy (a,b) and hard axis (c,d). Solid lines in (c) and (d) are simulations based on the corresponding anisotropy constants [119]. Data recorded at ambient conditions with a tunneling current set to 20 nA.

the simulations the magnetization vector is determined by energy minimization of the corresponding anisotropy energy and the only free parameter is the domain wall energy. The latter is adjusted so that the simulated curve shows the same coercive fields as the experimental data. The simulated hysteresis loops evidence that only perfect collinear magnetization configurations of the spin valve are accessible, see Fig.4.6(b, solid line) when the field is applied along the magnetic easy [110]-axis, which is very favorable for studying magnetocurrent effects. Since both $Fe_{34}Co_{66}$ layers have the same thickness, the smaller Kerr rotation and therefore the lower coercive field H_c with a mean value of 15 Oe is attributed to the more buried FM1-layer, while the FM2-layer shows average switching fields of 53 Oe. This assignment becomes more evident when the relative amplitude of the MOKE hysteresis loop at H_c is recorded for distinct thicknesses of the ferromagnetic films, see Fig.4.7.

In a second set of BEEM experiments the external magnetic field is applied and swept

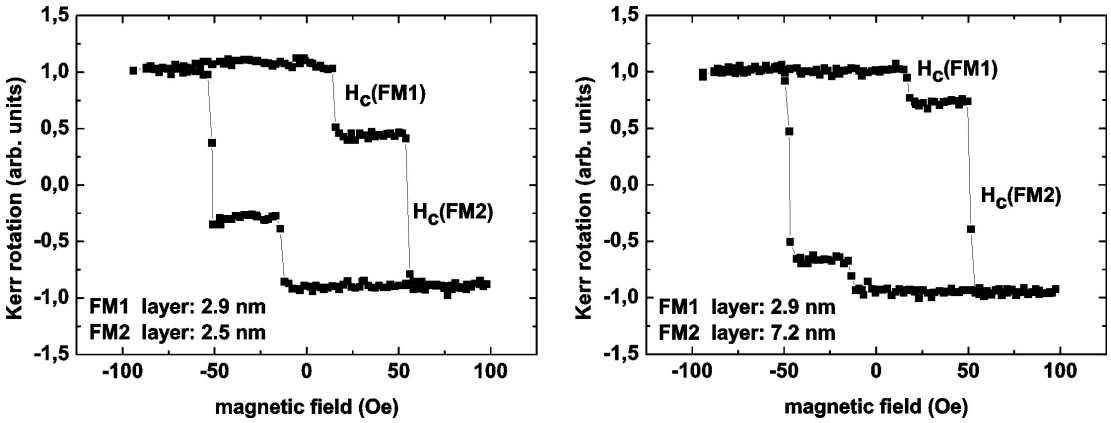

Figure 4.7: MOKE hysteresis loops recorded with an external magnetic field applied along the magnetic easy axes at ambient conditions using two spin valve stacks with a distinct ratio of thicknesses of the ferromagnetic layers.

along the [100]-axis. According to the FMR results of Fig.4.5 this crystallographic direction represents the magnetic hard axis for both ferromagnetic layers. From Fig.4.6(c) we recognize that the local hysteresis loops obtained with BEEM are once more of rectangular shape, however, with significantly increased coercive fields compared to the magnetization reversal along the easy [110]-axis. On the contrary, magnetization reversals recorded with MOKE are not any more ideally rectangularly shaped but exhibit a continuous bending, see Fig.4.6(d). Hence, the reversal is mediated by domain wall motion and by spin rotation processes. With the revealed magnetic anisotropies this curve is also simulated and adjusted to the experimental data by the variation of the domain wall energy, see Fig.4.6(d, solid line). When the magnetic field is decreased from the saturation state along the [100]-axis, both magnetization vectors rotate out of the [100]-axis towards the neighboring global minimum in the energy landscape, i.e. towards the magnetic easy [110]-axis. At remanence the magnetization vectors are then oriented parallel to each other and along [110] with respect to the substrate lattice. By reversing and continuously increasing the field both magnetizations start to rotate towards [-100] and, once the field is sufficiently large, they switch by about 180 degrees via domain wall nucleation and motion into the vicinity of the [-1-10]-axis. A further increase of the field leads to magnetization rotation towards the [-100]-direction until saturation is reached. The lower coercive field of 18 Oe is provided by the FM1-layer and the larger one of 67 Oe of the FM2-layer, respectively. The fact that the magnetization rotation of the MOKE data is not observed in the BEEM data is the result of an almost parallel rotation process. Recall that I_C is sensitive to the relative angle between the two magnetizations, only. Moreover, I_C responds with a cosine scaling to angular deviations α from parallel magnetization configuration, which reduces the sensitivity of

I_C to small angles α.

Magnetic field sweeps along the [1-10]-axis give rise to the hysteresis loops of Fig.4.8 (a) and (b). By referring to the FMR results of Fig.4.5 this direction represents an intermediate magnetic axis of both $Fe_{34}Co_{66}$ layers. At first glance, we recognize three plateaus in the BEEM hysteresis loop. We can attribute them to an almost parallel, antiparallel and an nearly 90 degree configuration of the spin valve when we compare them to the I_C-values of the already analyzed characteristics of Fig.4.6(a). Obviously, magnetization saturation of the spin valve along this [1-10]-axis is never reached, because the largest applicable fields of ± 150 Oe of the ambient condition BEEM setup are not sufficient to create the maximum detectable collector current.

In contrast to this data, the macroscopic magnetization behavior studied by MOKE reveals no sharp magnetic switching and plateaus. For clarity only one sweep direction is shown, see Fig.4.8(b). We observe, however, four humps each with a steep and softened step and, additionally, a non-vanishing slope indicating magnetization rotation processes at all external fields. Let us now proceed to make quantitative statements by simulating the hysteresis curves (points 1-6 in Fig.4.8(b) and red dashed line in Fig.4.8(d)) and by extracting the magnetization configuration at the most interesting points of the curve. With an almost 90 degree configuration of the spin valve at fields of ± 150 Oe and a parallel (point 2,3) and antiparallel (point 5,6) configuration at field values around remanence the simulated loop reproduces satisfactorily the local hysteresis loop at most points during magnetization reversal. However, at field values of about ± 70 Oe the BEEM data shows a sharp change of the spin valve configuration between an almost parallel and almost antiparallel state, which is not reproduced in this simulation, see Fig.4.8(d) red dashed line. On the other hand, this difference can be well explained in terms of small angular deviations of the magnetic field from [1-10].

Fig.4.8(c) and (d) demonstrate the resulting MOKE and BEEM characteristics accompanied by the calculated magnetization configurations when the magnetic field is swept along a direction deviating 2 degree from the [1-10]-axis (points 1-6 in Fig.4.8(c) and (d, blue solid line)). The FM2-layer magnetization is aligned parallel with the external magnetic field at 150 Oe, while the FM1-layer magnetization vector points nearly towards the [110]-direction, such that a magnetization configuration with a relative angle of approximately 90 degree is reached. By reducing the field a coherent spin rotation of the FM1-layer towards the magnetic easy [110]-axis emerges, while the FM2-layer magnetization is trapped between energy maxima in the $\langle 100 \rangle$-directions arising from the fourfold crystal anisotropy. The rotation process is also visible in the BEEM data as a nonvanishing slope. Further decreasing the field forces the FM2-layer magnetization to overcome these barriers by nucleating magnetic domains as evidenced by the sharp change in the BEEM hysteresis loop at an external field of 89 Oe or the sharp change in

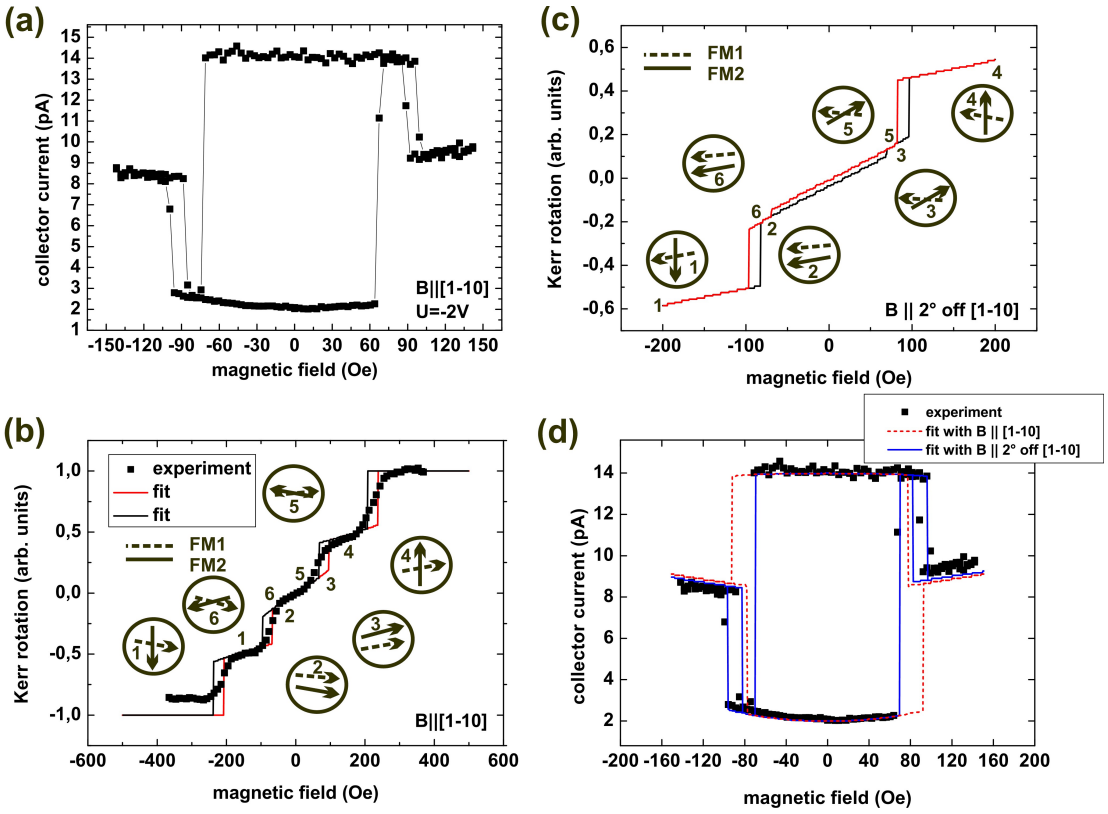

Figure 4.8: BEEM (a,d) and MOKE (b) hysteresis loops obtained with an external magnetic field applied along the magnetic intermediate [1-10] axis combined with the corresponding hysteresis simulations ((b) solid line and (d) red dashed line) being based on the magnetic anisotropy constants. Simulated hysteresis loops when the external field is applied along a direction deviating 2 degrees from the [1-10]-axis ((c) and (d) blue solid line). Data recorded at ambient conditions with a tunneling current set to 20 nA, see also [119].

Fig.4.8(c, point 2). The two magnetization vectors are aligned almost parallel pointing into the vicinity of [110] then. Sweeping the field from 89 Oe to -75 Oe the magnetization configuration remains apparently almost parallel since no significant change in the collector current can be seen. The simulation tells us that both magnetization vectors corotate slowly and around [110] until at -75 Oe the FM2 layer magnetization flips by almost 180 degree into the vicinity of [-1-10] via domain wall nucleation and motion forcing the spin valve into an almost antiparallel configuration. In Fig.4.8(c) this configuration is visible at point 3. Continuing the raise of the reversed magnetic field excites another domain wall mediated reversal of the FM2 layer magnetization. At field values of -99 Oe, it switches from the vicinity of [-1-10] by about 90 degree into [-110]. Note that the FM1-layer magnetization still points into the vicinity of [110] and becomes

only slightly deflected up to fields of -150 Oe, creating again a spin valve configuration of about 90 degree, see Fig.4.8(c, point 4). By reversing the sign of the sweep a similar magnetic behavior is obtained, yet, the local BEEM hysteresis loop and the corresponding simulated curve show a distinct bending around remanence when compared to the former case of the upsweep. This difference arises due to the counterrotation of the magnetization vectors generating larger relative angles than the corotation process. In conclusion, the magnetization reversal mechanisms underlying the experimental data of Fig.4.8(a) are mostly a result of magnetization realignment in the FM2 layer while the magnetization orientation of the FM1-layer remains always close to the magnetic easy [110]-axis. Interestingly, for this sweep direction the FM2-layer magnetization is more easily inverted than the FM1-layer in contrast to the sweeps along the magnetic easy and hard axis.

4.4 Hot electron transport in bcc $Fe_{34}Co_{66}$

The ratio of the spin dependent mean free paths (MFP's) for electron transport at the Fermi level E_F can exhibit values as large as 9 in the case of Co [120] ($\lambda_M(E_F)$=5.5 nm, $\lambda_m(E_F)$=0.6 nm). If the electron energy is raised into the hot electron regime, the underlying transport properties become modified but still show a large spin asymmetry as confirmed by large magnetocurrent values. In the literature MC values up to 3400 % obtained at low temperatures (77 K) are reported reflecting a hot electron spin polarization approaching 100 % [26]. Since this effect is based upon electron filtering, the magnetocurrent can be raised beyond any limits by increasing the thickness of the ferromagnetic layers involved in the spin valve, however, at the expense of a reduced collector current.

As already stated above the reason for the large MC values reported is commonly attributed to spin dependent group velocities and scattering processes suppressing efficiently hot minority spin electrons in the transport through ferromagnetic materials. We investigate this transport spin dependently by the variation of the thickness of the FM2-layer involved in $Fe_{34}Co_{66}$/Au/$Fe_{34}Co_{66}$ spin valves. In doing so, we answer the question, whether the large electron spin polarization arises from interface or from bulk effects. Additionally, we extract the hot electron scattering or attenuation length $\lambda_{M(m)}$ representing the thickness of the considered material necessary to reduce the collector current by a factor of e^{-1}. Strictly adhering to this definition, the obtained attenuation length is greater or equal the MFP, because scattering does not automatically transfer hot electrons to undetectable states and contributions of secondary electrons are not negligible.

Spin dependent attenuation lengths have been evaluated by SVT, MTT and BEEM ex-

periments for Co, NiFe- and FeCo-alloys [8, 39, 99, 121], however, a direct comparison of the results reveals that the experimentally determined λ cannot be interpreted as a material parameter only (compare e.g. Co $\lambda_M(1.4\,\mathrm{eV})$=2.3 nm [8], $\lambda_M(1.4\,\mathrm{eV})$=6.8±0.3 nm, $\lambda_M(1.4\,\mathrm{eV})$=3.5±0.2 nm [99]). Reasons for the poor reproducibility may lie in different tunnel barriers [99], a modified crystalline quality of the base layers (modified density of defects) and different substrates due to changed electronic states building up I_C. Additional reasons may be found in randomly mismatched k-vectors of the hot electrons during transport through differently orientated crystallites in a polycrystalline base layer and in MC-values calculated by the largest and lowest detectable collector current as a consequence of unknown magnetization reversal mechanisms. Since we investigate fully epitaxial spin valves, we benefit from a reproducible crystalline structure and therefore from a reproducible electron wave-vector in the base. In addition, hot electron transport is less affected by the obscuring nature of elastic scattering at grain boundaries and parallel and antiparallel magnetization configuration are readily achievable by applying the external magnetic field along the magnetic easy axis.

The samples employed in this study consist of spin valve layer stacks of 2.9 nm $Fe_{34}Co_{66}$/ 10.8 nm Au/ d_{FM2} nm $Fe_{34}Co_{66}$ capped with a thick 18.7 nm Au film as verified by cross sectional TEM. d_{FM2} denotes the variable thickness used for the thickness dependent study. Several (some hundred up to thousand) I_CU-spectra in parallel and antiparallel magnetization configuration randomly distributed over the surface are obtained on each sample. Note that this experiment is carried out at ambient conditions with tunneling currents of 30 nA (unless stated otherwise). In addition, hysteresis loops are exemplarily recorded on single sample locations to assure the availability of parallel and antiparallel magnetization configuration. But it turned out that this requirement is always met.

4.4.1 Magnetocurrent and hot electron spin polarization

From the set of I_CU-characteristics of each sample we calculate thereafter the dependence of the spin contrast on the tunneling voltage. In Fig.4.9(b) we recognize that the magnetocurrent effect is increasing with the thickness of the ferromagnetic films and monotonically decreasing with increasing absolute value of the tunneling voltage. The error bars reflect the standard error of the mean. Due to the optimistic definition of the magnetocurrent with the lower current I_C^{AP} in the denominator, error bars experience a relative strong rise when I_C^{AP} becomes small. However, reliable magnetocurrent values up to 1200 % are recognizable at bias voltages slightly above the Schottky barrier height of 1 eV, which represents the largest value measured at room temperature so far. By comparing this study to related experiments [8, 39, 99, 121] we see that this large spin contrast stems not from large film thicknesses, only. We can also see from Fig.4.9(b) that for thicknesses larger than 3.2 nm the MC changes only slightly when the film

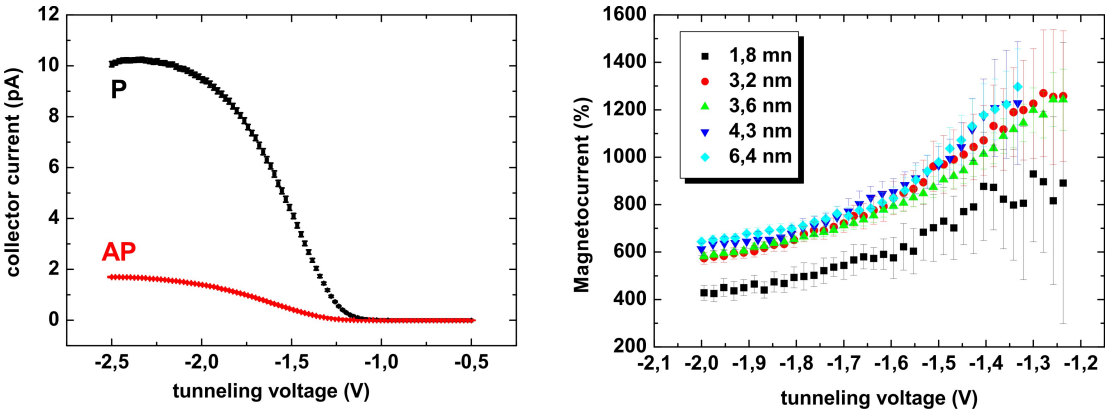

Figure 4.9: Mean value of some hundred $I_C U$-characteristics obtained on one spin valve stack (d_{FM2}=3.6 nm) of the sample series employed for this study. The small error bars reflect the standard error of the mean (left). Dependence of magnetocurrent on tunneling voltage for distinct thicknesses of the FM2 ferromagnetic layer.

thickness is increased further. At this point almost all minority spin hot electrons have already been filtered out.

Now let us focus on the bias dependence. The more the injection energy exceeds the Schottky barrier height the less the barrier acts as a filter. The momentum filter efficiency is reduced since more conducting states are available in the semiconductor. The probability of scattered or quasi-ballistic (mostly minority spin) hot electrons contributing to the collector current increases therefore with electron energy, which gives rise to a smaller MC.

By introducing factors $\Gamma_{i(o)}$ reflecting the spin dependent input (index i) and output (index o) transmission for hot electrons at the interfaces of the considered base layer we account for the possibility of a spin dependent bandstructure mismatch. We can write therefore

$$I_C^P \sim T_M^{\mathrm{FM1}} T_M^{\mathrm{FM2}} + T_m^{\mathrm{FM1}} T_m^{\mathrm{FM2}} \tag{4.9}$$

$$I_C^{AP} \sim T_M^{\mathrm{FM1}} T_m^{\mathrm{FM2}} + T_m^{\mathrm{FM1}} T_M^{\mathrm{FM2}} \tag{4.10}$$

with the overall spin dependent hot electron transmission of the considered base layer given by

$$T_{M(m)} = \Gamma_{M(m),i} \exp\left(-\frac{d}{\lambda_{M(m)}}\right) \Gamma_{M(m),o}, \tag{4.11}$$

compare [121]. Benefitting from the last formula we find a correlation between the ferromagnetic layer thickness d and the resulting hot electron spin polarization via

$$P = \frac{T_M - T_m}{T_M + T_m}, \tag{4.12}$$

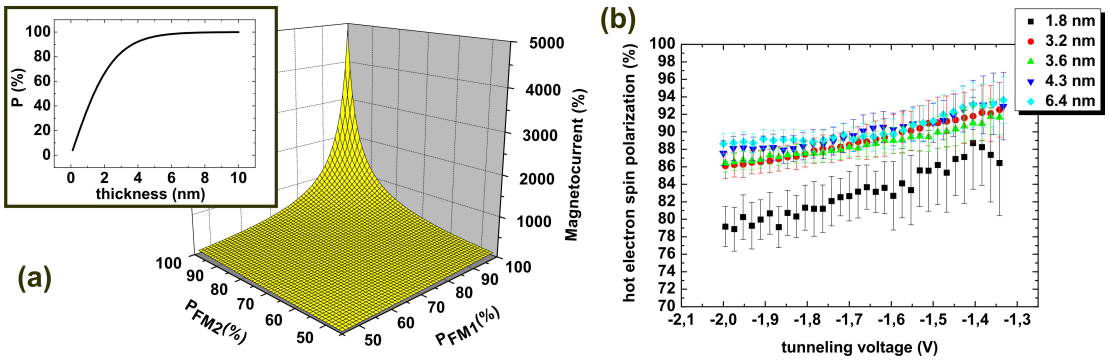

Figure 4.10: Magnetocurrent in context of hot electron spin polarization P of two bcc $Fe_{34}Co_{66}$ layers (a) and P as a function of film thickness calculated with $\lambda_M = 5\,\text{nm}$ and $\lambda_m = 1\,\text{nm}$ (inset of (a)). Dependence of P on the tunneling voltage for different thick $Fe_{34}Co_{66}$-layers (b). Data calculated with formula 4.13 and with the data of Fig.4.9.

which in turn permits the magnetocurrent to be expressed in terms of P by using Julliere's formula [122] via

$$\begin{aligned} \text{MC} &= \frac{I_C^P - I_C^{AP}}{I_C^{AP}} \\ &= \frac{2P^{\text{FM1}}P^{\text{FM1}}}{1 - P^{\text{FM1}}P^{\text{FM1}}}. \end{aligned} \tag{4.13}$$

In terms of hot electron spin polarization there is no significant difference between $d = 2.9\,\text{nm}$ and $d = 3.2\,\text{nm}$, see Fig.4.10. Thus, we can use the data of the spin valve with $d^{\text{FM1}} = 2.9\,\text{nm}$ and $d^{\text{FM2}} = 3.2\,\text{nm}$ of Fig.4.9 and treat both ferromagnetic layers to be 2.9 nm thick. In doing so, formula 4.13 collapses to MC=$2P^2/(1-P^2)$ and we can determine P as a function of U for a $Fe_{34}Co_{66}$-layer thickness of 2.9 nm. In a second step, we use this value as P^{FM1} for the remaining spin valve data of Fig.4.9 and extract P for distinct thicknesses of the $Fe_{34}Co_{66}$ layer.

One $Fe_{34}Co_{66}$ layer as thin as 1.8 nm is already sufficient to create a hot electron spin polarization of 88 % at $U = -1.4\,\text{V}$ and of 79 % at $U = -2\,\text{V}$, see Fig.4.10(b). When the film thickness is raised to 3.2 nm, one obtains 92 % and 86 %. By raising the ferromagnetic film thickness the resulting hot electron spin polarization becomes enhanced, however, apparently with a reduced rate when P approximates 100 %. This tendency is also predicted by formula 4.12, see inset of Fig.4.10(a). The monotonic reduction of P with an increasing absolute value of the tunneling voltage is governed by the same behavior of the magnetocurrent, compare Fig.4.9(b) and 4.10(b).

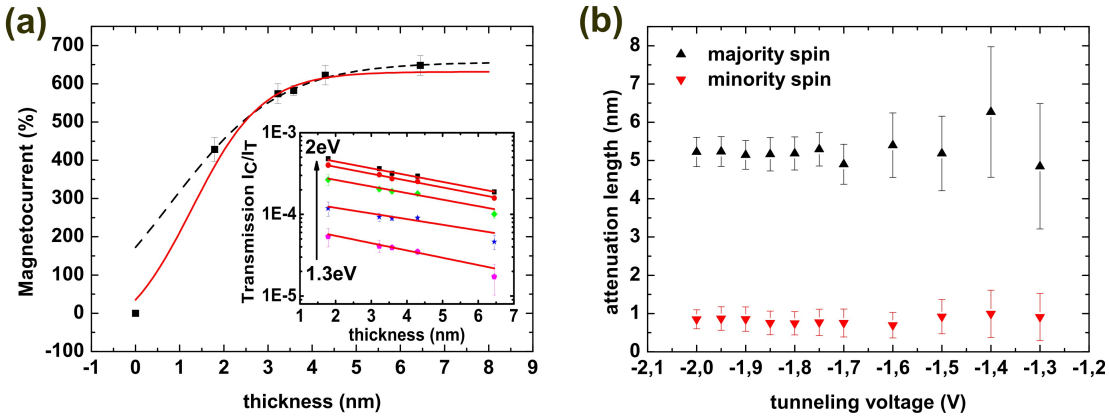

Figure 4.11: Transmission in parallel magnetization configuration for bias voltages of -1.3 V, -1.4 V, -1.6 V, -1.8 V and -2 V (inset (a)) and MC for different $Fe_{34}Co_{66}$ thicknesses d_1 using $U = -2\,\mathrm{V}$ (a). The solid/dashed lines represent fits using formula 4.15 with/ without interface spin asymmetry while the solid lines in the inset are linear fits to the data. Spin dependent attenuation lengths and their bias dependence of bcc $Fe_{34}Co_{66}$ (b). Up/Down triangles stand for majority/minority spins.

4.4.2 Spin dependent attenuation lengths of bcc $Fe_{34}Co_{66}$

The inset of Figure 4.11(a) shows the transmission I_C/I_T for parallel magnetization alignment as a function of the film thickness of one of the $Fe_{34}Co_{66}$-layers involved in the spin valve. This behavior can be described by

$$\frac{I_C^P}{I_T} \sim \Gamma_{1i}^M \Gamma_{1o}^M \Gamma_{2i}^M \Gamma_{2o}^M \exp\left(-\frac{d_1+d_2}{\lambda_M}\right) + \Gamma_{1i}^m \Gamma_{1o}^m \Gamma_{2i}^m \Gamma_{2o}^m \exp\left(-\frac{d_1+d_2}{\lambda_m}\right). \quad (4.14)$$

The second term is negligible with respect to the first term for sufficiently thick $Fe_{34}Co_{66}$-layers and leads to an exponential thickness dependence of the transmission, as observed here. Using a linear fit to the data we extract the majority spin attenuation length from the slope of the curves shown in the inset of Fig.4.11(a). In order to compute the minority spin attenuation length we rewrite the MC by using formula 4.14 combined with $\lambda^- = (\lambda_m^{-1} - \lambda_M^{-1})^{-1}$ and two interface parameters $\alpha = \Gamma_{1i}^m \Gamma_{1o}^m / \Gamma_{1i}^M \Gamma_{1o}^M$ and $\beta = \Gamma_{2i}^m \Gamma_{2o}^m / \Gamma_{2i}^M \Gamma_{2o}^M$ as follows [45]

$$\mathrm{MC} = \frac{1 + \alpha\beta \exp\left(-\frac{d_1+d_2}{\lambda^-}\right)}{\alpha \exp\left(-\frac{d_1}{\lambda^-}\right) + \beta \exp\left(-\frac{d_2}{\lambda^-}\right)} - 1. \quad (4.15)$$

In the next step formula 4.15 is fitted to the thickness dependence of the MC by the variation of the three parameters α, β and λ^-. With the already determined λ_M and the value of λ^- we are able to calculate λ_m thereafter. An example of the fitting results is given in Fig.4.11(a). The fit can be performed with and without spin asymmetry at the

base interfaces (dashed and solid line). While the fit, which accounts for spin dependent interface scattering, leads to minority spin attenuation lengths of about 1 ± 0.2 nm, the fit with assumed zero spin dependent interface scattering through the graphs origin leads to smaller attenuation lengths of 0.7 nm. In the following, we make use of the average of both values combined with their average error in order to obtain the lower and upper limit for λ_m. Considering the case that the magnetocurrent effect is governed by hot electron scattering taking place at the film interfaces, Fig.4.11(a) would show no change of MC with film thickness, which is not observed here. Moreover the opposite holds and the observed hot electron transport is dominated by bulk properties, since the extrapolation of the dashed line in Fig.4.11(a) to zero taking a nonzero spin dependent interface transmission into account shows ordinate intercepts of MC$\approx 150\,\%$ only, while observed magnetocurrents reach values being several times larger.

In Fig.4.11(b) the dependence of the spin dependent attenuation lengths on the tunneling voltage is shown. Both lengths are almost independent of U within the measured energy interval of 1.3 up to 2 eV above the Fermi level. Integrated over this interval λ_m shows an average of 0.8 ± 0.4 nm and λ_M a value about 6 times larger around 5.2 ± 0.7 nm, demonstrating the strong spin asymmetry in bulk scattering.

4.4.2.1 Comparing attenuation lengths to literature values

At first glance the vanishing dependence of $\lambda_{M(m)}$ on U comes as a surprise. It differs from the energy dependence of the electronic lifetime. Let us address this question later and compare, at first, these results to a related MTT study [39] revealing the attenuation lengths for magnetron sputtered $Fe_{16}Co_{84}$ on GaAs(100). In doing so, we illuminate the role of the semiconductor with regard to transmission rates and to the determination of λ emphasizing again that λ cannot be a material parameter, only. The results of both studies are plotted in Fig.4.12. By comparison one recognizes that λ_m is in good agreement with respect to the energy dependence and the absolute value, however, λ_M is reproduced only roughly. Significant variations of more than 1 nm and unexplainable by the error bars are visible at tunneling voltages exceeding -1.7 V. Differences during the magnetization reversal in both studies can be ruled out to be the reason for the deviation due to the similar rectangular shape of the hysteresis loops, see [26]. The slight difference in the FeCo-alloy concentration as well as the different temperatures are also most likely irrelevant [99]. Crucial may be the influence of the different tunnel barriers on the determination of the attenuation lengths as well as the influence of the different substrates, which have to be quantified. A third argument responsible for larger absolute values of λ_M may lie in different crystalline structures leading to a lack of elastic scattering in the bulk of the base layers in this study.

Let us recall the current paths relevant for this thickness dependent BEEM study.

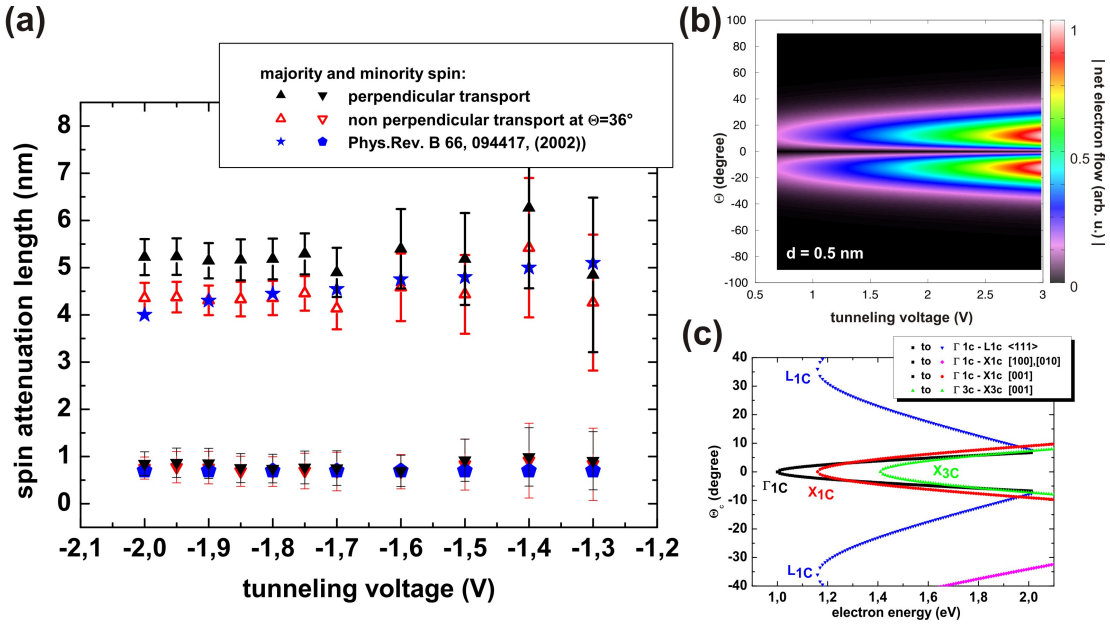

Figure 4.12: Spin dependent attenuation lengths of bcc $Fe_{34}Co_{66}$ and magnetron sputtered $Fe_{16}Co_{84}$ (a). The data of the latter film is extracted from [39]. Solid triangles reflect the data of Fig.4.11, which is assumed to reflect a perpendicularly orientated transport with respect to the interfaces. This assumption is supported by the narrow emission cone arising from emitter tunneling (b) combined with the narrow acceptance cone arising from the semiconductor bandstructure (c). Open triangles in (a) stand for an exclusive nonperpendicular ballistic transport into semiconductor L-valleys while blue stars/pentagons are results from a MTT study for magnetron sputtered $Fe_{16}Co_{84}$ using n-type GaAs(100) collectors [26].

The relative narrow tunneling emission cone peaking around $\Theta = 12°$ with respect to $\mathbf{k}_{||} = 0$ and the multitude of acceptance cones of the collector are replotted in Fig.4.12. Their combined effect on the current path selection favors a perpendicular ballistic transport with $k_{||} \approx 0$, i.e. around $\overline{\Gamma}$ along the vicinity of the [100]-axis of all the base layers. However, we also have to take the electronic bandstructure of the base layers into account and to check for conducting states. Although an ideal bandstructure calculation has to treat the whole layer stack as one supercell due to the inherent ballistic nature of this experiment, we utilize the bulk bandstructures of each base film for the sake of simplicity, see Fig.4.13. Within the relevant energy interval of 1 to 2 eV above E_F s- and d-like electronic bands are provided for both spin species along [100] by bcc $Fe_{34}Co_{66}$ but not by fcc Au, whose s-like band ends at the X-point at $E = 1.1$ eV above E_F. The resulting lack of conduction band states suppresses ballistic transport along [100] for $E > 1.1$ eV. At first glance this is strong in contrast to all the I_CU-characteristics shown above, which exhibit no well defined feature attributable to the occurrence of an

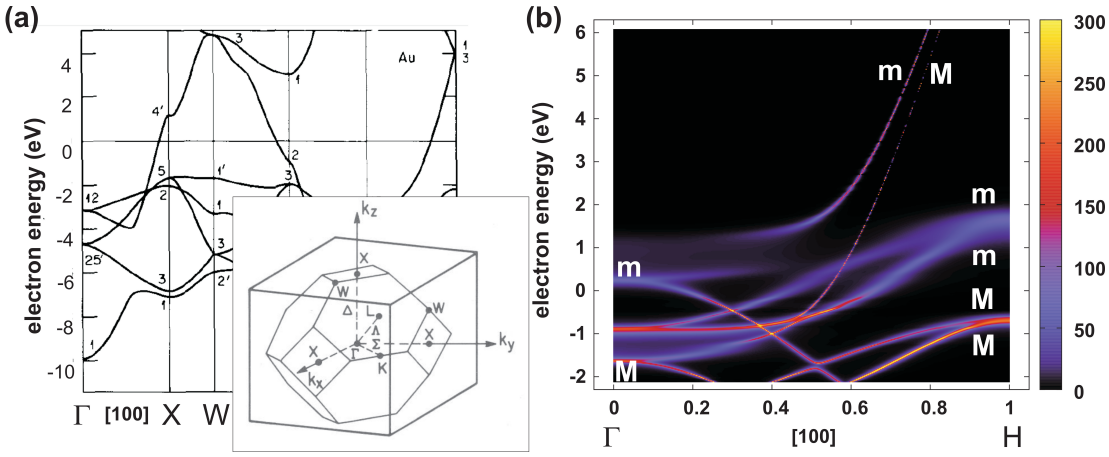

Figure 4.13: Electronic bandstructure of fcc Au (a) and bcc $Fe_{34}Co_{66}$ (b). Bands of the alloy are broadened as a result of disorder. Graphs extracted from [37] and [41].

energy gap. Only for larger tunneling voltages I_C is successively but relatively smoothly reduced. The lack of this feature can be ascribed to an energy gap around $\overline{\Gamma}$, which opens up quite slowly with increasing electron energy. The s-like band continues from X towards the very neighboring W-point up to energies beyond 4 eV[1]. Combined with the narrow but finite broadness of the emission and acceptance cones we can understand that the impact of the gold energy gap on I_C is accordingly weakened.

In conclusion, the matching of the tunneling emission cone with electronic bands of the base and of the semiconductor facilitates perpendicular hot electrons transport through the base. We have stated in the last chapter that only with the existence of strong scatterers in combination with a non-conservation of $k_{||}$ at the base layer interfaces a large contribution to the collector current via off-axis conduction band states seems to be likely. This, however, appears to be unlikely due to the relative large transmission values being among the largest ever measured on complete spin valve bases, compare [8, 25, 27, 44, 46, 47, 111, 123–127].

Interestingly, in the corresponding MTT devices hot electron transmission across the interface of magnetron sputtered $Fe_{16}Co_{84}$ and n-type GaAs(100) is found to be carried out via off-axis L-valleys rather than via on axis states of GaAs as evidenced by replicas appearing in the I_CU-spectra [128]. We attribute this difference to the very distinct electronic bandstructure of GaAs(100) compared to $GaAs_{67}P_{33}(100)$. For the former one all five X-valleys are available for hot electron transmission not until the electron energy is raised up to Φ_{SB}+0.47 eV. In addition, the on axis Γ-valley exhibits a relatively low density of states with respect to the L-valley as visible by their distinct effective masses ($m^*_\Gamma = 0.067m$, $m^*_{L,l} = 1.9m$, $m^*_{L,l} = 0.075m$ [89]). For extended insulating

[1]The angle between $\Gamma - X$=[100] and $\Gamma - W$=[1,0.5,0] equals 26.6°, only.

layers employed as tunnel barriers in MTT experiments we also have to revise our calculation of the tunneling emission cone. Since tunneling takes place not only on atomic terraces but also on atomic steps and other rough surface areas, conservation of $k_{||}$ is violated. Evidence is found that this leads to a much more relaxed (broader) tunneling emission cone compared to the point-like tunneling injection by an STM-tip [99]. However, hot electrons ballistically transported with a nonzero $k_{||}$-component are proportionately more attenuated since they have to pass a larger effective distance through the base layers until they reach the semiconductor interface. Let us estimate this influence on the determination of the attenuation length. To use the same transmission values of Fig.4.11 effective reduced thicknesses with $d_{\mathrm{eff}}^{\mathrm{FM2}} = d^{\mathrm{FM2}} \cos 36^\circ$ are deduced to account for a dominant non-perpendicular transport through the base towards the L-point and these results are fitted with the same procedure as mentioned above. In doing so, the majority spin attenuation length is artificially reduced by about 1 nm, while the minority spin attenuation length is altered by 0.1 nm, only[1]. Interestingly, the attenuation lengths in both studies nicely coincide with each other, as shown in Fig.4.12. It seems that differences in the revealed scattering lengths λ of Fig.4.12 originate from different substrates. At this point we can find no significant improvement in hot electron transport between MBE-grown $Fe_{34}Co_{66}$ and magnetron sputtered $Fe_{16}Co_{84}$ layers.

4.4.2.2 Attenuation length and electron energy

Obviously, $\lambda_{M(m)}$ does not vary strongly with increasing tunneling voltage for U=-1.3 up to -2 V, see Fig.4.11 in contrast to what we would expect from lifetime considerations. But we understand this result and also the strong spin dependence by recalling the mean free path Λ being the product of group velocity and electron lifetime

$$\Lambda(E) \quad = \quad v(E)\tau(E). \tag{4.16}$$

Both are functions of the electron energy, however, with an opposite slope. While $\tau(E)$ is reduced at larger energies due to the growing phase space, $v(E)$ is generally enhanced as reflected in steeper electronic bands with increasing energy. We will consider these competing effects in the following by using a simple model, which is based on ab-initio bandstructure calculations. In addition, we investigate whether the spin asymmetry arising from the most effective inelastic relaxation channel, i.e. electron-electron scattering, is already sufficient to explain the strong spin dependence of the attenuation lengths of Fig.4.11.

[1] Retrospectively considering dominant transport along $\Theta_{\max} = 12^\circ$ for our study respecting the impact of the dip of the tunneling emission cone around $k_{||} = 0$ would also change d^{FM2} to a value $d_{\mathrm{eff}}^{\mathrm{FM2}}$. However this variation is 2 % only and therefore neglected.

Electron scattering is treated within the golden rule approach described by formula 2.12. Since we focus on a relatively small energy interval, we assume the electron-electron scattering matrix element α to be constant and spin independent, because the density of states (DOS) and, thus, related effects undergo much stronger variations than α. For the sake of simplicity we further approximate the DOS for $E < E_F$ with a spin independent box like shape. In doing so, secondary electron excitation is naturally spin independent. The integrals, which we have to execute for determining the spin dependent hot electron lifetime $\tau_{\mathrm{e-e},M(m)}$, collapse therefore to an integral over the unoccupied part of the DOS according to

$$\tau^{-1}_{\mathrm{e-e,M(m)}} = A\frac{2\pi}{\hbar}\int_{E_F}^{E} dE'\,(1-f(E'))\,\rho_{M(m)}(E'), \tag{4.17}$$

while A is an overall scaling parameter reflecting the strength of secondary electron excitations and the impact of the matrix element α. A will be finally adjusted to fit the experimental data best. ρ and f are the momentum averaged density of states and the Fermi function. In a second step we multiply $\tau_{\mathrm{e-e},M(m)}$ with the k-resolved group velocity along [100], which we extract from a bandstructure calculation of bcc $Fe_{34}Co_{66}$. With this calculation performed for each electron energy we finally get the dependence of the energy dependent hot electron mean free path Λ, which we discuss thereafter with regard to the attenuation lengths λ of Fig.4.11.

In Fig.4.14 the momentum averaged spin resolved density of states and the spin resolved electronic bandstructure along [100] of bcc $Fe_{34}Co_{66}$ are shown. Both are calculated with density functional theory (DFT) and are supplied by Prof. Dr. H. Ebert [41]. Disorder within the alloy is manifested in electronic bands being broadened since the atoms can be arranged on different positions within the crystal unit cell. Obviously, the influence of disorder is much larger on the minority spin character. Very interestingly disorder mediated band broadening increases the elastic scattering rate for Fermi level electrons as reported in [129]. We can imagine that the same effect takes also place in the hot electron regime, where elastic and inelastic scattering may also be enhanced. As a consequence disordered alloys would naturally provide a new source of spin asymmetry for hot electron relaxation compared to elemental metals or ordered alloys. However, this statement remains hypothetic and has to be quantified in the future.

In order to reveal the group velocity, the electronic bands of Fig.4.14 are fitted by polynomial functions and differentiated with respect to the electron energy. Influences of spin orbit hybridization points are neglected in this consideration. Note that bands with Δ_5-symmetry are twofold degenerate so that we count them twice for obtaining the k-averaged electronic group velocity along [100]. From Fig.4.15(a) we recognize that minority spins are inherently slower than majority spins within a large energy interval, which in turn facilitates electron scattering of minority spin character. The visible kinks

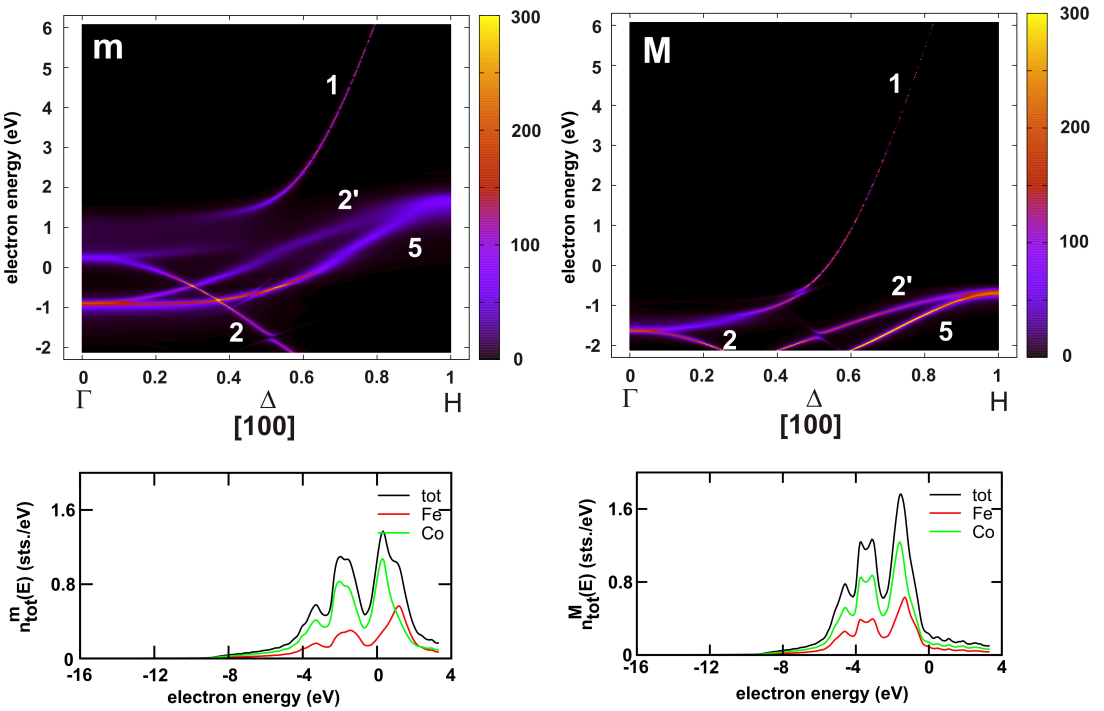

Figure 4.14: Density functional theory calculation using the Korringa-Kohn-Rostoker(KKR) method revealing the spin resolved DOS and the electronic bandstructure along the crystallographic [100]-direction of bcc $Fe_{34}Co_{66}$ [41]. Note that the spin character is not any more well defined by majority and minority spins due to spin orbit coupling. This effect is particularly visible at spin orbit hybridization points (spin hot spots) [129].

are a consequence of flat bands, which contribute velocities approaching zero. The integration of the unoccupied part of the density of states according to formula 4.17 is shown in Fig.4.15(b) revealing that the phase space for hot electron decay is always by far larger for minority than for majority spins. By dividing the graphs of Fig.4.15 we achieve a measure of the energy dependent mean free path MFP. Although we have adopted some approximations for this model the revealed spin dependent mean free paths reproduce reasonably well the bias voltage dependence and the spin dependence of the experimentally obtained attenuation lengths, see Fig.4.15(c). Certainly, there exists a difference between tunneling voltage and electron energy as well as between the attenuation length and mean free path. However, these discrepancies vanish for tunneling voltages approaching the Schottky barrier height and grow obviously only slowly with increasing absolute value of U. The coincidence of the graphs of Fig.4.15(c) strongly supports that the magnetocurrent effect of bcc $Fe_{34}Co_{66}$ films is mostly governed by the spin asymmetry of bulk electron-electron scattering and by the spin dependent electron

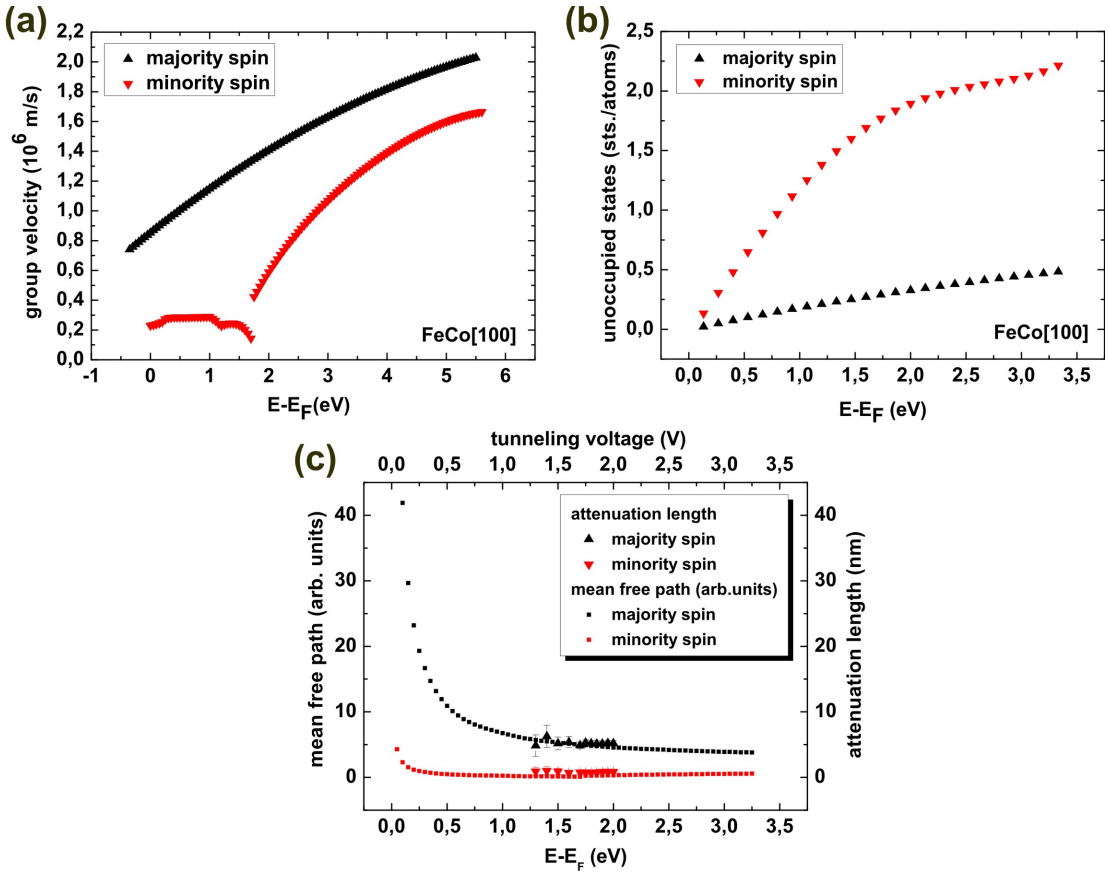

Figure 4.15: Spin resolved k-averaged group velocity along [100](a) and the spin dependent integrated density of states of bcc $Fe_{34}Co_{66}$(b) at room temperature. Mean free path along [100] as calculated from (a) and (b) and attenuation length of bcc $Fe_{34}Co_{66}$ (c).

group velocities within the electron energy interval of 1.3 up to 2 eV above E_F, rather than by magnon or phonon mediated relaxation processes.

4.5 Hot electron transport in fcc Au

From another wedge layer study varying the thickness of the Au capping layer we extract the scattering length of fcc Au at room temperature. The samples employed in this study consist of spin valve layer stacks of 2.9 nm $Fe_{34}Co_{66}$/12.5 nm Au/ 2.9 nm $Fe_{34}Co_{66}$/ d_{cap} Au as verified by an cross sectional TEM investigation. d_{cap} denotes the variable thickness used for the thickness dependent study. Several (some hundred up to thousand) I_CU-spectra in parallel and antiparallel magnetization configuration randomly distributed over the surface are obtained on each sample.

The I_CU-spectra reflect hot electron transport along the vicinity of the [100]-axis of

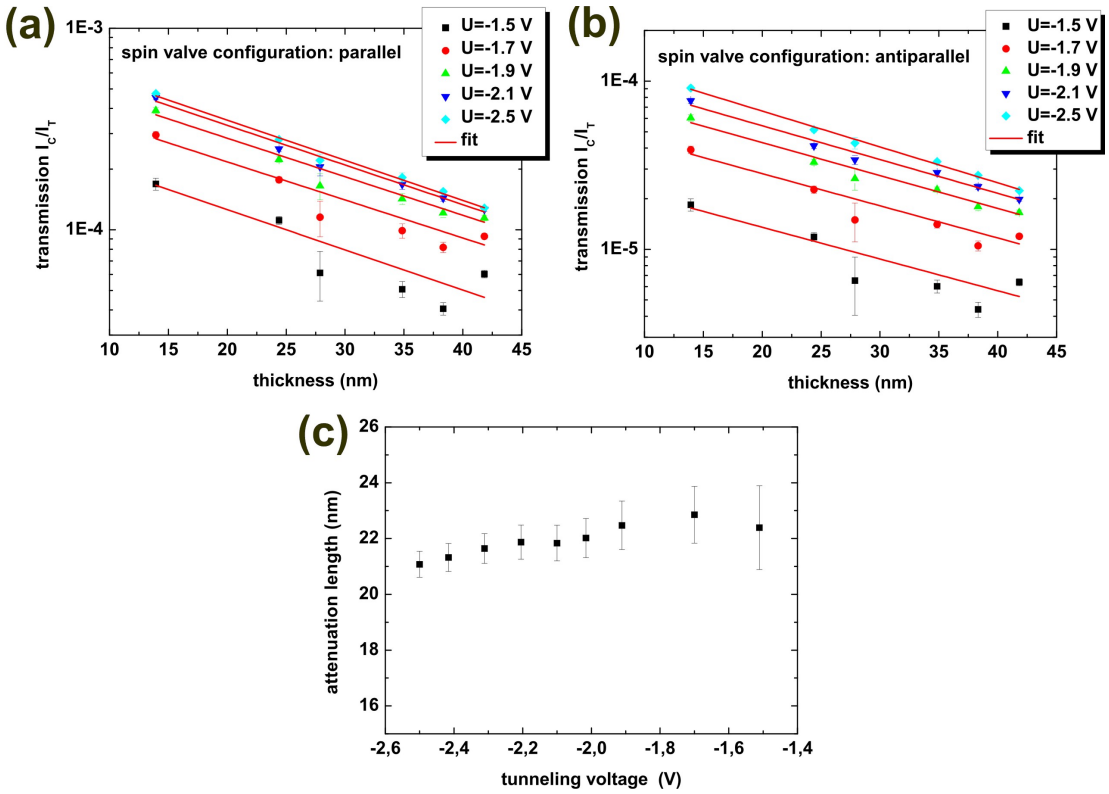

Figure 4.16: Transmission in parallel (a) and antiparallel (b) magnetization configuration for various bias voltages. The solid lines are exponential fits to the data revealing the attenuation length of fcc Au (c).

the fcc lattice. Hot electron transmission follows an exponential decay with increasing thickness and is independent of the magnetization configuration of the spin valve, see Fig.4.16(a) and (b). The extracted value of the attenuation λ accompanied by its bias voltage dependence is shown in Fig.4.16(c). λ is slightly reduced with increasing U and shows an average value of 21.9±0.6 nm within the measured energy interval of 1.5 up to 2.5 eV above the Fermi level. This value is almost the half of the mean free path of Fermi-electrons, which equals 38 nm [130] at room temperature. Hence, the noble metal gold is several times more transmissive for hot electrons than the $Fe_{34}Co_{66}$-alloy, which we attribute to the lack of unoccupied d-like states above E_F for Au.

The relatively weak dependence of λ on the tunneling voltage has to be once more attributed to the competing influence of the electronic lifetime and electron velocity. If we compare the attenuation length of this work to other BEEM studies in the literature shown in table 4.1, it becomes once more clear that the attenuation length λ is apparently not a material parameter, only. The strong variations can only be explained by different substrates [132], which distinctly select the electron paths through the base

Table 4.1: Hot electron attenuation lengths of thin gold films

λ (nm)	substrate	voltage (V)	temperature (K)	Ref.
13	Si(111)	-1.2	77	[40]
13.3±2	Si(100)	-1.2	293	[131]
14.7±0.6	Si(100)	-1.2	77	[131]
27.6	Si(111)	-1.2	293	[45]
26.5	Si(100)	-1.2	293	[45]
11.9±2.4	Si(111)	-1.2	80	[132]
13.4±2.7	Si(100)	-1.2	80	[132]
1.6±0.1	GaAs(100)	-1.2	80	[132]
21.9±0.6	$GaAs_{67}P_{33}$(100)	-1.5...-2.5	293	this work

and by inequalities in the crystalline quality of the Au-overlayer, which creates a distinct elastic contribution λ_{el} to λ. The revealed attenuation length of Fig.4.16(c) exceeding 20 nm is among the largest ever measured and comes closest to the values revealed by reference [45]. Interestingly, these authors claim they have investigated hot electron transport through single crystalline gold grains of (111) orientation. This strongly supports that epitaxial lattices of Au are privileged for hot electron transmission than polycrystalline lattices.

4.6 Temperature dependence of hot electron transport

By replacing one of the bcc $Fe_{34}Co_{66}$ films of the spin valves with an epitaxially grown Fe layer we aim for revealing correlations between hot electron transport and the electronic bandstructure of these materials. When iron becomes alloyed with cobalt, E_F shifts to larger energies and, thus, the phase space available for hot electron decay is very different for $Fe_{34}Co_{66}$ and Fe. To expose such bandstructure effects the sample temperature is successively reduced to freeze out the distorting influences of thermally excited magnons and phonons. Since temperature dependent studies are relative time-consuming due to a large amount of characteristics (about 15.000 characteristics per sample) which are to be recorded, we investigate only one spin valve stack for each of these materials.

4.6.1 Hot electron transport in $Fe_{34}Co_{66}$/Au/$Fe_{34}Co_{66}$ spin valves

The first base layer stack under investigation consists of 2.9 nm $Fe_{34}Co_{66}$/ 10.8 nm Au/ 5 nm $Fe_{34}Co_{66}$/18.7 nm Au. Obtained hysteresis loops exhibit a rectangular shape for sample temperatures between 85 K and room temperature provided the magnetic field

is swept along the magnetic easy [110]-axis. We can thus state that for all temperatures only the desired collinear spin valve configurations are accessible and perfect measurement conditions persist from a magnetic point of view.

When the sample temperature is reduced, we observe a negative and positive temperature coefficient for I_C depending on the tunneling voltage, see Fig.4.17. For most of the bias voltages used I_C monotonically increases while the opposite holds near the threshold region of Φ_{SB} as a result of lowering the temperature. We ascribe the latter of these two effects to the slight temperature dependence of the energy gap E_g of the semiconductor. By this means the Schottky barrier height shifts by the order of 10 meV to larger values [133]. On the other hand the increase in hot electron transmission at low temperatures is a result of the reduction of scattering partners (phonons and magnons) in the base but also in the semiconductor. Once hot electrons have entered the collector they may be backscattered into the base layers while the needed momentum exchange is provided by phonons of the semiconductor. Interestingly, the temperature sensitivity is much stronger when the two magnetization vectors are aligned parallel than antiparallel, see Fig.4.17(a) and (b). I_C becomes, for instance, almost doubled at $U = -2.5\,\mathrm{V}$ but the increase is about one third only upon cooling the sample from 293 to 85 K. However, this result comes not as a surprise. Although phonon and magnon mediated electron relaxation processes are suppressed, other temperature independent processes are not varied. Electron-electron scattering affects more effectively minority spin electron transport yielding $\tau_M > \tau_m$. This inequality is further strengthened by generally slower electron velocities for minority spin electrons. Hence these two temperature independent factors are more pronounced in the antiparallel magnetization configuration, where transport is more governed by minority spin hot electrons compared to the parallel magnetization configuration.

Small features of the I_CU-characteristics can be best analyzed by calculating their derivative, see Fig.4.17(c). The minimum in the resulting dI_C/dU-characteristic reveals an inflection point U_I in the I_CU-spectra at $U_\mathrm{I} - 1.6\,\mathrm{V}$ and $-1.8\,\mathrm{V}$ for parallel and antiparallel magnetization configuration, respectively. The inflection point is remarkably insensitive on temperature variations and therefore not related to thermal excitations. For bias voltages larger than U_I the ballistic currents measured in I_C grow slower and merge towards a saturation level U_Sat. Quite the contrary, U_Sat shows a significant temperature dependence and shifts towards larger voltages at lower temperatures, which becomes evident when we extrapolate the dI_C/dU-characteristic beyond $U = -2.5\,\mathrm{V}$ and focus on the interception point with the zero line. Consequently, the inflection point and the saturation of I_C are independent features or not tightly related to each other.

The occurrence of the inflection point may be ascribed to different reasons, like the growing suppression of perpendicular ballistic hot electron transport with increasing

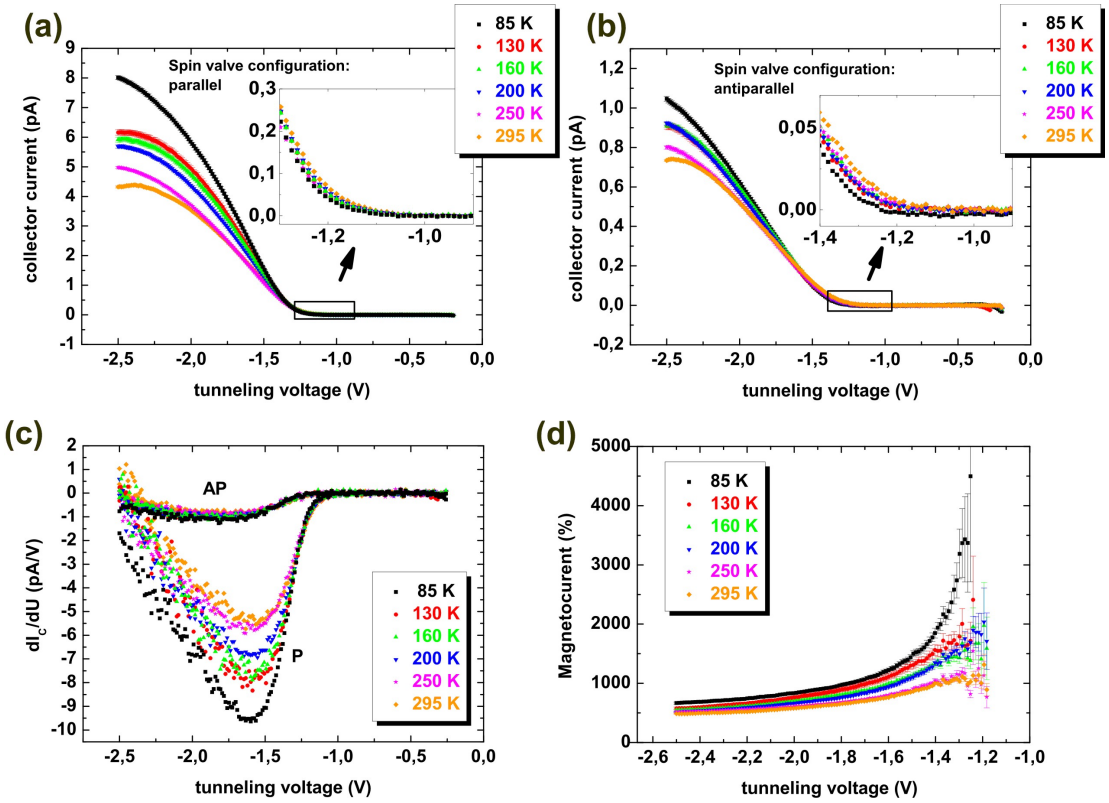

Figure 4.17: Temperature dependence of hot electron transport through $Fe_{34}Co_{66}$/Au/ $Fe_{34}Co_{66}$ spin valves. I_CU-characteristics for parallel (a) and antiparallel (b) magnetization configuration accompanied by their first derivative (c). The resulting magnetocurrent as calculated from (a) and (b) is shown in (d). Data obtained with $I_T = 20\,\mathrm{nA}$.

tunneling voltage by the gold energy gap around $\overline{\Gamma}$. Furthermore, the larger the injection voltage U the smaller is the increment in hot electron transmission when increasing U. This statement is a consequence of the low energetic tail of the hot electron tunneling distribution overlapping with the energy interval $[eU, \Phi_{SB}]$ for hot electron transmission across the metal/semiconductor interface. The occurrence of a saturation of I_C, on the other hand, is explained differently in the literature [95]. The growth of phase space for hot electron transmission into the semiconductor is compensated by the scattering efficiency in the base and the collector, which is enhanced at larger bias voltages. This view is supported by Fig.4.17(c) since a reduction of the population of potential scattering partners (i.e. thermal phonons and magnons) shifts this saturation point to larger tunneling voltages or electron energies.

Phonon and magnon induced effects in hot electron transport can be distinguished due to their opposite temperature dependence in spin contrast. Thermally excited magnons intermix the spin transport channels or they act as outscatterer predominantly for ma-

jority spin hot electrons due to phase space arguments. In this way, the presence of magnons diminishes spin contrast. On the other hand, phonons provide a spin conserving Coulomb type hot electron relaxation very similar to electron-electron scattering. The presence of phonons enhances minority spin relaxation due to phase space arguments and would increase the magnetocurrent. In Fig.4.17(d) the temperature dependence of the magnetocurrent of the investigated $Fe_{34}Co_{66}/Au/Fe_{34}Co_{66}$ spin valve is shown. Spin contrast is monotonically reduced the larger the sample temperature is. This observation can only be attributed to the impact of thermal magnons, because phonons provide the opposite tendency for hot electron relaxation. For a sample temperature of $T = 85\,\mathrm{K}$ MC values between 670 % at $U = -2.5\,\mathrm{V}$ and reliably larger than 3000 % at lower bias voltages of $U = -1.25\,\mathrm{V}$ are identifiable[1]. The strong change of the MC from 1200 to 3000 % for $U = -1.2\,\mathrm{V}$ upon variations of the temperature is counterintuitive. In terms of hot electron spin polarization this change is of a single percent, only. On the contrary, a variation of the magnetocurrent between 100 and 400 % is caused by a much stronger variation of P, see also Fig.4.10. The bias dependence of MC shows a monotonic decay with increasing tunneling voltage Fig.4.17(d) for all temperatures. This is mainly a result of non-ballistic electrons contributing to I_C as already discussed in the last paragraph.

Fig.4.18(a) shows the temperature dependence of the magnetocurrent for some voltages U demonstrating again the monotonic temperature behavior. According to fundamental thermodynamics phonon and magnon populations scale with the temperature via power laws, which is manifested in similar scalings of $\Gamma_{\mathrm{e-ph}}$ and $\Gamma_{\mathrm{e-m}}$. Since $T_i^{M(m)}$ is an exponential law of λ and influences P via $P = \frac{T^M - T^m}{T^M + T^m}$ and MC via $\mathrm{MC} = \frac{2P_1P_2}{1-P_1P_2}$, we do not expect a simple power law for the dependence $\mathrm{MC} = \mathrm{MC}(T)$.

We proceed by plotting the temperature sensitivity of MC and $I_C^{P(AP)}$, i.e. the temperature dependence normalized to the data at room temperature via $(\mathrm{MC}(U,T) - \mathrm{MC}(U,293\,\mathrm{K}))/\mathrm{MC}(U,293\,\mathrm{K})$ and $(I_C^{P(AP)}(U,T) - I_C^{P(AP)}(U,293\,\mathrm{K}))/(I_C^{P(AP)}(U,293\,\mathrm{K}))$, see Fig.4.18(b-d). Fig.4.18(c) and (d) unambiguously demonstrates that the temperature dependence of I_C depends on the emitter voltage U. While for voltages only slightly larger than Φ_{SB} I_C is varied due to the variation of the energy gap of the semiconducting collector, I_C is enhanced at larger tunneling voltages due to the reduction of magnons and phonons. The more negative the bias voltage the stronger the change of I_C upon temperature variations. Interestingly, the temperature sensitivity is reversed for the magnetocurrent, see Fig.4.18(b). Changes are largest for $U \approx \Phi_{SB}$. However, the interpretation of characteristics of the magnetocurrent MC are somehow counterintuitive as highlighted above due to the definition $\mathrm{MC} = \mathrm{MC}(P_1, P_2)$. A large change

[1] The largest magnetocurrent of 3400 % reported so far has been obtained on a MTT-device using 5 nm $Co_{70}Fe_{30}$/ 4 nm Cu/ 5 nm $Ni_{81}Fe_{19}$ spin valves with n-GaAs collectors at T=77 K [26].

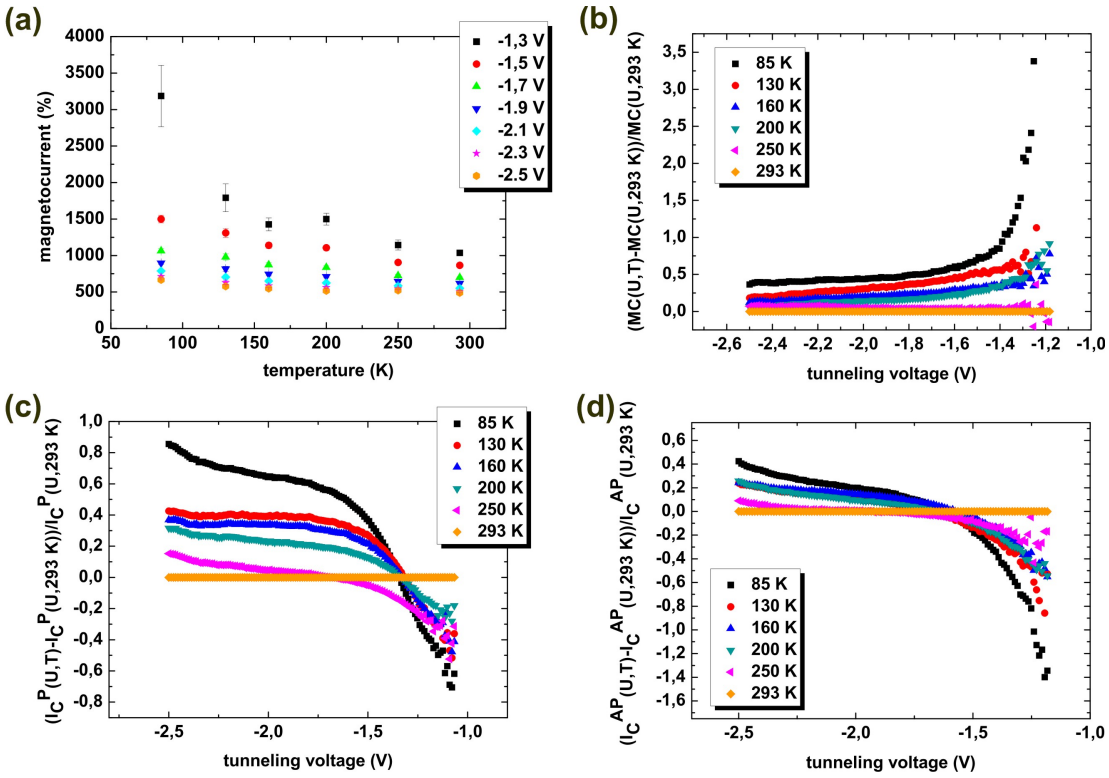

Figure 4.18: Magnetocurrent as function of sample temperature (a). Temperature dependence of $I_C^{P(AP)}$ and MC normalized to room temperature values (b-d). Data obtained with $I_T = 20\,\mathrm{nA}$.

of the quantity MC does not automatically imply a large variation of hot electron spin polarization.

So let us focus on the normalized temperature dependence of I_C of Fig.4.18(c) and (d) again, where obviously the temperature sensitivity nonlinearly grows with U. This observation cannot be explained by the energy dependence of electron-phonon and electron-magnon scattering since $\Gamma_{\mathrm{e-ph}}$ and $\Gamma_{\mathrm{e-m}}$ saturate in the deep hot electron regime relevant here. It is, moreover, a consequence of the temperature dependent shape of the $I_C U$-characteristics. This effect is not only impressed by the temperature dependence of the Schottky barrier height but also of the saturation point U_{Sat} reflecting the variation of scattering partners with temperature. In this context we cannot distinguish between phonon mediated scattering within the base or hot electron backscattering in the semiconducting collector. Once electrons have overcome the Schottky barrier, they either relax to E_F and remain within the collector or they are backscattered into the base layers. Temperature dependent backscattering influencing the observed value of I_C arises by electron relaxation with phonons of the semiconducting collector. This interpretation is strongly supported by BEEM studies on Au/Si(100). The authors report

attenuation lengths of Au being only slightly temperature dependent although ballistic currents are almost doubled when cooling down from room temperature to 77 K [131]. Electrons of larger energy may experience multiple phonon mediated relaxation mechanisms before they are trapped within the semiconductor and are not any more able to overcome the Schottky barrier in the backward direction. Within this point of view we cannot unambiguously ascribe the bias and temperature dependencies of U_{Sat} to properties of the base layers or of the collector. This question can be answered by a thickness dependent study carried out at various sample temperatures.

4.6.2 Hot electron transport in Fe/Au/$Fe_{34}Co_{66}$ spin valves

4.6.2.1 Crystallinity and magnetism

One of the $Fe_{34}Co_{66}$-films is now substituted by a bcc Fe-film in order to highlight the discrepancies in hot electron transport between these two material. From literature we know that bcc Fe-films have almost the same lattice constant as $Fe_{34}Co_{66}$-films (0.2835 nm and 0.2858 nm) and that they grow on GaAs(100)-substrates with the structure bcc Fe(100)<010> || GaAs(100)<010>[134]. One can expect therefore a single crystalline growth of Fe/Au/$Fe_{34}Co_{66}$ spin valve stacks onto n-$GaAs_{67}P_{33}$(100), as well.

For reaching the desired collinear magnetization configurations we have to pay attention to the layer thicknesses. Two magnetic easy axes along the [100]- and [010]-direction are provided by the magnetocrystalline anisotropy of bcc Fe for film thicknesses exceeding 7 monolayers ($\approx$ 1 nm). When iron is grown onto (100)-oriented GaAs substrates, an additional uniaxial interface anisotropy arises favoring the magnetic easy axis to be aligned with the [110]-axis of GaAs[135, 136]. The competition in selection of the magnetic easy axis of these two anisotropies leads to an in-plane spin reorientation transition when the iron film thickness is successively increased. Yet, this is not the case for equally thick bcc $Fe_{34}Co_{66}$ films on GaAs(100), where the magnetic easy axis is favored by both magnetic properties to be aligned along the [110]-axis, see [137]. So for this study we chose Fe to be directly grown onto $GaAs_{67}P_{33}$(100) in combination with a bcc $Fe_{34}Co_{66}$ film as FM2-layer. Provided Fe is grown sufficiently thin but also not thinner as 7 monolayers we benefit from the dominance of the uniaxial interface magnetic anisotropy and end up in two parallelly aligned magnetic easy axes of the two ferromagnetic films along the [110]-direction of the substrate.

Let us start this investigation by checking for the layer thicknesses as well as for the crystalline structure. The base layer stack employed in this study consists of an epitaxial 4.4 nm bcc Fe/ 9.7 nm fcc Au/ 9.1 nm bcc $Fe_{34}Co_{66}$/fcc 16.5 nm Au layer stack as verified by cross-sectional TEM, see Fig.4.19. Although the crystalline structure is not visible

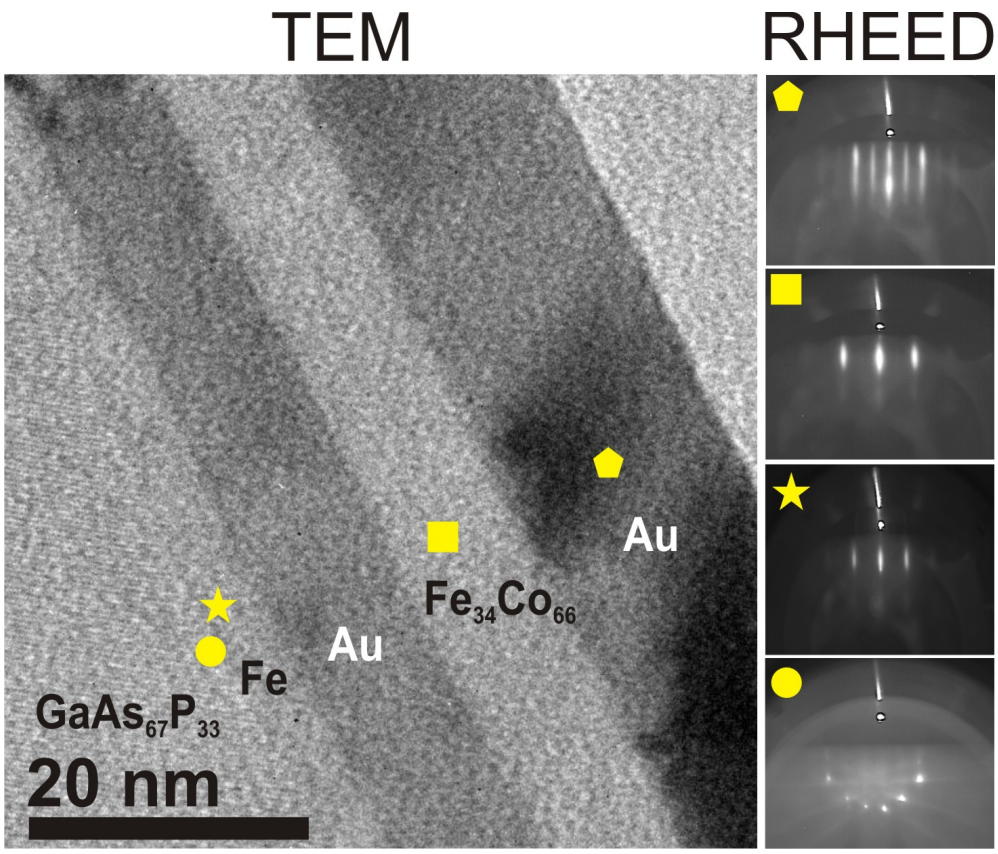

Figure 4.19: Cross sectional TEM combined with electron diffraction during layer deposition (RHEED) clearly demonstrates the single crystalline growth of the base layers

in the TEM-image, electron diffraction during during the metal deposition (RHEED) evidences the complete single crystalline growth of the spin valve stack, see Fig.4.19.

Next we focus on the magnetic response of this spin valve. The magnetization reversal is recorded by using MOKE at room temperature and BEEM at room and low temperatures. Since macroscopic and microscopic length scales are probed by these techniques, we also obtain information about the homogeneity of the reversal process. In Fig.4.20(a-d) the most interesting room temperature hysteresis loops are shown. Both techniques reveal rectangular shaped hysteresis loops with 100 % remanent magnetization when the external field is swept along the substrates [110]-axis, see Fig.4.20(a-b). Only domain wall nucleation and motion are significant while spin rotation processes contribute obviously only negligibly. The lack of any spin rotation processes between saturation and remanence evidences the existence of a local energy minimum for $\mathbf{M}||[110]$ at all external fields applied. In this way, the two magnetization vectors are able to switch only by 180° and we conclude that the desired collinear magnetization configurations of the spin valve are exclusively achievable. Further, we assert again that the lower coer-

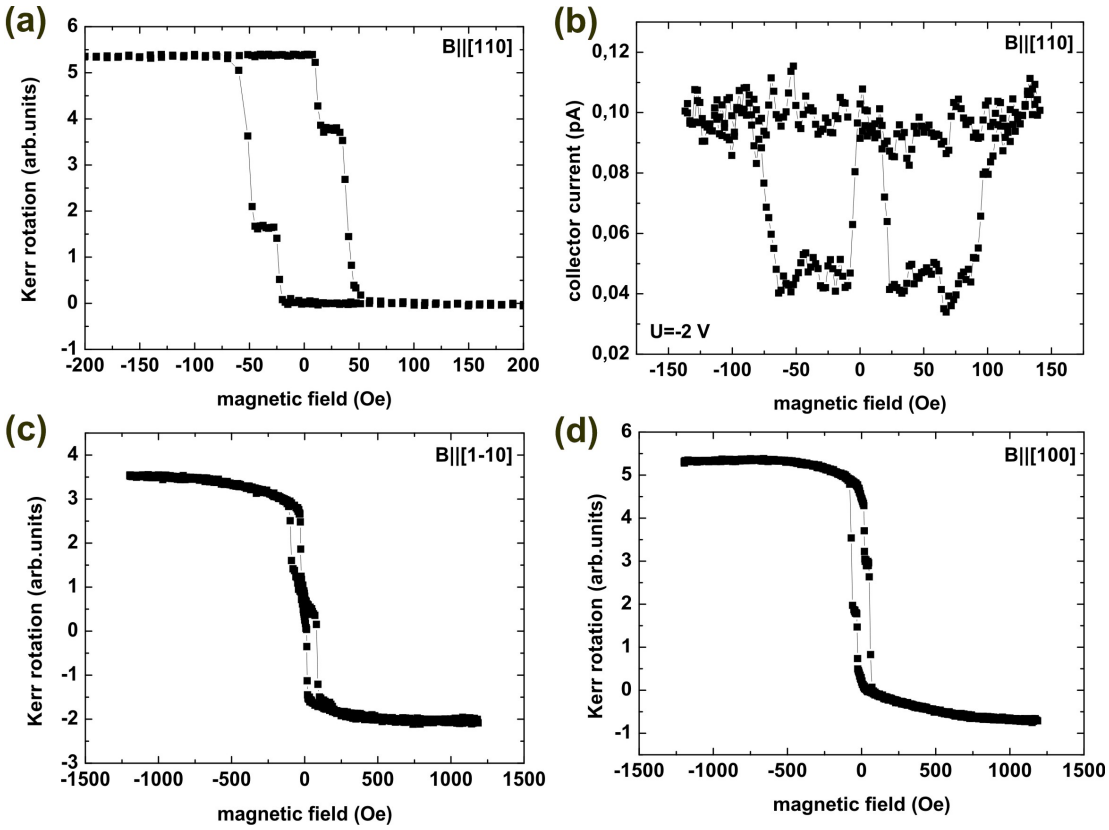

Figure 4.20: Room temperature hysteresis loops obtained by sweeping a magnetic field along the [110]- (a,b), [1-10]- (c) and [100]-axis (d) of the substrate using MOKE (a,c,d) and BEEM (b). Data obtained with $I_T = 20\,\mathrm{nA}$.

cive field belongs to the more buried bcc Fe layer. The saturation magnetizations of Fe and $Fe_{34}Co_{66}$ are relatively equal ($4\pi M_s = 22$ and 24 kOe) and the two ferromagnetic layers are of very different film thicknesses.

When the field is swept along other axes of high symmetry of the ferromagnetic lattice, hysteresis loops of very similar shape as for $Fe_{34}Co_{66}$/Au/$Fe_{34}Co_{66}$ spin valves are observed, which indicates that the underlying magnetization processes are very similar, see Fig.4.20(c) and (d).

Although room temperature magnetometery provides clear evidence for the collinear magnetization configurations, this is not any more the case for lower sample temperatures. Moreover, a more complex and even inhomogeneous magnetization reversal appears. By keeping the sweeping field oriented along [110] and cooling the sample from room temperature to 130 K, rectangularly shaped loops can be still observed with BEEM, however, not any more for all STM-tip positions on the surface. Partly curved characteristics can be recorded as well revealing an inhomogeneous magnetic response

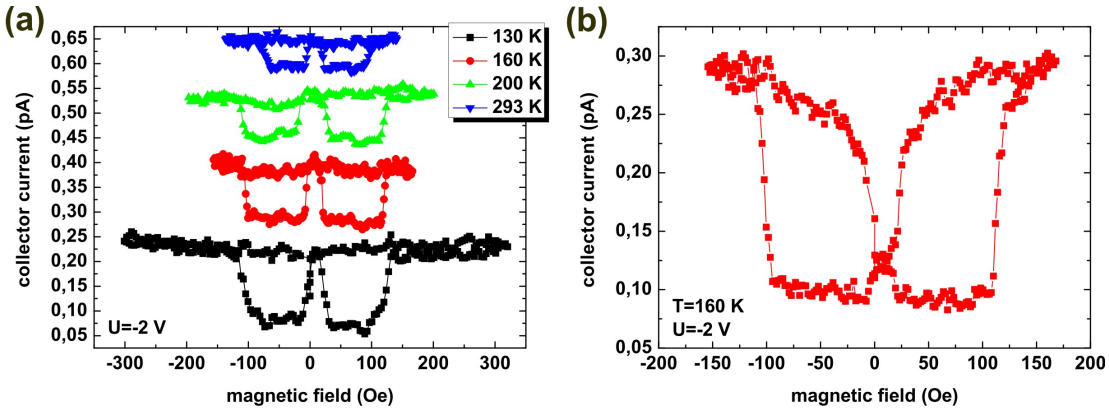

Figure 4.21: Local hysteresis loops obtained at various sample temperatures using BEEM (a). For sake of clarity the loops are shifted with respect to each other. Two types of hysteresis loops can be obtained for sample temperatures of $T \leq 160\,\mathrm{K}$ revealing an inhomogeneous magnetization reversal (b). Data obtained with $I_T = 20\,\mathrm{nA}$.

of the spin valve and highlighting the growing influence of spin rotation processes, see Fig.4.21(a) and (b). In addition, the absence of 100 % remanence in Fig.4.21(b) demonstrates that an antiparallel magnetization alignment is not any more readily available. Although the curved hysteresis of Fig.4.21(b) fades to a broad plateau at $H \approx \pm 20\,\mathrm{Oe}$ defining $I_C^{\min}$, this value not necessarily resembles I_C^{AP}. From the anisotropy considerations mentioned above we can assess an upper limit for the deviation from antiparallel alignment. We know that the two magnetic easy axes of both ferromagnetic layers may deviate by a maximum of 45° so that $I_C^{\min}$ corresponds to a relative angle between the two magnetic moments of between 135° and 180°. The resulting hot electron characteristics may have therefore an additional magnetic contribution. In order to respect this result, we substitute I_C^{AP} by $I_C^{\min}$ and MC by MC* for all low temperature data of this spin valve as a precaution. Note that, I_C^P is still accessible by recording I_C at sufficiently large magnetic fields.

4.6.2.2 Hot electron transport

$I_C U$-spectra are recorded at $H > 250\,\mathrm{Oe}$ and $H \approx 40\,\mathrm{Oe}$ to determine I_C^P and $I_C^{AP}(I_C^{\min})$, see Fig.4.22(a) and (b). Compared to $Fe_{34}Co_{66}/Au/Fe_{34}Co_{66}$ spin valves they are very different in shape. The replacement of one of the $Fe_{34}Co_{66}$-layers with a bcc Fe film causes a kink-like feature to appear at $U_K = -1.8\,\mathrm{V}$. I_C is increased when the tunneling voltage exceeds this value, an effect, which can be explained by opening an additional conduction channel for hot electrons or by the omission of a relaxation channel.

The very low ballistic currents of less than 0.15 pA at T=293 K can be attributed to the thicker base layers and to the increased number of now three different materials intro-

duced into the base so that ballistic hot electron transport is more subject to interface attenuation due to bandstructure mismatches. Once more, I_C becomes monotonically enhanced for all investigated magnetization configurations when the sample temperature is lowered but not until the tunneling voltage exceeds the kink-value of U_{K}. Below this threshold voltage I_C is even slightly reduced when the sample is cooled from room temperature to 200 K. But by continuing the cooling procedure a positive temperature dependence of I_C remains for all tunneling voltages measured.

One of the most conspicuous differences of the two types of spin valves is the very distinct temperature dependence. The increase of I_C in Fig.4.22(a) and (b) is about a factor of 4 at $U = -2.5\,\mathrm{V}$ upon cooling from 293 K to 130 K and approximately equally strong for the other magnetization configurations studied. This behavior strongly suggests that either temperature independent contributions (electron-electron scattering and group velocity contributions) to the spin asymmetry of hot electron relaxation are much less effective or temperature dependent influences (thermal phonons and magnons) are stronger in bcc Fe than in bcc $Fe_{34}Co_{66}$.

The kink-feature of the I_CU-spectra becomes more visible when we calculate their first derivative, see Fig.4.22(c). Furthermore, two inflection points at $U_{\mathrm{I1}} = -1.6\,\mathrm{V}$ and $U_{\mathrm{I2}} = -2.1\,\mathrm{V}$ appearing as minima in the first derivative are revealed within the I_CU-spectra. All observed extremes are, though more or less pronounced, observable for all studied temperatures at the same values of U indicating that these are not only related to thermal excitations. Another feature, which is common for both types of spin valves, is the temperature dependence of the I_C-saturation at large tunneling voltages U_{Sat} supporting the explanation we have already found for the $Fe_{34}Co_{66}/Au/Fe_{34}Co_{66}$ spin valve study. This level shifts towards larger tunneling voltages when reducing the sample temperature and is visible by extrapolating the dI_C/dU-characteristics of Fig.4.22(c) towards the crossing with the zero line.

Let us proceed to calculate the (effective) magnetocurrent from the data of Fig.4.22(a) and (b) in order to highlight the second conspicuous difference of both spin valve types. In Fig.4.22(d) all revealed values for MC are well below 200 % and therefore about 6 times lower than for the $Fe_{34}Co_{66}/Au/Fe_{34}Co_{66}$ spin valve although ferromagnetic layer thicknesses are larger for the current study. By focusing on the bias voltage dependence we find again the monotonic tendency, which we have already addressed above. But the temperature dependence of Fig.4.22(d) exhibits a magnetic contribution and cannot be solely interpreted in terms of electron transport. When the sample temperature is lowered Fig.4.22(d) demonstrates suppressed values of spin contrast, which is most likely due to a growing misalignment of the magnetic moments of the ferromagnetic layers.

Some of the features mentioned above stand out more significantly when the data is

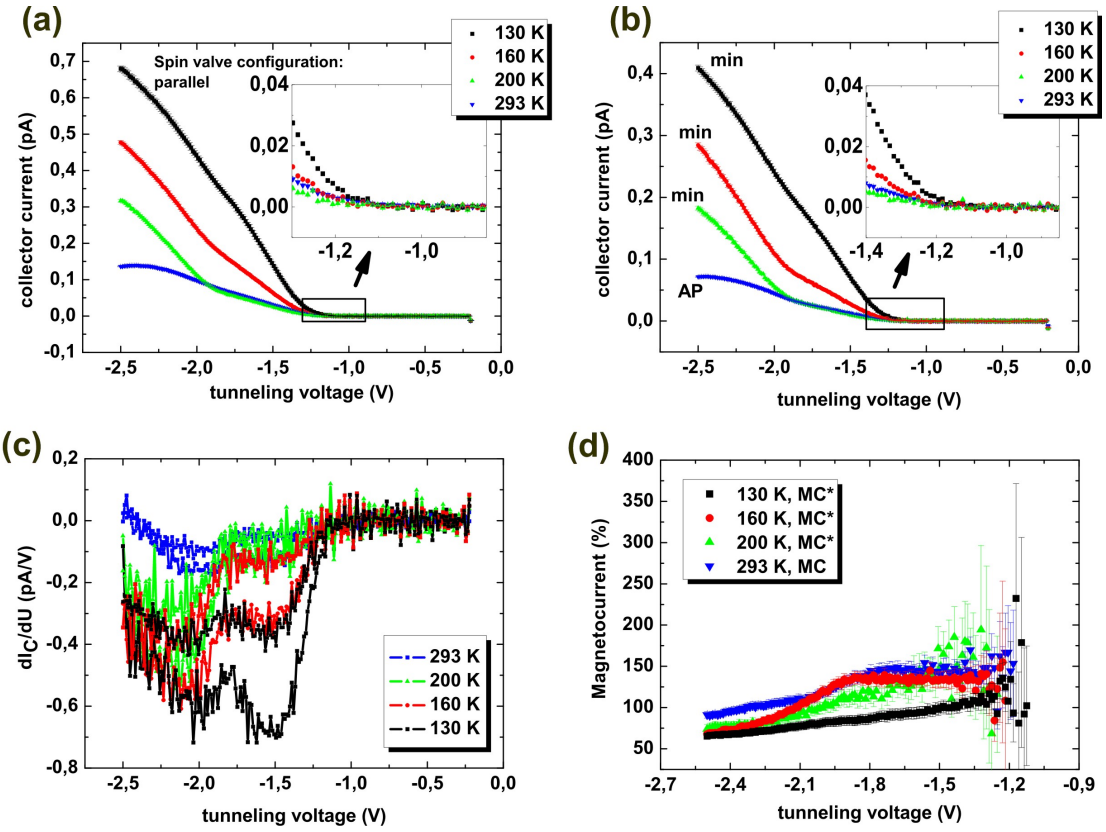

Figure 4.22: Temperature dependence of hot electron transport through epitaxial Fe/Au/$Fe_{34}Co_{66}$ spin valves. I_CU-characteristics for parallel magnetization configuration of the spin valve are shown in (a). A perfect antiparallel configuration is only accessible at room temperature, while at lower temperatures the magnetization vectors are opposed to each other drawing an angle smaller than 180° (b). The first derivative of these curves is plotted in (c). The resulting magnetocurrent as calculated from (a) and (b) is shown in (d). Data obtained with $I_T = 20\,\mathrm{nA}$.

normalized to the room temperature values. For instance, the tendency of a suppression of ballistic currents for $U \simeq \Phi_{SB}$ is clearly visible in Fig.4.23 for T=300 and 160 K, which we attribute again to the slight temperature dependence of the Schottky barrier height. At T=130 K this effect is not any more apparent and becomes obviously overwhelmed by the enhanced transmissivity of hot electrons at reduced temperatures. Furthermore, the kink observed at $U_\mathrm{K} = -1.8\,\mathrm{V}$ in the I_CU-characteristics is also reflected in Fig.4.23 as a more or less broad feature.

Yet we lack any microscopic explanation for the kink feature and the reduced spin contrast. With the same model we have utilized for understanding the energy dependence of the attenuation lengths we can check for the influence of group velocity effects and electron-electron scattering in bcc Fe. For this purpose we execute once more the

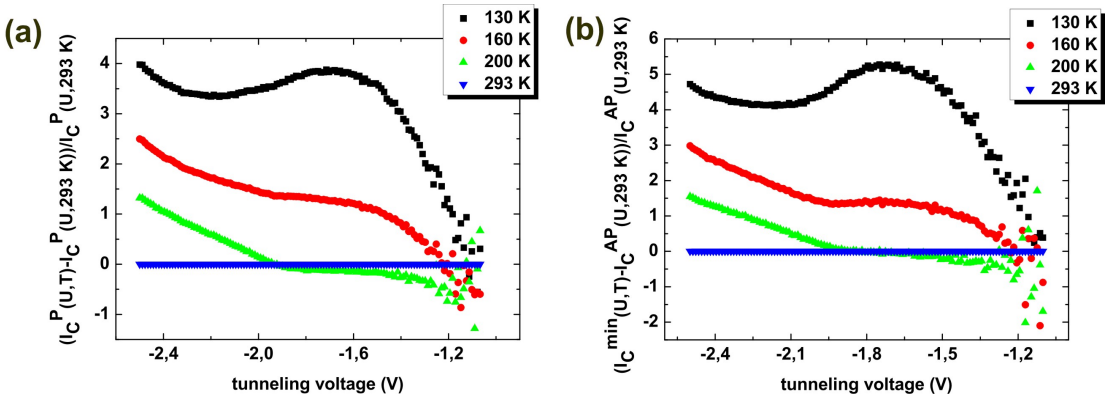

Figure 4.23: Temperature dependence of I_C^P and $I_C^{\min}$ normalized to the room temperature values. Data obtained with $I_T = 20\,\mathrm{nA}$.

integral

$$\begin{aligned} \Lambda_{\mathrm{e-e},M(m)} &= v_{M(m)}\tau_{\mathrm{e-e},M(m)} \\ &= v_{M(m)} \Big/ \left[A\frac{2\pi}{\hbar} \int_{E_F}^{E} dE' \left(1 - f(E')\right) \rho_{M(m)}(E') \right] \end{aligned} \tag{4.18}$$

in order to get a measure for the spin dependent hot electron mean free path $\Lambda_{\mathrm{e-e},M(m)}$. Recall that $\rho_{M(m)}$ is the spin resolved density of states and $v_{M(m)}$ the spin dependent group velocity along the Γ-H direction. A denotes an overall scaling factor, which we assume to be the same for bcc Fe and bcc $Fe_{34}Co_{66}$. It reflects secondary electron contributions and the impact of the matrix element. The needed density of states data as well as the bandstructure of bcc Fe is obtained via an ab-initio density functional calculation and supplied by Prof.Dr. H. Ebert [41], see Fig.4.24. The required values for $v_{M(m)}$ are extracted from the first derivative of the electronic bandstructure along the perpendicular [100]-axis and averaged, thereafter, for each electron energy. Please note again that the Δ_5-band is counted twice to respect its twofold degeneracy and that the impact of spin orbit hybridization points is neglected.

Minority spin hot electron in bcc Fe are inherently slower during their ballistic transport and experience a much larger phase space for inelastic electron-electron decay processes than their spin counterpart as we notice from from Fig.4.25(a) and (b). In comparison to bcc $Fe_{34}Co_{66}$ the spin asymmetry of the phase space for electron relaxation is smaller in bcc Fe. There are more unoccupied d-like states for both spin species available. However, the spin asymmetry of the group velocity is larger for some electron energies for Fe-films, which partly compensates the former loss of spin dependency. Since the integration of formula 4.18 is defined except for an overall scaling factor, we show the ratio of the revealed spin dependent mean free paths in Fig.4.25(c). Poles at certain values of U are a consequence of flat (minority spin) bands leading to group velocities

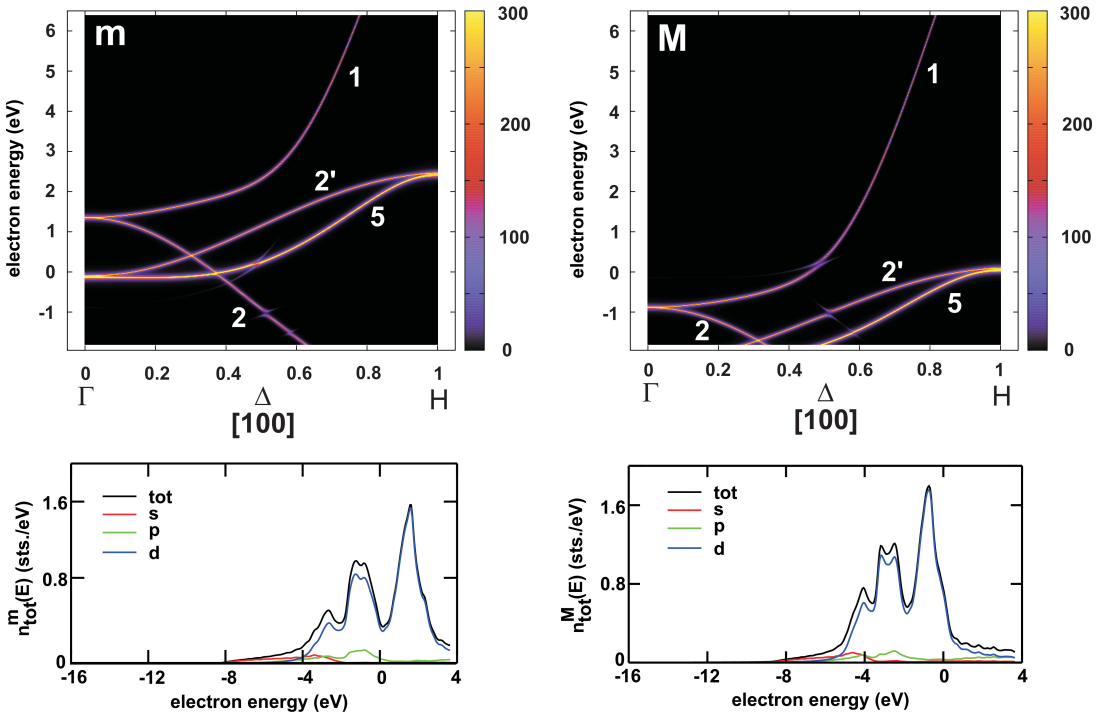

Figure 4.24: Density functional theory calculation using the Korringa-Kohn-Rostoker(KKR) method revealing the spin resolved DOS and electronic bandstructure along the crystallographic [100]-direction for bcc Fe [129].

approaching zero. According to this model we can expect a significantly reduced spin contrast in ballistic hot electron transport when one $Fe_{34}Co_{66}$-film is replaced by an equally thick Fe-film provided the relevant electron energies are below 1.9 eV above E_F. Though these results explain partly the lower spin contrast of bcc Fe, they lack an interpretation of the temperature dependence and the kink-feature of the I_CU-spectra.

So we have to aim for another interpretation. The strong temperature dependence and the reduced spin contrast in the Fe-film direct our attention to the interaction of hot electrons with thermally excited spin waves. For this, we show in Fig.4.25(d) the magnonic DOS of both materials as calculated by another ab-initio method (data supplied by Dr. L.Sandratskii [138]). We recognize a different evolution of both graphs in particular at low energies. The magnonic system is more populated in Fe than in $Fe_{34}Co_{66}$-films. At room temperature ($k_BT = 25$ meV) we can extract a difference in population of more than factor of 4, which implies that hot electrons are accordingly more subject to spin flip scattering processes in Fe than in $Fe_{34}Co_{66}$. This interpretation is in agreement with the low magnetocurrent values observed for all tunneling voltages of Fig.4.22(d) and also provides an explanation of the relatively strong temperature

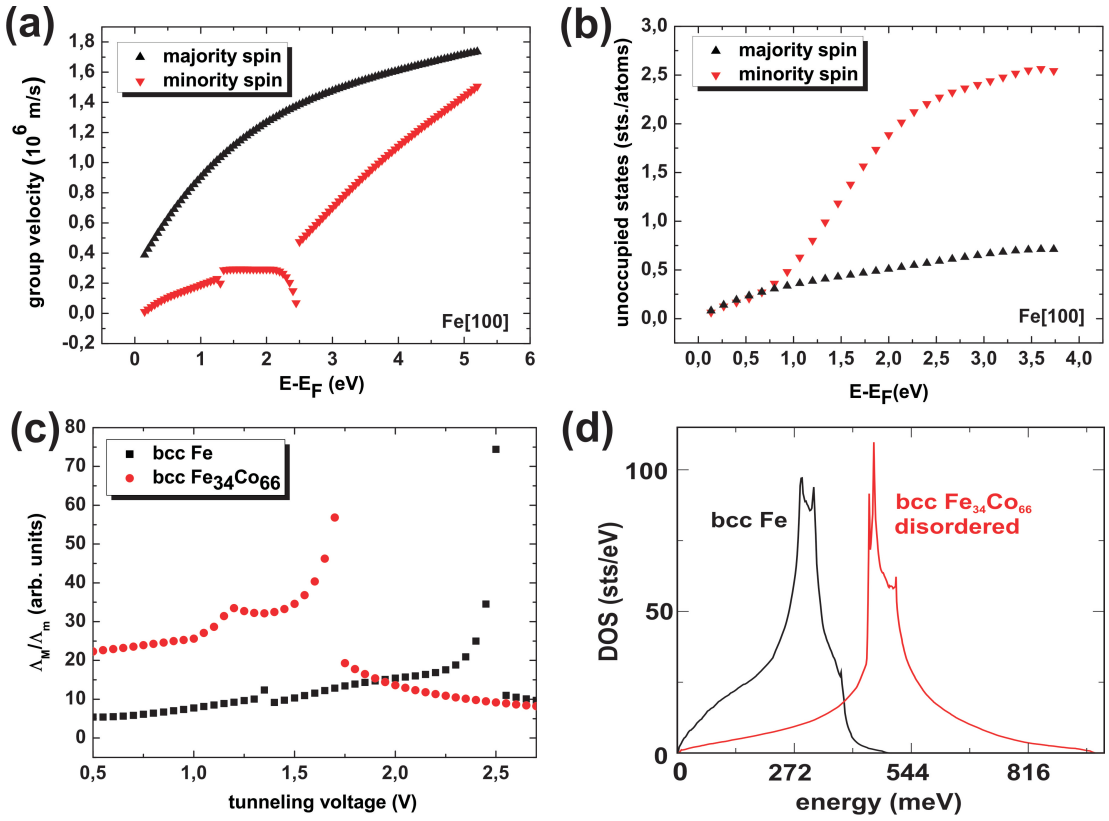

Figure 4.25: Spin resolved k-averaged group velocity along [100](a) and the spin dependent integrated unoccupied density of states of bcc $Fe_{34}Co_{66}$(b) at room temperature (b). Mean free path along [100] as calculated from (a) and (b), see (c), and magnonic density of states for bcc Fe and disordered bcc $Fe_{34}Co_{66}$ [138].

dependence observed in Fig.4.22(a) and (b). Interestingly, with the significant influence of thermally excited magnons on hot electron relaxation we may ascribe the kink-like feature of the $I_C U$-characteristics to magnon mediated sd-scattering. The major part of unoccupied final electronic states is found at electron energies of $E = 1.6$ and $E = 0.3$ eV above E_F for Fe and $Fe_{34}Co_{66}$, respectively, see Fig.4.24 and 4.14. Once the electron energy of the tunnel injected electrons exceeds these values by the thermal energy $k_B T$, magnon mediated absorption(emission) of thermal magnons by majority(minority) spin hot electrons is reduced boosting ballistic electron transport. The threshold energy is too low to be observed for $Fe_{34}Co_{66}$ but detectable for Fe. The fact that the kink structure is found at tunneling voltages of $U_K = -1.8$ V and not at $U = -1.6$ V can be attributed to the broad energy distribution of hot electrons, shifting this feature slightly towards larger voltages U.

In conclusion all observed differences in hot electron transport between bcc Fe and bcc $Fe_{34}Co_{66}$ point to the distinct influence of hot electron interaction with thermally

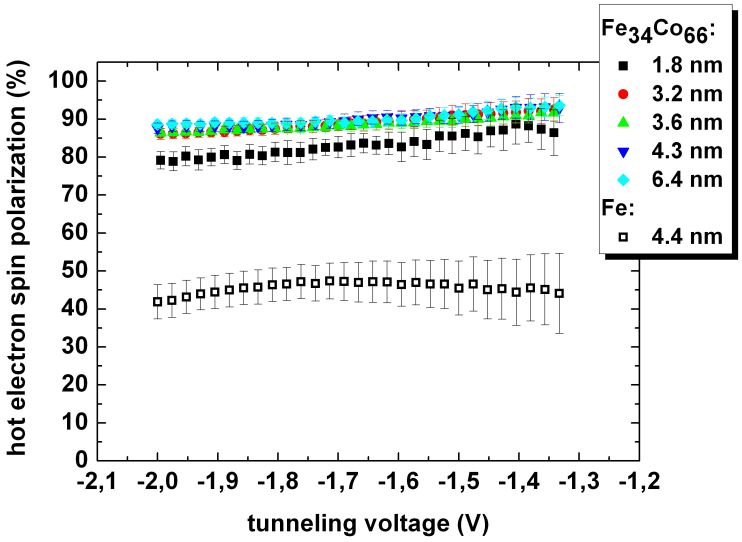

Figure 4.26: Hot electron spin polarization for bcc $Fe_{34}Co_{66}$ and bcc Fe at room temperature for various film thicknesses.

excited spin waves.

Let us conclude, this chapter by evaluating the hot electron spin polarization. For the 9.1 nm thick $Fe_{34}Co_{66}$ film of this spin valve we can readily utilize the spin polarization data of the 6.4 nm thick $Fe_{34}Co_{66}$ film. Differences in spin polarization will be restricted to single percent only, because both thicknesses are already sufficient to filter out almost all minority spin hot electrons, see again Fig.4.10. The low magnetocurrents measured in the last study are reflected in a low hot electron spin polarization for bcc Fe, see Fig.4.26. Hence, one should favor $Fe_{34}Co_{66}$- over Fe-films in spin injection and detection experiments based on hot electron filtering.

5 Conclusion

This chapter provides a short overview of the most important accomplishments:

1. A UHV-STM/BEEM setup has been constructed, built and optimized for the detection of low electrical currents flowing almost ballistically through a hot electron transistor device. Spin contrast in hot electron transport is achieved by introducing a spin valve layer stack into the base and investigated as function of electron energy, sample temperature and layer thicknesses.
2. The tunneling process between emitter and base as well as hot electron transport across the metal/semiconductor interface has been modeled within a free electron approach. The relevant ballistic hot electron paths through the layer stack building up the collector current are found to be very perpendicularly oriented with respect to the film planes.
3. The examination of the Schottky diode (base/collector) characteristics allowed us to extract the sample resistance and to select operational diodes from defective sample pieces.
4. The complete epitaxial lattice structure of the spin valve layer stack has been verified by cross-sectional TEM studies as well as by electron diffraction (RHEED) during layer deposition.
5. The magnetic response of the spin valve structures upon applying an external magnetic field is studied with MOKE on macroscopic and with BEEM on microscopic length scales at various temperatures. In this way also the homogeneity of the magnetization behavior can be studied. When the field is aligned with the [110]-axis of the substrate, overgrown $Fe_{34}Co_{66}$/Au/$Fe_{34}Co_{66}$ spin valves show a magnetization reversal, which is exclusively carried out by domain wall nucleation and motion processes. A Ferromagnetic Resonance study accompanied by hysteresis loop simulations reveals further that ideally the desired parallel and antiparallel magnetization configurations of the spin valve are adjustable, only. This behavior becomes more complex and even inhomogeneous for Fe/Au/$Fe_{34}Co_{66}$ spin valves. Only at room temperature the desired two collinear configurations could be reproducibly achieved.
6. The hot electron attenuation length, an analog quantity to the electron mean free

path, has been determined for bcc $Fe_{34}Co_{66}$ and fcc Au by means of wedge layer studies. Their values reflect bulk properties of hot electron transport along the vicinity of the [100]-axis of the corresponding lattice. It is found that the majority spin attenuation length is more than 6 times larger than the one for minority spin hot electrons for $Fe_{34}Co_{66}$ and that the spin asymmetry in transport is governed by bulk rather than interface properties. Results are discussed with regard to literature data in order to check for an improved hot electron transmission through epitaxially grown base layers. It turned out that there is no significant difference between magnetron-sputtered and MBE-grown FeCo-alloy films on GaAs(100) or related substrates. However, the large attenuation length of 22 nm found for fcc Au-films evidences that bulk scattering at grain boundaries is suppressed due to the single-crystalline structure.

7. The replacement of one of the bcc $Fe_{34}Co_{66}$-films with a bcc Fe-layer accompanied by a temperature dependent study allowed us to distinguish between the various relaxation channels of hot electrons. Additional information could be extracted by means of a golden rule approach for hot electron transport, which is based on the real bandstructure of these materials. The spin asymmetry in hot electron transport through $Fe_{34}Co_{66}$-films could be correlated to the spin dependence of the electronic group velocity as well as of the electron-electron scattering rate, while its temperature dependence stems from the influence of thermal magnons. The decay of magnetocurrent with increasing tunneling voltage is a result of reduced hot electron filter efficiency of the metal/semiconductor interface. In this way, I_C is more built up of secondary- and already scattered primary hot electrons, which significantly enhances the contribution of minority spin hot electrons.

   The reduced spin contrast, enhanced temperature dependence and the appearance of the kink-feature in the characteristics upon introducing the Fe-film can be well explained with an enhanced scattering rate at thermal magnons, only. On the contrary, attempts to correlate these effects to the altered group velocity and to electron-electron relaxation in iron were not successful.

8. Reliable magnetocurrent values up to 1200 % at 293 K and exceeding 3000 % at 85 K have been obtained with epitaxial $Fe_{34}Co_{66}$/Au/$Fe_{34}Co_{66}$ spin valves. The latter value is close to the largest magnetocurrent of 3400 % measured at 77 K, while the former sets a new record value at room temperature.

9. The evaluation of the hot electron spin polarization reveals that ultrathin films of bcc $Fe_{34}Co_{66}$ are already sufficient to create a hot electron spin polarization close to 100 %. On the contrary, bcc Fe-films have to be much thicker in order to achieve the same degree of spin polarization. $Fe_{34}Co_{66}$ should be therefore favored over Fe in hot electron spin filtering experiments.

Bibliography

[1] E. Carpene et al. *Phys.Bev.B* **78**, *174422 (2008).*

[2] M Cinchetti et al. *Phys.Rev.Lett.* **97**, *177201 (2006).*

[3] I. Appelbaum, B. Huang, and D.J. Monsma. *Nature Lett.* **447**, *295 (2007).*

[4] M .Aeschlimann et al. *Phys.Rev.Lett.* **79** *(25), 5158 (1997).*

[5] D.J. Monsma, J.C. Lodder, Th.J.A. Popma, and B. Dieny. *Phys.Rev.Lett.* **74** *(26), (1995).*

[6] D.J. Monsma, R. Vlutters, and J.C. Lodder. *Science* **281**, *407 (1998).*

[7] T. Kinno, K. Tanaka, and K. Mizushima. *Phys.Bev.B* **56** *(8), 56 (1997).*

[8] W.H. Rippard and R.A. Buhrman. *Appl.Phys.Lett.* **75**, *1001 (1999).*

[9] B. Huang and I. Appelbaum. *Appl.Phys.Lett.* **100**, *034501 (2006).*

[10] B. Huang, D.J. Monsma, and I. Appelbaum. *Phys.Rev.Lett.* **99**, *177209 (2007).*

[11] J. Schmalhorst, S. Kämmerer, G.Reiss, and A.Hütten. *Appl.Phys.Lett.* **86**, *052501 (2005).*

[12] M.P. Seah and W.A. Dench. *Surface and Interface Analysis* **1** *(1), (1979).*

[13] T. Balashov, A.F. Takacs, W. Wulfhekel, and J. Kirschner. *Phys.Rev.Lett.* **97**, *187201 (2006).*

[14] C.L. Gao et al. *Phys.Rev.Lett.* **101**, *167201 (2008).*

[15] I. Appelbaum and V. Narayanamurti. *Phys.Rev.B* **71**, *045320 (2005).*

[16] R. Vlutters et al. *Phys.Rev.B* **65**, *024416 (2001).*

[17] J.J. Quinn. *Phys.Rev.* **126** *(4), 1453 (1962).*

[18] J. Hong and D.L. Mills. *Phys.Rev.B* **62** *(9), 5589 (2000).*

[19] F. Simon et al. *Phys.Rev.Lett.* **101**, *177003 (2008).*

[20] E.V. Chulkov et al. *Chem.Rev.* **106**, *4160 (2006).*

[21] V.P. Zhukov, E.V. Chulkov, and P.M. Echenique. *Phys.Rev.B* **73**, *125105 (2006).*

[22] M. Heiblum, D.C. Thomas, C.M. Knoedler, and M.I. Nathan. *Surface Science* **174**, *478 (1986).*

[23] M. Heiblum. *Solid State Electronics* **24**, *343 (1981).*

[24] C.A. Mead. *Proc. IRE* **48**, *359 (1960).*

[25] T. Banerjee, E. Haq, M.H. Siekman, J.C. Lodder, and R. Jansen. *Phys.Rev.Lett.* **94**, *027204 (2005).*

[26] S. van Dijken, X. Jiang, and S.S.P. Parkin. *Appl.Phys.Lett.* **83** *(5), 951 (2003).*

[27] R. Heer, J. Smoliner, J. Bornemeier, and H. Brückl. *Appl.Phys.Lett.* **85** *(19), 4388 (2004).*

[28] M. Kozhevnikov, E.Y. Lee, and V. Narayanamurti. *Phys.Rev.B* **61** *(20), 13914 (2000).*

[29] S. Yuasa, T. Nagahama, and Y. Suzuki. *Science* **297**, *234 (2002).*

[30] B.G. Park, T. Banerjee, J.C. Lodder, and R. Jansen. *Phys.Rev.Lett.* **97**, *137205 (2006).*

[31] S. van Dijken, X. Jiang, and S.S.P. Parkin. *J.Appl.Phys.* **97**, *043712 (2005).*

[32] R. Sato and K. Mizushima. *Appl.Phys.Lett.* **79** *(8), 1157 (2001).*

[33] J.G. Simmons. *J.Appl.Phys.* **34** *(6), 1793 (1963).*

[34] N.E. Christensen. *Phys.Rev.B* **13** *(6), 2698 (1976).*

[35] V. Narayanamurti and M. Kozhevnikov. *Phys.Rep.* **349**, *447 (2001).*

[36] M. Prietsch. *Phys.Rep* **253**, *163 (1995).*

[37] S.H. Liu, C. Hinnen, C. Nguyen van Huong, N.R. de Tacconi, and K.M. Ho. *J.Electroanal.Chem.* **176**, *325 (1984).*

[38] G. Schönhense. *Annalen der Physik* **25**, *465 (1993).*

[39] S. van Dijken, X. Jiang, and S.S.P. Parkin. *Phys.Rev.B.* **66**, *094417 (2002).*

[40] L.D. Bell. *Phys.Rev.Lett.* **77** *(18), 3893 (1996).*

[41] H. Ebert. *Bandstructure calculation using the Bloch spectral function method, Ludwig-Maximilian University of Munich (2008).*

[42] R. Knorren, K.H. Bennemann, R. Burgermeister, and M. Aeschlimann. *Phys.Rev.B* **61** *(14), 9427 (2000).*

[43] L. Bürgi, O. Jeandupeux, H. Brune, and K. Kern. *Phys.Rev.Lett.* **82** *(22), 4516 (1999).*

[44] E. Heindl, J. Vancea, and C.H. Back. *Phys.Rev.B* **75***, 073307 (2007).*

[45] M.K. Weilmeier, W.H. Rippard, and R.A. Buhrman. *Phys.Rev.B* **59** *(4), R2521 (1999).*

[46] E. Haq, T. Banerjee, M.H. Siekman, J.C. Lodder, and R. Jansen. *Appl.Phys.Lett.* **88***, 242501 (2006).*

[47] E. Haq, T. Banerjee, M.H. Siekman, J.C. Lodder, and R. Jansen. *Appl.Phys.Lett.* **86***, 082502 (2005).*

[48] E. Zarate, P. Apell, and P.M. Echenique. *Phys.Rev.B* **60** *(4), 2326 (1999).*

[49] R. Knorren, G. Bouzerar, and K.H. Bennemann. *J.Phys.:Condens.Matter* **14***, R739 (2002).*

[50] R. Keyling, W.D. Schöne, and W. Ekardt. *Phys.Rev.B* **61** *(3), 1670 (2000).*

[51] I. Campillo, A. Rubio, J.M. Pitarke, A. Goldman, and P.M. Echenique. *Phys.Rev.Lett.* **85** *(15), 3241 (2000).*

[52] S.M. Sze, J.L. Moll, and T. Sugano. *Solid State Electronics* **7***, 509 (1964).*

[53] D. Sprinzak, M. Heiblum, Y. Levinson, and H. Shtrikman. *Phys.Rev.B.* **55** *(16), R10185 (1997).*

[54] B.A. McDougall, T. Balasubramanian, and E. Jensen. *Phys.Rev.B.* **51** *(19), 13891 (1995).*

[55] F. Koshiga and T. Sugano. *J.J.Appl.Phys.* **5** *(11), 1036 (1966).*

[56] A. Eiguren et al. *Phys.Rev.Lett.* **88** *(6), 066805 (2002).*

[57] B. Hellsing, A. Eiguren, and E.V. Chulkov. *J.Phys.:Condens. Matter* **14***, 5959 (2002).*

[58] J.E. Gayone, S.V. Hoffmann, Z. Li, and Ph. Hofmann. *Phys.Rev.Lett.* **91** *(12), 127601 (2003).*

[59] S.J. Tang, Ismail, P.T. Sprunger, and E.W. Plummer. *Phys.Rev.B.* **65***, 235428 (2002).*

[60] M. Plihal, D.L. Mills, and J. Kirschner. *Phys.Rev.Lett.* **82** *(12), 2579 (1999).*

[61] R. Vollmer, M. Etzkorn, P.S. Anil Kumar, H. Ibach, and J. Kirschner. *Phys.Rev.Lett.* **91** *(14), 147201 (2003).*

[62] K. Karlsson and F. Aryasetiawan. *Phys.Rev.B.* **62** *(5), 3006 (2000).*

[63] A. Hofmann et al. *Phys.Rev.Lett.* **102***, 187204 (2009).*

[64] J. Schäfer et al. *Phys.Rev.Lett.* **92** *(9), 097205 (2004).*

[65] S.V. Halilov, A.Y. Perlov, P.M. Oppeneer, and H. Eschrig. *Europhys.Lett.* **39** *(1), 91 (1997).*

[66] R. Vlutters, O.M.J. van't Erve, S.D. Kim, R. Jansen, and J.C. Lodder. *Phys.Rev.Lett.* **88** *(2), 027202 (2002).*

[67] R. Jansen et al. *Phys.Rev.Lett.* **85** *(15), 3277 (2000).*

[68] M.P. Gokhale, A. Ormeci, and D.L. Mills. *Phys.Rev.B.* **46***, 8978 (1992).*

[69] R. Berndt and J.K. Gimzewski. *Phys.Rev.B.* **48** *(7), 4746 (1993).*

[70] R. Berndt and J.K. Gimzewski. *Phys.Rev.Lett.* **67** *(27), 3796 (1991).*

[71] P. Johansson, R. Monreal, and P. Appel. *Phys.Rev.B.* **42** *(14), 9210 (1990).*

[72] E.R. Heller and J.P. Pelz. *Appl.Phys.Lett.* **82** *(22), 3919 (2003).*

[73] W. Berthold et al. *Phys.Rev.Lett.* **88** *(5), 056805 (2002).*

[74] F. Reinert, G. Nicolay, S. Schmidt, D. Ehm, and S. Hüfner. *Phys.Rev.B.* **63***, 115415 (2001).*

[75] P. Wahl, M.A. Schneider, L. Diekhöner, R. Vogelgesang, and K. Kern. *Phys.Rev.Lett.* **91** *(10), 106802 (2003).*

[76] L. Limot, T. Maroutian, P. Johansson, and R. Berndt. *Phys.Rev.Lett.* **91** *(19), 106801 (2003).*

[77] H.-G. Boyen. *Phys.Rev.B.* **56** *(11), 6502 (1997).*

[78] V.P. Zhukov, E.V. Chulkov, and P.M. Echenique. *Phys.Stat.Sol.(a)* **205** *(6), 1296 (2008).*

[79] P. Monod and F. Beuneu. *Phys.Rev.B.* **19** *(2), 911 (1979).*

[80] F. Simon et al. *Phys.Rev.Lett.* **101***, 177003 (2008).*

[81] R. Jansen, S.D. Kim, R. Vlutters, O.M.J. van't Erve, and J.C. Lodder. *Phys.Rev.Lett.* **87** *(16), 166601 (2001).*

[82] J. Smoliner, D. Rakoczy, and M. Kast. *Rep.Prog.Phys.* **67***, 1863 (2004).*

[83] W.E. Spicer, I. Lindau, P. Skeath, and C.Y. Su. *J.Vac.Sci.Technol.* **17** *(5), 1019 (1980).*

[84] A. Spitzer, J. Vigroux, J. Moser, and G. Bayreuther. *IEEE Trans. on Magn.* **43** *(6), 2857 (2007).*

[85] C.Y. Chang and S.M. Sze. *Solid State Electronics* **13***, 727 (1970).*

[86] A.B. Chen and A. Sher. *Phys.Rev.B.* **23** *(10), 5360 (1981).*

[87] K. Schwarz and D.R. Salahub. *Phys.Rev.B* **25** *(5), 3427 (1982).*

[88] V.L. Moruzzi. Calculated electronic properties of ordered alloys. *World Scientific (1995).*

[89] D.L. Smith, M. Kozhevnikov, E.Y. Lee, and V. Narayanamurti. *Phys.Rev.B* **61** *(20), 13914 (2000).*

[90] E.H Rhoderick and R.H. Williams. Metal-semiconductor contacts. *Clarendon Press Oxford (1988).*

[91] E.Y. Lee and L.J. Schowalter. *J.Appl.Phys.* **70** *(4), 2156 (1991).*

[92] W.J. Kaiser and L.D. Bell. *Phys.Rev.Lett.* **61** *(20), 2368 (1988).*

[93] G. Klimeck, R.C. Bowen, T.B. Boykin, and T.A. Cwik. Superlattices and microstructures. **27** *(5), 519 (2000).*

[94] R. Ludeke and M. Prietsch. *J.Vac.Sci.Technol.* **A9** *(3), 885 (1990).*

[95] R. Ludeke, M. Prietsch, and A. Samsavar. *J.Vac.Sci.Technol.* **B9** *(4), 2342 (1991).*

[96] M. Prietsch and R. Ludeke. *Phys.Rev.Lett.* **66** *(19), 2511 (1991).*

[97] M.Schmid. *Diploma thesis, University of Regensburg (2010).*

[98] E. Heindl, C. Kefes, M. Soda, J. Vancea, and C.H. Back. *J.Magn.Magn.Mat.* **321***, 3693 (2009).*

[99] R. Jansen, T. Banerjee, B.G. Park, and J.C. Lodder. *Appl.Phys.Lett.* **90**, *192503 (2007).*

[100] Femto Messtechnik Gmbh. *priv. comm.*

[101] R. Heer, C. Eder, J. Smoliner, and E. Gornik. *Rev.Sci.Instrum.* **68** *(12), 4488 (1997).*

[102] L. Libioull, A. Radenovic, E. Bystrenova, and G. Dietler. *Review of Scientific Instruments* **74** *(2), 1016 (2003).*

[103] B. Michel, L. Novotny, and U. Dürig. *Ultramicrsocopy* **42-44**, *1647 (1992).*

[104] *http://www.imagineeringezine.com/e-zine/efield-3.htm.*

[105] H. Birk, M.J.M. de Jong, and C. Schönenberger. *Phys.Rev.Lett.* **75** *(8), 1610 (1995).*

[106] J. Giaime, P. Saha, D. Shoemaker, and L. Sievers. *Review of Scientific Instruments* **67** *(1), 208 (1995).*

[107] Z.J. Radzimski et al. *Appl.Phys.Lett.* **52** *(20), 1692 (1988).*

[108] K. Nakamura, T. Hashimoto, T. Yasui, M. Yoshimoto, and H. Matsunami. *Jpn.J.Appl.Phys.* **40**, *1377 (2001).*

[109] X. Zhang et al. *Jpn.J.Appl.Phys.* **32**, *L755 (1993).*

[110] C.J. Gutierrez et al. *J.Magn.Magn.Mat.* **126**, *232 (1993).*

[111] W.H. Rippard and R.A. Buhrman. *Phys.Rev.Lett.* **84** *(5), 971 (2000).*

[112] B. Heinrich. Ultrathin Magnetic Structures I. *Springer (1994).*

[113] L.C. Chen et al. *J.Vac.Sci.Technol.* **B18** *(4), 2057 (2000).*

[114] G. Bayreuther, M. Dumm, B. Uhl, R. Meier, and W. Kipferl. *J.Appl.Phys.* **93** *(10), 8230 (2003).*

[115] F. Bianco, P. Bouchon, M. Sousa, G. Salis, and S.F. Salvarado. *J.Appl.Phys.* **104**, *083901 (2008).*

[116] T. Leeb, M. Brockmann, F. Bensch, S. Miethaner, and G. Bayreuther. *J.Appl.Phys.* **85**, *4964 (1999).*

[117] B. Heinrich and J.F. Cochran. *Advances in Physics* **42**, *523 (1993).*

[118] FMR data analyzed by G.Woltersdorf.

[119] E. Heindl, G. Woltersdorf, J. Vancea, and C.H. Back. *Phys.Rev.B* **76**, *104435 (2007).*

[120] B.A. Gurney et al. *Phys.Rev.Lett.* **71** *(24), 4023 (1993).*

[121] R. Jansen. *J.Phys.D:Appl.Phys.* **36** *R289, (2003).*

[122] M. Julliere. *Phys.Lett.A* **54**, *225 (1975).*

[123] A.C. Perrella, P.G. Mather, and R.A. Buhrman. *J.Appl.Phys.* **98**, *093713 (2005).*

[124] A. Kaidatzis, S. Rohart, A. Thiaville, and J. Miltat. *Phys.Rev.B* **78**, *174426 (2008).*

[125] W.H. Rippard and R.A. Buhrman. *J.Appl.Phys.* **87** *(9), 6490 (2000).*

[126] E. Haq et al. *J.Appl.Phys.* **95** *(11), 6930, (2004).*

[127] T. Banerjee, J.C. Lodder, and R. Jansen. *Phys.Rev.B* **76**, *140407(R) (2007).*

[128] X. Jiang, S. van Dijken, R. Wang, and S.S.P. Parkin. *Phys.Rev.B* **69**, *014413 (2004).*

[129] M. Pickel et al. *Phys.Rev.Lett* **101**, *066402 (2008).*

[130] W. Zhang et al. *Microelectronic Engineering* **76** *(1-4), 146 (2004).*

[131] C.A.Ventrice Jr., V.P. LaBella, G. Ramaswamy, H.P. Yu, and L.J. Schowalter. *Phys.Rev.B.* **53** *(7), 3952 (1996).*

[132] A.J. Stollenwerk et al. *Phys.Rev.B* **77**, *033416 (2008).*

[133] Shiyang Zhu et al. *Sol.Stat.Electronics* **44**, *2217 (2000).*

[134] P. Schieffer et al. *Appl.Phys.Lett.* **89**, *161923 (2006).*

[135] R. Moosbühler, F. Bensch, M. Dumm, and G. Bayreuther. *J.Appl.Phys.* **91** *(10), 8757 (2002).*

[136] M. Brockmann, M. Zölfl, S. Miethaner, and G. Bayreuther. *J.Magn.Magn.Mat.* **198-199**, *384 (1999).*

[137] M. Dumm et al. *J.Appl.Phys.* **87** *(9), 5457 (2000).*

[138] L.Sandratskii. *Magnon calculation, data supplied by L. Sandratskii, MPI Halle (2010).*

Publications

- E. Heindl, J. Vancea and C.H. Back, *Ballistic electron magnetic microscopy on epitaxial spin valves*, Phys.Rev.B **75**, 073307 (2007)
- E. Heindl, G. Woltersdorf, J. Vancea and C.H. Back, *Hot electron transport and magnetic anisotropy in epitaxial spin valves*, Phys.Rev.B **76**, 104435 (2007)
- E. Heindl, C. Kefes, M. Soda, J. Vancea and C.H. Back, *Hot electron spin attenuation lengths of bcc $Fe_{34}Co_{66}$ - Room temperature Magnetocurrent of 1200 %*, J.Magn.Magn.Mat. **321**, 3693 (2009)
- M. Schmid, E. Heindl, C. Kefes, J. Vancea and C.H. Back, *The influence of the crystalline structure on hot electron transport in thin gold films*, to be published (2010)

Acknowledgements

Working as a PhD-student in Regensburg was a very interesting and challenging experience. During these years many people were instrumental in this work and in my personal growth, as well. Here is a small tribute to all those people.

Foremost, I would like to thank my family and my parents. Their everlasting support and encouragement cannot be expressed with words but have been doubtlessly essential for the prosperity of this work.

I have collaborated with many colleagues, who all deserve my warmest thanks:

- My deep and sincere gratitude is owned by my supervisors Dr. Johann Vancea and Prof. Dr. Christian H. Back. Their understanding, constructive comments and personal guidance have built the basis of this work.
- I am deeply grateful to Christoph Kefes, Florian Freund, Maximilian Schmid, Hasan Orhan and Dr. Johann Vancea for lots of interesting discussions concerning hot electron transport.
- My sincere thanks are due to the personnel of the local electronic and mechanical workshop, who all participated in the implementation of the BEEM-setup. I owe my specific thanks to Dieter Riedl. His kind support and guidance on electronic topics have been of great value.
- My special gratitude is due to Johann Riedl for his encouragement and assistance in the numerical calculation of the tunneling process.
- I am grateful to Marcello Soda and Olga Ganitcheva for the TEM-investigation, to Georg Woltersdorf for the FMR-analysis, to Prof. Dr. H. Ebert and Stephan Lowitzer for the DFT-calculation of the electronic bandstructures and as well as to Leonid Sandratskii for the calculation of the magnonic DOS. Without their contributions the interpretation of the observed characteristics would remain doubtfully and hypothetically.
- The thesis has been proof-read by Thi Thanh Lan Pham, Maximilian Schmid, Dr. Johann Vancea and Prof. Dr. Christian H. Back. Sincere thanks are given to them all.

Last but not least I would like to thank all of my friends for the pleasurable time up to now in Regensburg. I have lived in this beautiful city for more than 9 years, a period with lots of great memories on and off the job, as well.

Declaration

I herewith declare on oath that I autonomously carried out this PhD-thesis without inadmissible means or third party assistance. I undertake that any data, quotation or concept from the published or unpublished work of another person has been duly acknowledged either by reference or literary quotes.